

AFIT/GE/ENG/04-22



ENHANCING THE INSTANTANEOUS DYNAMIC RANGE OF ELECTRONIC
WARFARE RECEIVERS USING STATISTICAL SIGNAL PROCESSING

THESIS
Bryan E. Smith
First Lieutenant, USAF

AFIT/GE/ENG/04-22

DEPARTMENT OF THE AIR FORCE
AIR UNIVERSITY

AIR FORCE INSTITUTE OF TECHNOLOGY

Wright-Patterson Air Force Base, Ohio

APPROVED FOR PUBLIC RELEASE; DISTRIBUTION UNLIMITED.

The views expressed in this thesis are those of the author and do not reflect the official policy or position of the United States Air Force, Department of Defense, or the United States Government.

AFIT/GE/ENG/04-22

ENHANCING THE INSTANTANEOUS DYNAMIC RANGE OF ELECTRONIC
WARFARE RECEIVERS USING STATISTICAL SIGNAL PROCESSING

THESIS

Presented to the Faculty
Department of Electrical and Computer Engineering
Graduate School of Engineering and Management
Air Force Institute of Technology
Air University
Air Education and Training Command
In Partial Fulfillment of the Requirements for the
Degree of Master of Science in Electrical Engineering

Bryan E. Smith, B.S.E.E.
First Lieutenant, USAF

March 2004

APPROVED FOR PUBLIC RELEASE; DISTRIBUTION UNLIMITED.

AFIT/GE/ENG/04-22

ENHANCING THE INSTANTANEOUS DYNAMIC RANGE OF ELECTRONIC
WARFARE RECEIVERS USING STATISTICAL SIGNAL PROCESSING

THESIS

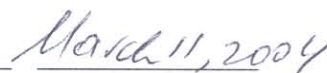
Bryan E. Smith, B.S.E.E.

First Lieutenant, USAF

Approved:



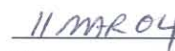
Dr. Meir Pachter
Thesis Advisor



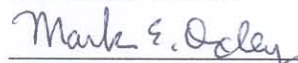
Date



Maj. Matthew E. Goda, PhD.
Committee Member



Date



Dr. Mark E. Oxley
Committee Member



Date

Acknowledgements

The list is large and genuine. First, I would like to thank a great instructor Major Claypoole, who always believed in me. I would like to thank Major Hale, who always pushed me to my limits and beyond, but made me a much better engineer in the process. I learned many of the required research skills for my thesis in Major Hale's and Major Claypoole's classes. I would like to thank Dr. Tsui. It was an honor working with one of the recognized experts in Electronic Warfare. I would also like to thank all of the support staff at AFIT, especially the librarians who helped the Lt with the Tennessee accent find books and Mr. Jim Gray who always seemed to show up and straighten out things in the older Engineering building.

Last but not least, I owe a large debt of gratitude to my thesis advisor, Dr. Pachter, who was a constant source of encouragement during the thesis process. I am a better engineer, professional, and officer through my time spent with Dr. Pachter.

Bryan E. Smith

Table of Contents

	Page
Acknowledgements	iv
List of Figures	vii
List of Tables	ix
List of Symbols	x
List of Abbreviations	xiii
Abstract	xiv
 I. Introduction	 1-1
1.1 EW Receiver	1-1
1.1.1 EW System Operation	1-2
1.1.2 EW Receiver Operation with Time-Coincident Signals	1-5
1.2 IDR Analysis Simplifying Assumptions	1-5
1.3 Problem Statement	1-7
1.4 Scope	1-8
1.5 Methodology	1-9
1.6 Sponsor	1-9
1.7 Summary	1-9
 II. Literature Review	 2-1
2.1 Introduction	2-1
2.2 Instantaneous Dynamic Range Literature Review	2-1
2.3 Cramer-Rao Bound Literature Review	2-1
2.4 Frequency Estimation Literature Review	2-3
2.4.1 Direct ML Estimator for Complex Sinusoids in AWGN	2-4
2.5 Conclusion	2-5
 III. IDR Analysis of a DFT-Based Intercept Receiver	 3-1
3.1 Introduction	3-1
3.2 Deterministic Analysis: The FT of the Sum of Two Sinusoids	3-1
3.2.1 Introduction	3-1
3.2.2 Infinite Data Record	3-2
3.2.3 Finite Data Record	3-2
3.2.4 Sampling	3-5
3.2.5 Discrete Fourier Transform of Two Sinusoids	3-7
3.2.6 Conclusion	3-10
3.3 DFT-Based Intercept Receiver Frequency Detection/Estimation in Noise	3-10

	Page
3.3.1 Frequency Interpolation Methods	3-14
3.4 SLR Method Analysis	3-25
3.4.1 SLR Error Analysis	3-25
3.4.2 SLR Simulation Description	3-26
3.4.3 SLR Simulation Results	3-29
3.4.4 SLR IDR Results	3-32
3.5 Conclusion	3-32
IV. Cramer-Rao Bound for Instantaneous Dynamic Range	4-1
4.1 Introduction	4-1
4.2 Derivation of the CRB for Multiple Sinusoids in AWGN	4-1
4.2.1 Complex Signal CRB	4-1
4.2.2 Real Signal CRB	4-7
4.3 Cramer-Rao Bound for Instantaneous Dynamic Range	4-9
4.4 Conclusion	4-14
V. IGLS Algorithm-Based Parametric Receiver	5-1
5.1 Introduction	5-1
5.2 IGLS Development	5-1
5.2.1 Linear Prediction Theory	5-1
5.2.2 Iterative Generalized Least Squares	5-7
5.2.3 Confidence Intervals for IGLS Estimates	5-9
5.2.4 IGLS Algorithm Simulations	5-12
5.3 IGLS algorithm-based Parametric Receiver compared to the IDR-CRB	5-21
5.3.1 IGLS Algorithm-based Parametric Receiver IDR for Loose Frequency Estimates	5-24
5.4 Conclusion	5-28
VI. Conclusions	6-1
6.1 Introduction	6-1
6.2 Contributions	6-1
6.3 Future Work	6-2
6.4 Summary	6-3
Appendix A. Interference in an EW Receiver	A-1
A.1 Introduction	A-1
A.2 Random Process Theory	A-1
A.3 Thermal Noise	A-2
Appendix B. Power Spectral Density and the Periodogram	B-1
B.1 Introduction	B-1
B.2 Deterministic Power Spectral Density	B-1
B.3 Periodogram	B-4
Bibliography	BIB-1

List of Figures

Figure		Page
1.1.	Parameters measured by an EW receiver	1-2
1.2.	Typical Digital EW System Block Diagram	1-3
1.3.	3-Dimensional Parameter Cube	1-4
1.4.	EW Receiver intercepting Time-Coincident Signals	1-6
2.1.	Direct ML estimator surface plot for two complex sinusoids	2-6
3.1.	Infinite measurement two sinusoid PSD	3-3
3.2.	Two Sinusoids Non-windowed and Windowed FT Magnitude	3-5
3.3.	Two Sinusoids within Fourier Resolution FT Magnitude	3-6
3.4.	Single sinusoid continuous and sampled FT magnitude	3-8
3.5.	Two Sinusoids Zero Padded and Not Zero Padded DFT Magnitude	3-9
3.6.	Orthogonal and Not Orthogonal Sinusoids DFT magnitude	3-10
3.7.	Threshold Demonstration with Noise and Noise+1 Sinusoid	3-12
3.8.	Two Sinusoid + Noise DFT Magnitude	3-13
3.9.	Sinc Lobe Compensation Demonstration.	3-14
3.10.	MPP concept illustration.	3-16
3.11.	Deterministic bias of MPP interpolator for real and complex signals	3-17
3.12.	MPP Interpolator MC MSE versus Δ and SNR	3-18
3.13.	Deterministic bias of PBI interpolator for real and complex signals	3-19
3.14.	PBI Interpolator MC MSE versus Δ and SNR	3-20
3.15.	Deterministic bias of GPBI interpolator for real and complex signals	3-21
3.16.	GPBI Interpolator MC MSE versus Δ and SNR	3-22
3.17.	Interpolator 2 Sin Bias	3-23
3.18.	Interpolator 2 Sin interpolator estimate \hat{f}_1 MSE versus Δ and SNR	3-24
3.19.	Spectral Leakage Estimate Error Statistics vs. Signal 1 SNR and Bins	3-27
3.20.	P_d and P_{fa} results for SLR method.	3-30
3.21.	P_d and P_{fa} results for SLR method.	3-31
3.22.	P_d and P_{fa} results for SLR method.	3-33
3.23.	Histogram of SLR compensated DFT detections	3-34
3.24.	SLR method P_d for low SNR 1.	3-34
4.1.	Equi-amplitude CRB validation	4-8
4.2.	Complex IDR-CRB versus Δf	4-11
4.3.	Real Signal IDR-CRB Algorithm Flowchart	4-12
4.4.	IDR-CRB ($N = 64, 128, 256, 512$) versus Δf	4-13
5.1.	Extended Prony Method Estimation Accuracy	5-14
5.2.	[IGLS Estimation Accuracy (EPM, N=32)	5-15

Figure		Page
5.3.	IGLS Estimation Accuracy (FFT, N=32)	5-17
5.4.	IGLS Estimation Accuracy (FFT, N=128)	5-18
5.5.	IGLS Estimation Accuracy (EPM, M=128)	5-19
5.6.	Figure 5.5(a) zoom analysis	5-20
5.7.	LP Variance Estimate Accuracy	5-21
5.8.	Frequency Estimate Confidence Intervals	5-22
5.9.	IDR-CRB IGLS Performance Analysis Flowchart	5-23
5.10.	IGLS performance for IDR-CRB A_{2b} (EPM)	5-25
5.11.	IGLS performance for IDR-CRB A_{2b} (FFT)	5-26
5.12.	IGLS performance for IDR-CRB A_{2b} (M=128, $f_{acc} = \frac{1}{40N}$)	5-27
5.13.	IDR determination for two sinusoids in white noise.	5-28

List of Tables

Table		Page
1.1.	Example of a typical PDW format	1-3
3.1.	SLR IDR Results (Noise only $P_{fa} = 0.01$)	3-32
5.1.	LP Coefficients to Frequency Relationship	5-4

List of Symbols

Symbol		Page
n	Discrete time	1-7
p	Number of sinusoidal signals	1-7
A_i	ith signal amplitude	1-7
f_i	ith signal RF frequency	1-7
ϕ_i	ith signal phase	1-7
signal 1	Higher amplitude signal	1-7
signal 2	Lower amplitude signal	1-7
\mathbf{x}	EW Receiver Measurement Model	1-7
\mathbf{s}	Signal vector	1-7
\mathbf{w}	AWGN vector	1-7
N	Number of Discrete Time Measurement Samples	1-7
θ	True Parameter Value	2-2
$\hat{\theta}$	Estimated Parameter Value	2-2
$b(\hat{\theta})$	Estimate Bias	2-2
$\text{var}\{\hat{\theta}\}$	Estimate Variance	2-2
\mathbf{x}_c	Complex signal measurement	2-4
$J(\mathbf{f})$	Direct ML objective function	2-5
$x(t)$	Continuous time measurement model	3-2
$X(f)$	FT of continuous time measurement model	3-2
$x_I(t)$	Infinite time measurement model	3-2
τ	Measurement Time	3-3
$\frac{1}{\tau}$	Fourier Resolution	3-4
T	Sampling Period (one)	3-6
f_o	Sampling Frequency	3-6
$x_s(t)$	Sampled measurement signal	3-6
$X(k)$	DFT of $x(n)$	3-8
$X_{SLR}(k)$	SLR method DFS	3-13
$\hat{S}_1(k)$	Estimated DFS of signal 1	3-13
$S_1(k)$	DFS of signal 1	3-13
$W(k)$	Estimated DFS of signal 1	3-13
$S_2(k)$	Estimated DFS of signal 2	3-13
\mathbf{e}_{SLR}	Signal 1 DFS estimate error	3-13
$ X(p) $	Maximum DFS sample point	3-15
α	Variable indicating largest neighbor to $ X(p) $	3-15
$V(\mu)$	Phase Indexed Variable	3-18
γ	Averaged PIV estimate	3-20

Symbol		Page
a	Sinc peak amplitude	3-25
B	Weighted combination for Amplitude Estimate	3-25
P_d	Probability of Detection	3-26
P_{fa}	Probability of False Alarm	3-26
M	Number of Monte Carlo trials	3-28
f_{req}	Required detection frequency accuracy	3-32
\mathbf{s}_c	Complex sinusoidal signal vector	4-1
\mathbf{w}_c	Complex Noise Vector	4-2
$L_\theta(\mathbf{x}_c)$	Log Likelihood Function	4-2
$s(\boldsymbol{\theta}, \mathbf{x}_c)$	Score function	4-3
$\mathbf{J}(\boldsymbol{\theta})$	Fisher Information Matrix of \mathbf{x}_c	4-3
\mathbf{C}	Diagonal amplitude matrix	4-5
\mathbf{M}	J factored frequency and phase dependence	4-5
\mathbf{D}	Upper block of M inverse	4-7
\mathbf{Q}	Real signal J factored frequency and phase dependence	4-9
\mathbf{B}_J	Diagonal Matric to generate Q	4-9
\mathbf{E}	Upper block of Q inverse	4-9
\mathbf{F}	Lower block of Q inverse	4-9
f_{acc}	Desired RMS Frequency Accuracy	4-10
A_{2b}	Lowest Amplitude Possible for Given f_{acc}	4-10
\mathbf{a}	LP coefficient vector	5-2
$\Phi(z)$	Factored LP coefficient polynomial	5-2
\mathbf{X}	Observation matrix	5-5
\mathbf{B}	Constraint matrix	5-6
$\boldsymbol{\alpha}$	Reduced parameter vector	5-6
\mathbf{X}_c	Constrained data matrix	5-6
\mathbf{x}_o	First column of constrained data matrix	5-6
\mathbf{X}_o	Remaining columns of \mathbf{X}_c	5-6
\mathbf{a}_o	Constrained LP coefficient vector	5-6
\mathbf{e}_o	Prediction error vector	5-6
\mathbf{A}^T	M by M - 2p Toeplitz matrix of LP coefficients	5-7
\mathbf{C}_{e_o}	Error vector covariance	5-7
\mathbf{G}	Cholesky decomposition of $\mathbf{C}_{e_o}^{-1}$	5-8
\mathbf{e}_1	Whitened error vector	5-8
\mathbf{A}_k	LP coefficient matrix kth iterate	5-9
$\hat{\mathbf{a}}_o^{(k+1)}$	LP coefficient estimate k+1 iterate	5-9
ρ	Probability error outside confidence interval	5-10
\mathbf{S}_o	Signal component of \mathbf{X}_o	5-10
\mathbf{s}_o	Signal components of \mathbf{x}_o	5-10
\mathbf{q}	$\mathbf{e}_1 - \mathbf{G}\mathbf{s}_o$	5-10

Symbol		Page
$\hat{\mathbf{C}}_{\hat{\mathbf{a}}_o}$	LP coefficient estimation error covariance matrix	5-11
\mathbf{H}	Transformation matrix	5-12
w_p	Unique mapping from LP coefficients to frequency	5-12
$\hat{\mathbf{C}}_{\hat{\mathbf{f}}}$	Frequency estimation error covariance	5-12
$R_{xx}(n, m)$	Autocorrelation value	A-1
$C_{xx}(n, m)$	Autocovariance value	A-2
$S_{WW}(f)$	PSD of White Noise	A-3
σ^2	Noise Variance	A-3
\mathbf{R}	Noise Covariance Matrix	A-3
$S_x(f)$	Power Spectral Density of x	B-2
$R_f(\alpha)$	Autocorrelation of x	B-3
$\hat{S}_{XX}(f)$	Periodogram	B-4

List of Abbreviations

Abbreviation		Page
EW	Electronic Warfare	1-1
AOA	Angle of Arrival	1-1
PA	Pulse Amplitude	1-2
PW	Pulse Width	1-2
TOA	Time of Arrival	1-2
ADC	Analog to Digital Converter	1-2
PDW	Pulse Descriptor Word	1-3
PRF	Pulse Repetition Frequency	1-4
IDR	Instantaneous Dynamic Range	1-5
SNR	Signal-to-Noise Ratio	1-5
AWGN	Additive White Gaussian Noise	1-7
DFT	Discrete Fourier Transform	1-8
IGLS	Iterative Generalized Least Squares	1-8
FT	Fourier Transform	1-9
IGLS	Iterative Generalized Least Squares	1-9
MSE	Mean Square Error	2-1
CRB	Cramer-Rao Bound	2-2
IDR-CRB	Instantaneous Dynamic Range Cramer-Rao Bound	2-2
ML	Maximum Likelihood	2-3
STAP	Space-Time Adaptive Processing	3-4
DFS	Discrete Fourier Spectrum	3-8
FFT	Fast Fourier Transform	3-8
IDFT	Inverse Discrete Fourier Transform	3-8
SLR	Spectral Leakage Reduction	3-12
MPP	Modulus Peak Position	3-14
MC	Monte Carlo	3-16
PBI	Phase Based Interpolator	3-17
PIV	Phase Indexed Variable	3-18
GPBI	Gamma Phase Based Interpolator	3-19
PDF	Probability Density Function	4-2
LP	Linear Prediction	5-1
WSS	Wide Sense Stationary	A-1
PSD	Power Spectral Density	A-1
AWGN	Additive White Gaussian Noise	A-2

Abstract

Accurately processing multiple, time-coincident signals presents a challenge to Electronic Warfare (EW) receivers, especially if the signals are close in frequency and/or mismatched in amplitude. The metric that quantifies an EW receiver's ability to measure time-coincident signals is the Instantaneous Dynamic Range (IDR), defined for a given frequency estimation accuracy, a given frequency separation and a given SNR as the maximum signal amplitude ratio that can be accommodated. Using a two sinusoid time-series model, this thesis analyzes IDR for ideal intercept and parametric digital EW receivers.

In general, the number of signals contained in the EW receiver measurement interval is unknown. Thus, the non-parametric Discrete Fourier Transform (DFT) is employed in an EW intercept receiver with the associated amplitude dependent spectral leakage which limits IDR. A novel method to improve the DFT-based intercept receiver IDR by compensating for the high amplitude signal's spectral leakage using computationally efficient 3 bin interpolation algorithms is proposed and analyzed. For a desired frequency estimation accuracy of 1.5 bins, the method achieves an IDR of 57 dB with little frequency separation dependence when the signals are separated by more than 2 bins with a low amplitude signal SNR of 10 dB.

For situations where the number of signals contained in the measurement interval is known, the IDR of an Iterative Generalized Least Squares (IGLS) algorithm-based parametric receiver is analyzed. A real and complex signal IDR Cramer-Rao Bound (IDR-CRB) is derived for parametric receivers by extending results contained in Rife. For tight frequency estimate requirements (these requirements depend on the number of measurement samples), the IDR-CRB yields achievable bounds. For less stringent frequency estimate requirements, the IDR-CRB is unrealistic due to the noise threshold inherent to frequency estimation. Thus, to achieve good results when less stringent frequency estimates are required, the author defines the IGLS algorithm-based parametric receiver IDR at the amplitude ratio where the frequency estimates first achieve efficiency, i.e., the amplitude ratio where the overmodelling condition first ceases.

ENHANCING THE INSTANTANEOUS DYNAMIC RANGE OF ELECTRONIC WARFARE RECEIVERS USING STATISTICAL SIGNAL PROCESSING

I. Introduction

The ability to identify threat radars is of primary concern to the warfighter. When flying missions, pilots rely on the Electronic Warfare (EW) system to perform this critical task by characterizing the threat radar's signal. If a threat radar is misidentified or worse, undetected, the consequences can be fatal. Of increasing concern to digital EW receiver designers is the growing number of RF transmissions; increasing the probability that the EW receiver intercepts time-coincident signals. Because the time-coincident signals interfere with the receiver's ability to measure both signals correctly, special processing is required which is the focus of this thesis.

1.1 EW Receiver

EW receivers are unique from other receivers operating in the RF region, e.g., radar and communication receivers. The communication and radar receivers know the frequency, types of modulation, and bandwidth of the incoming signal [1]. In an EW receiver, no prior knowledge of the transmission signal is assumed. In addition, in an EW receiver, even the number of intercepted signals is unknown. Thus, EW systems employ wideband radio frequency spectrum and signal analyzers capable of continuous automatic real-time wideband search, detection, and analysis of signals, e.g., the Australian Blue Owl System [2].

An EW receiver measures certain signal parameters during each measurement interval to enable the EW system to identify the signals. Figure 1.1 is an illustration of the parameters, also listed below, that are measured by an EW receiver.

- Frequency
- Angle of Arrival (AOA)

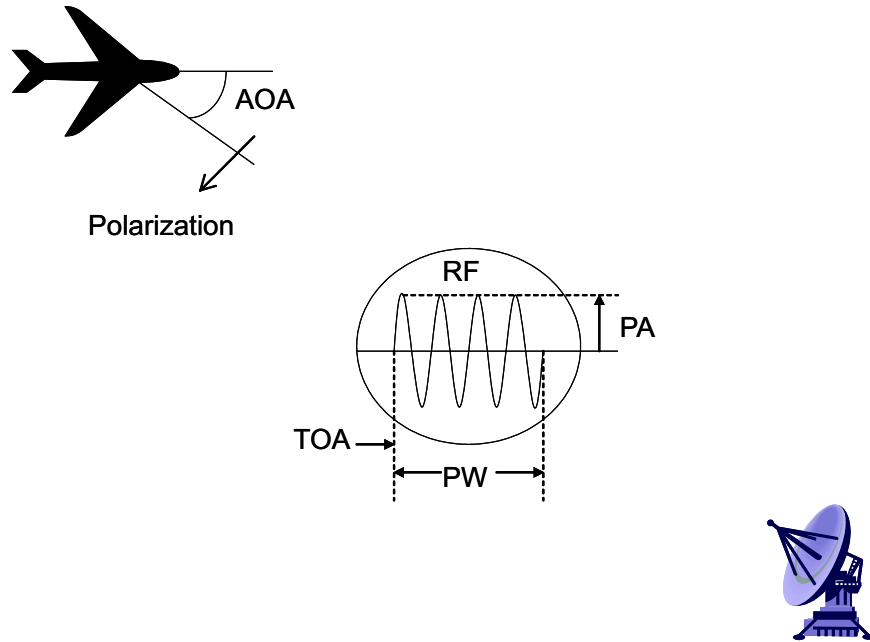


Figure 1.1: Parameters measured by EW receiver [1].

- Pulse Amplitude (PA)
- Pulse Width (PW)
- Time of Arrival (TOA)
- Polarization - EM polarization of pulse i.e. vertical, horizontal, right hand circular, left hand circular.

These parameters are used by the EW system to associate pulses to emitters.

1.1.1 EW System Operation. To understand the purpose and requirements of an EW receiver, it is also helpful to understand the entire system operation. In this section, a walk-through of the operations encountered by a signal in the EW system is discussed. The walk-through follows the block diagram of Figure 1.2 of a typical EW system with digital receiver for radar pulse interception. The EW system is analyzed in three parts: the receiver, the preprocessor, and the post-processor.

Following Fig. 1.2, the antenna intercepts the signal and propagates the signal to the receiver RF amplifier where the information is down converted to an IF frequency. The down converted signals are passed to the Analog-to-Digital Converter (ADC) where

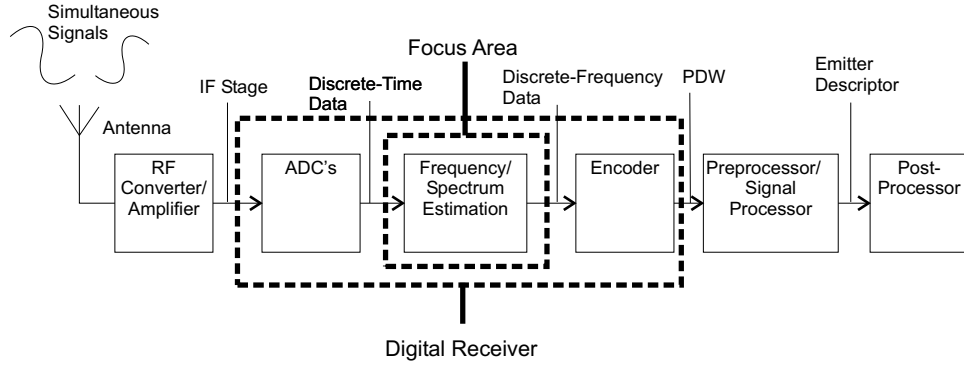


Figure 1.2: Typical Digital EW System Block Diagram [1].

Table 1.1: Example of a typical PDW format [1].

<i>Parameters</i>	<i>Range</i>	<i>No. of Bits</i>
Frequency	Up to 32 GHz	15 (1-MHz resolution)
Pulse Amplitude	Up to 128 dB	7 (1-dB resolution)
Pulse width	Up to 204 μ s	12 (0.05 μ s resolution)
TOA	Up to 50 sec	30 (0.05- μ s resolution)
AOA	360 deg	9 (1-deg resolution)
BPSK signal flag		1
Chirp signal flag		1
Total no. of bits		75

they are time sampled, i.e., a discrete-time representation of the signal. This discrete-time data is passed to the Frequency/Spectrum analysis module in measurement blocks where spectrum/frequency estimation is performed. The frequency/spectrum analysis results are passed to the encoder to form the Pulse Descriptor Word (PDW) containing all of the parameters for any signals contained in the data. An example of a typical PDW is contained in Table 1.1.

The preprocessor processes the stream of PDW's received from the receiver into specific radar pulse trains through a process called de-interleaving. Of the five parameters contained in a PDW, the three parameters used to accomplish de-interleaving are the RF, AOA, and TOA difference between the received pulses [1]. The other two parameters are unsuitable for de-interleaving because PA is dependent on receiving and transmitting antenna position and PW is susceptible to multipath [1]. Differences in AOA is by far the most stable parameter to use for de-interleaving since even aircraft cannot quickly change

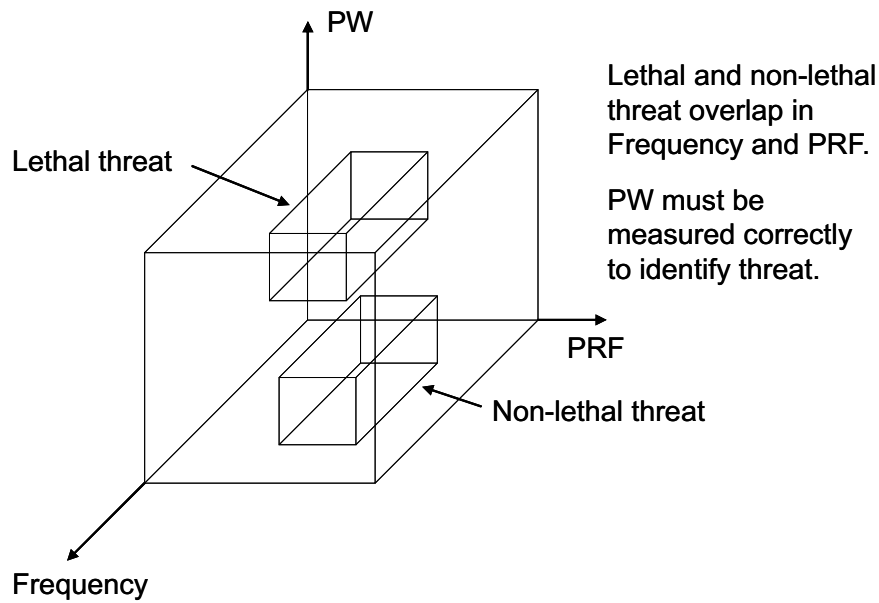


Figure 1.3: 3-Dimensional cube of parameters determining the parameter separating the Lethal threat from the Non-lethal threat [4].

their angular position from pulse to pulse (unfortunately it is also the hardest to measure with any accuracy) [1,3]. Once the pulse trains are de-interleaved into individual radar pulse trains, a number of parameters can be derived from the pulse train such as antenna beamwidth and scan rate from successive amplitude comparisons, mode switching from successive PW's, frequency of emitter pulses from multiple TOA measurements referred to as Pulse Repetition Frequency (PRF), and range from multiple AOA measurements. This information is passed to the post-processor as an emitter report.

The post-processor functions associate the individual emitter reports to specific emitters using parameters contained in the emitter report. This parameter matching is analogous to determining where the emitter report overlaps with target emitters in N-dimensions as in Fig. 1.3 for a 3-dimensional cube. Another way to view this process is querying a database with specific fields and viewing the results. Often, there is overlap and multiple emitters match an emitter report. When this occurs the emitter that is the greatest threat is selected. When an emitter report does not match any entries, then an unknown emitter is sent. Once the emitter is identified, it varies by platform on how the information is utilized.

1.1.2 EW Receiver Operation with Time-Coincident Signals. When time-coincident signals are present in the receiver measurement interval, which is depicted in Fig. 1.4, receiver performance depends on the spectral/frequency estimation function of the receiver. If the time-coincident signals are characterized correctly in the spectral estimation/frequency estimation block of Figure 1.2, all other systems will operate normally. Equi-amplitude signals well separated in frequency do not present much of a problem for the spectral/frequency estimation function. However, signals with large amplitude ratios and/or with close frequencies are difficult for the receiver to measure. The receiver metric that quantifies the ability of an EW receiver to measure time-coincident signals is referred to as the Instantaneous Dynamic Range (IDR) of an EW receiver. The standard IDR definition is

- The standard IDR definition – The IDR is defined in [1] as the power ratio of the maximum and minimum simultaneously received pulses that can be properly encoded by the receiver (and is similarly defined in [4]).

Unfortunately, the standard IDR definition does not reflect the dependence IDR has on signal frequency separation and SNR, which causes confusion when reporting results. Thus, the IDR definition employed in this thesis is

! The thesis IDR definition – IDR is defined as the maximum signal amplitude ratio for a given frequency estimation accuracy, a given frequency separation and a given Signal-to-Noise Ratio (SNR) [5].

1.2 IDR Analysis Simplifying Assumptions

This thesis analyzes IDR for an ideal EW receiver. The following simplifying assumptions are made for the thesis analysis:

- Operation of all devices prior to Spectrum/Frequency Estimation block is assumed nominal to include a perfect ADC, i.e., no quantization error.
- Signals are considered pure sinusoidal tones

$$s(n) = \sum_{i=1}^p A_i \cos(2\pi f_i n + \phi_i), \quad (1.1)$$

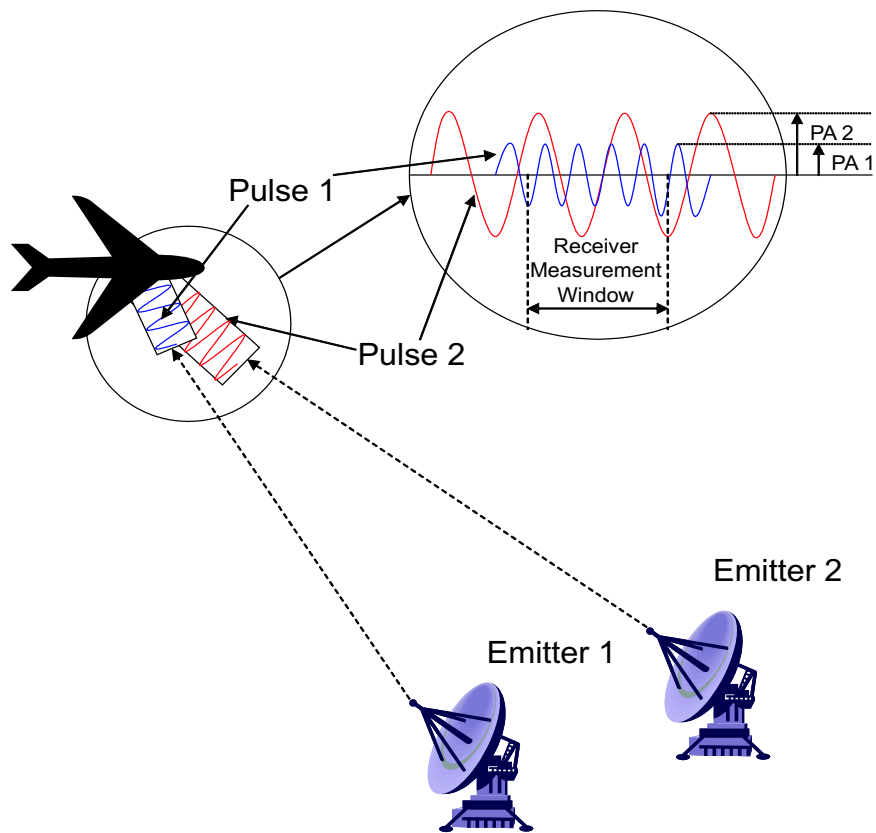


Figure 1.4: EW Receiver intercepting Time-Coincident Signals.

where $s(n)$ is the received signal functional representation at discrete-time n , p is the number of tones, A_i is the i th signal (pulse) amplitude, f_i is the i th signal RF frequency, and ϕ_i is the i th signal phase.

- Signals are assumed to fill the entire measurement period as depicted in Fig. 1.4.
- Thermal noise with the associated Additive White Gaussian Noise (AWGN) model discussed in Appendix A is the only noise considered (no colored noise).

These same simplifying assumptions are made in [1, 5]. **Throughout the thesis, signal 1 is considered the higher amplitude signal, while signal 2 is considered the lower amplitude signal.**

Under the above simplifying assumptions, the mathematical measurement model is

$$x(n) = s(n) + w(n), \quad n = 0, \dots, N - 1 \quad (1.2)$$

where the vector $\mathbf{x} = [x(0), x(1), \dots, x(N - 1)]^T$ is the discrete-time measurement (after the ADC block), \mathbf{s} is the multiple sinusoidal tones defined in (1.1), \mathbf{w} is AWGN, and N is the number of samples. The measurement model of (1.2) is also the standard model used in frequency estimation in statistical signal processing. Thus, there is a vast amount of literature discussing the analysis of (1.2). Chapter II provides a brief review of frequency estimation literature pertinent to the IDR focus.

1.3 Problem Statement

The goal of this research is to investigate the operation of an ideal EW digital receiver when time-coincident signals are present to determine the maximum amplitude ratio of the received signals at which the receiver can still properly measure all of the signals for a given frequency estimation accuracy, a given frequency separation and a given SNR, referred to as the receiver IDR. Because, in the ideal case considered, the measurement model is the same as in frequency estimation; this research applies statistical signal processing techniques. Due to the complexity of analyzing three or more signals, only two time-coincident signals are considered in this research, however, all techniques analyzed (with the exception of the confidence intervals established in Chapter V) can be extended to three or more signals.

EW receivers operate on real signals, thus real signals are considered in the analysis, although complex signals are sometimes employed to simplify examples and mathematical analysis. The IDR definition employed throughout the thesis is defined in Section 1.1.2.

Two types of spectral/frequency estimation blocks are considered. The first type assumes no prior knowledge of the number of signals and employs a non-parametric signal processing technique for spectral/frequency estimation, the Discrete Fourier Transform (DFT). An EW receiver employing a non-parametric spectral/frequency estimation technique is referred to as an *intercept receiver* in this thesis. The second type of spectral/frequency estimation block assumes the number of signals is known and employs a parametric based signal processing technique for frequency estimation, the novel Iterative Generalized Least Squares (IGLS) algorithm. An EW receiver employing a parametric spectral/frequency estimation technique is referred to as a *parametric receiver* in this thesis.

As the number of transmitters in the EW environment explodes, EW receivers effectively processing time-coincident signals is increasing in importance. Understanding the limitations and ways of extending IDR improves EW system operation, directly supporting the war fighter in a critical area. Thus, this thesis has a direct impact on USAF operational systems and results can be applied immediately to digital EW receiver design and software updates.

1.4 Scope

IDR is analyzed for the model of (1.2) using a DFT-based intercept receiver, i.e. a non-parametric frequency estimator, and an IGLS algorithm-based parametric receiver, i.e. a parametric frequency estimator. Other algorithms are outside the scope of this document. The DFT is selected because its universal applicability allows for use of hardware developed for other applications besides EW. The IGLS algorithm is selected because it yields optimal Maximum Likelihood frequency estimates.

1.5 Methodology

The author assumes the reader is familiar with Fourier Transform (FT) theory and statistical signal processing; although Chapter III only requires FT theory and basic knowledge of statistics. The literature review in Chapter II is a brief overview of applicable literature and current IDR research. In lieu of reviewing the required mathematical background for Chapters III, IV, and V in Chapter II, each of the Chapters performs a review of the mathematics involved by (hopefully) finding a common starting point the reader can follow in the development. In Chapter III, deterministic FT theory in the specific IDR context is covered before the theory is extended to analyze the IDR of a novel multiple signal estimation/detection technique. In Chapter IV, the Cramer-Rao bound for multiple equi-amplitude sinusoidal signals originally derived by Rife in [6] is re-derived, and then extended to IDR analysis. In Chapter V, the novel frequency estimation algorithm, Iterative Generalized Least Squares (IGLS), originally developed by Dr. Pachter and researched by Zahirniak in [7] and Ingham in [8], is completely developed beginning with the necessary linear prediction background; concluding with an IGLS comparison to the IDR Cramer-Rao bound in Chapter IV and then a modification to parametric IDR analysis in light of the IDR Cramer-Rao bound comparison results. Thus, original thesis results are located at the end of Chapters III, IV, and V and are summarized in Chapter VI. The author hopes this methodology strikes a delicate balance between inundating the reader with information not pertinent to this research and ensuring the reader can fully understand and interpret the research results. Finally, Matlab[®] is employed where necessary for simulations and analysis.

1.6 Sponsor

This research is funded by the Air Force Research Laboratory Sensors Directorate Radio Frequency Analysis division Parametrics branch (AFRL/SNRP).

1.7 Summary

The research goal is to investigate the performance of an ideal EW digital receiver when time-coincident signals are present in the measurement using the model of (1.2)

to determine the maximum amplitude ratio of the received signals at which the receiver can still properly measure all of the signals for a given frequency estimation accuracy, a given frequency separation, and a given SNR, referred to as the receiver IDR. The IDR is analyzed for a DFT-based intercept receiver and an IGLS algorithm-based parametric receiver. This research is accomplished through the use of statistical signal processing techniques coupled with extensive Matlab[®] simulation and analysis.

II. Literature Review

2.1 Introduction

The literature pertaining to the thesis falls under three veins. Literature concerning IDR, the Cramer-Rao bound, and frequency estimation. Thus, all three of these topics are discussed below. This literature review is intended to provide direction to sources of information to understand the broad context of the research. Mathematical background and literature pertaining directly to the methodology is covered in each of Chapters III, IV, and V.

2.2 Instantaneous Dynamic Range Literature Review

There is little literature analyzing IDR from a statistical signal processing standpoint. Most books mention the issue and provide a definition, but perform little analysis besides mentioning that IDR is frequency dependent [1,3]. Part of the problem is that the standard IDR definition is so broad that many different interpretations can be inferred. Some engineers interpret the ability to measure the signal by using a human to interpret the spectrum. However, the EW system requires numerical frequency estimates for proper signal encoding. **For this thesis, numerical frequency estimates are required** [9]. Most analysis performed on IDR is on a finished receiver with clarification on how IDR is defined for the tests seldom, if ever, provided, i.e., whether the spectrum is interpreted or numerical estimates are obtained, what signal frequency difference is analyzed, etc. [9]. In addition to clarifying IDR for the analysis performed in the thesis, it is hoped that the tests performed in this thesis become a standard for other EW engineers to use when reporting IDR results.

2.3 Cramer-Rao Bound Literature Review

The standard optimality criteria for most estimators is Mean Square Error (MSE) [10], defined as

$$\text{MSE} = \mathcal{E}[(\theta - \hat{\theta})^2], \quad (2.1)$$

where θ is the parameter value to be estimated and $\hat{\theta}$ is the estimated parameter value (Note that RMS error is defined as the square root of mean square error). MSE is used for a variety of reasons: relates to a power statistic, penalizes large errors more than small errors, and is the error variance for unbiased estimators as shown below.

An illuminating estimation result is obtained by multiplying out (2.1) and adding and subtracting $\mathcal{E}\{\hat{\theta}\}^2$

$$\begin{aligned}\text{MSE} &= \mathcal{E}\{\hat{\theta}^2\} - 2\theta\mathcal{E}\{\hat{\theta}\} + \theta^2 + \mathcal{E}\{\hat{\theta}\}^2 - \mathcal{E}\{\hat{\theta}\}^2 \\ &= \text{var}\{\hat{\theta}\} + (\theta - \mathcal{E}\{\hat{\theta}\})^2.\end{aligned}\tag{2.2}$$

Define bias, $b(\hat{\theta})$ as the following

$$b(\hat{\theta}) = \mathcal{E}[(\theta - \hat{\theta})],\tag{2.3}$$

and (2.2) becomes [10]

$$\text{MSE} = \text{var}\{\hat{\theta}\} + b(\hat{\theta})^2.\tag{2.4}$$

Thus, the MSE is composed of the estimate variance, $\text{var}\{\hat{\theta}\}$, along with the squared estimate bias.

Because of the bias term of (2.4), most estimators derived to minimize the MSE directly are unrealizable [10]. However, estimators derived to minimize the estimator variance are *relatively* simple to derive, and if the estimator can be made unbiased, the estimator will minimize the MSE [10]. Limiting the analysis to unbiased estimators also allows comparison to the Cramer-Rao Bound (CRB).

The CRB is a lower bound on the error covariance matrix for any *unbiased* estimator of parameter $\boldsymbol{\theta}$ [11]. The CRB is standard fare in most books on statistical signal processing [10–12]. The CRB for multiple sinusoids in white noise is derived in [6]. In [5], a Cramer-Rao bound is derived for complex signals IDR, when IDR is defined using the thesis definition, and is referred to in the thesis as the complex Instantaneous Dynamic Range Cramer-Rao Bound (IDR-CRB). The algorithm for the complex IDR-CRB is simplified in

Chapter IV and extended to real signals. Note that algorithms that achieve the CRB are referred to as efficient [11].

Unfortunately, comparison to the IDR-CRB is generally not valid for the intercept receiver discussed in Chapter III because the DFT frequency estimates are dominated by frequency quantization and bias when multiple signals are present. Thus, the CRB applies mainly to the parametric receiver of Chapter V, since the estimates provided by the IGLS algorithm are unbiased above threshold (the threshold effect is discussed in Chapter V).

2.4 Frequency Estimation Literature Review

Frequency estimation is a rich and varied subject. Frequency estimators estimate the amplitude, phase and frequency parameters of sinusoidal signals. These parameters are collectively referred to as the parameter vector $\boldsymbol{\theta}$, where $\boldsymbol{\theta} = [A_1 \ f_1 \ \phi_1 \ \dots \ A_p \ f_p \ \phi_p]^T$. Frequency estimators are divided into two types:

- Non-parametric Frequency Estimators: Frequency estimators that do not assume any prior knowledge concerning the data. Thus, non-parametric techniques must also determine the number of signals present in the measurement interval
- Parametric Frequency Estimators: Methods that exploit the data consists of the sum of sinusoids. Number of signals, referred to as model order, is assumed known.

Both types of frequency estimators estimate the amplitude, phase and frequency parameters sinusoidal signals. Because parametric frequency estimators employ knowledge of the signal structure, the estimates provided are much more accurate than the non-parametric frequency estimators. However, if the parametric frequency estimator model order is wrong, results are much worse than non-parametric frequency estimators.

The DFT is the non-parametric frequency estimator employed by the intercept receiver in the thesis (and most digital EW receivers). For a single complex sinusoid in white noise, the zero-padded Periodogram (discussed in Appendix B) peak location is the Maximum Likelihood (ML) estimate [10,11]. For one or more real sinusoids or multiple complex sinusoids, the location of resolvable Periodogram peaks provide biased frequency estimates

as long as the frequencies are separated greater than the Fourier resolution (Fourier resolution is defined in Chapter III).

There are many parametric frequency estimation techniques. To limit the scope of the discussion, only techniques that yield optimal ML frequency estimates are mentioned, since these are the techniques that achieve the IDR-CRB above threshold (the interested reader can refer to [13] for a discussion of many sub-optimal frequency estimation techniques). The four algorithms found in the literature that ML frequency estimates are listed below.

- The direct ML frequency estimator discussed below.
- The IGLS algorithm discussed in Chapter V.
- The IQML algorithm, which is closely related to IGLS, discussed in [14].
- The Mean Likelihood Frequency Estimation algorithm, discussed in [15].

2.4.1 Direct ML Estimator for Complex Sinusoids in AWGN. The direct ML frequency estimate is a complicated function of frequencies with many local minimum. Consider the case of two complex sinusoidal signals in white noise (which is a simpler case than real signals)

$$x_c(n) = A_1 e^{j(2\pi f_1 n + \phi_1)} + A_2 e^{j(2\pi f_2 n + \phi_2)} + w(n), \quad n = 0 \dots N-1 \quad (2.5)$$

where the c subscript on \mathbf{x}_c denotes the complex sinusoids. Form the complex amplitude vector \mathbf{A}_c where $A_c(i) = A_i \exp(j\phi_i)$. Now, let $\mathbf{e}_i = [1, \exp(j2\pi f_i), \dots, \exp(j2\pi f_i(N-1))]^T$ and the $N \times 2$ matrix $\mathbf{E} = [\mathbf{e}_1 \ \mathbf{e}_2]$. The likelihood function of \mathbf{x}_c - referred to as likelihood because \mathbf{x}_c is known and the best estimate of the unknown parameter vector $\boldsymbol{\theta} = [A_1 \ f_1 \ \phi_1 \dots A_p \ f_p \ \phi_p]$ is the $\boldsymbol{\theta}$ that makes \mathbf{x}_c most likely to occur - is [13]

$$f_{\boldsymbol{\theta}}(\mathbf{x}_c) = (\pi\sigma^2)^{-N} \exp \left\{ -\frac{1}{\sigma^2} (\mathbf{x}_c - \mathbf{A}_c \mathbf{E})^H (\mathbf{x}_c - \mathbf{A}_c \mathbf{E}) \right\}. \quad (2.6)$$

If the frequencies are known, the amplitudes and phases ML estimate is a simple least squares estimate [13]

$$\mathbf{A}_c = (\mathbf{E}^H \mathbf{E})^{-1} \mathbf{E}^H \mathbf{x}_c. \quad (2.7)$$

However, if the frequencies are also unknown, maximizing the following objective function is required [13]

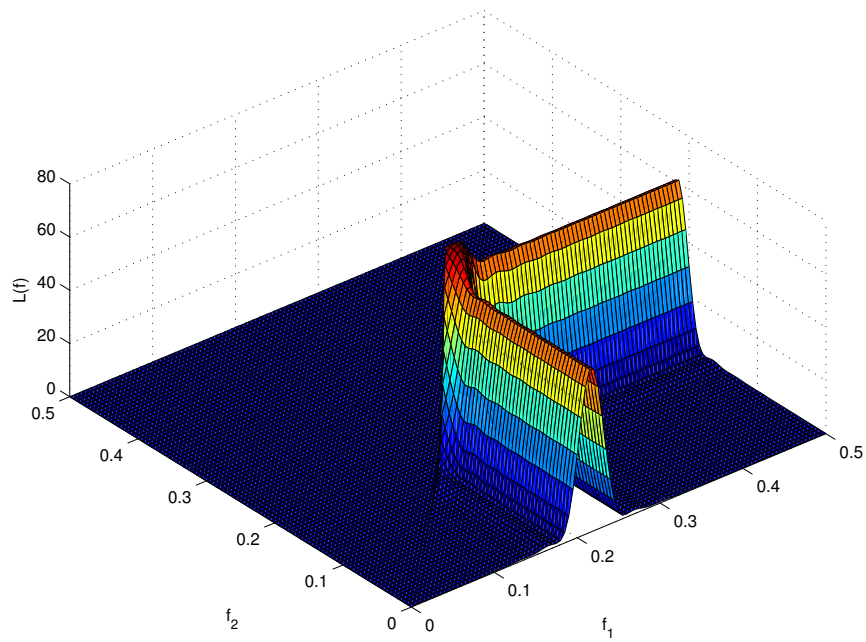
$$J(\mathbf{f}) = \mathbf{x}^H \mathbf{E}(\mathbf{E}^H \mathbf{E})^{-1} \mathbf{E}^H \mathbf{x}. \quad (2.8)$$

$J(\mathbf{f})$ is a highly non-linear function of the unknown frequencies. This non-linear least squares problem is computationally intensive, and, if iterative techniques are employed, there is no guarantee of achieving the global maximum.

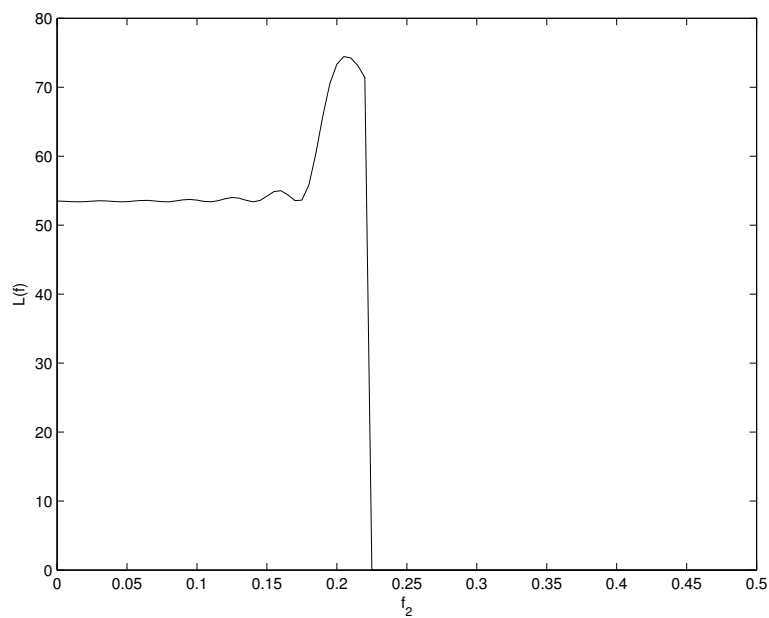
Figure 2.1 is a plot of $J(\mathbf{f})$ with *no noise* and signal parameters: $N=32$ (data record length), $[A_1 = 1, f_1 = 0.227, \phi_1 = \frac{4\pi}{3}]$, $[A_2 = 1, f_2 = 0.207, \phi_2 = \frac{\pi}{3}]$. Note that even without the noise, the function exhibits many local minima and maxima which complicates iterative maximizing techniques - noise increases the estimation difficulty to the point that directly maximizing $J(\mathbf{f})$ is computationally prohibitive for real time applications [13]. Thus, most practical multiple signal frequency estimation algorithms exploit the relationship between the linear prediction coefficients and frequencies, which is the basis of the IGLS frequency estimation algorithm discussed in Chapter V and the IQML frequency estimation algorithm discussed in [14].

2.5 Conclusion

This Literature review is a brief, top-level overview of the issues involved in IDR analysis. IDR, although an important receiver concept, is normally only reported with an associated receiver with no discussion of how the results are obtained. The CRB is normally covered in a typical class on statistical signal processing, with the CRB for multiple sinusoids in AWGN derived by Rife in [6]. Frequency estimation, a large and heavily researched area, is discussed with emphasis on multiple frequency estimation algorithms that achieve ML results. Finally, in Chapters III, IV, V, the necessary mathematical background, assuming the reader is familiar with statistical signal processing concepts and Fourier math, is discussed in order to interpret the results at the end of the chapter.



(a) $J(\mathbf{f})$



(b) $J(\mathbf{f})$ cross-section at $f_1 = 0.227$

Figure 2.1: Direct ML estimator surface plot for two complex sinusoids.

III. IDR Analysis of a DFT-Based Intercept Receiver

3.1 Introduction

In EW intercept receivers, the number of received signals and the signals' carrier frequencies are assumed unknown. Thus, the intercept receiver must also detect the number of signals present in the measurement interval in addition to measuring the signals frequencies. Most new digital EW receivers employ the DFT for multiple signal detection/estimation. If the signals are detected, the frequencies are estimated from the location of the DFT peaks. Thus, in this chapter, the DFT-Based intercept receiver IDR is analyzed. In Section 3.2, a *no noise* deterministic FT signal analysis is performed in the context of IDR. Then, in Section 3.3 a DFT multiple frequency detection/estimation technique for the DFT-based intercept receiver is proposed and IDR evaluated.

3.2 Deterministic Analysis: The FT of the Sum of Two Sinusoids

3.2.1 Introduction. In deterministic FT analysis, spectral leakage limits IDR. Thus, the FT for the sum of two sinusoids is analyzed in this section to fully understand spectral leakage. This section is organized as follows. In Section 3.2.2, an infinite data record is considered, which is the easiest from an analysis standpoint. Then, Section 3.2.3 evaluates the impact of finite records on the FT and discusses spectral leakage. Data record digitization is considered next in Sections 3.2.5 and 3.2.4 including the DFT and IDFT; the DFT's orthogonality principle is also considered. While deterministic Fourier analysis is studied extensively in the literature, the subject matter covered in this section in the specific IDR context yields important insights into the analysis of the DFT-based intercept receiver's IDR. During this sections analysis, a special type of IDR is considered, called *no noise* IDR, which is defined as

! no noise IDR - Maximum amplitude ratio where the no noise FT technique considered, i.e., FT or DFT, still exhibits resolvable peaks for multiple frequency estimates. This is an analysis tool employed to aid the discussion on spectral leakage.

3.2.2 Infinite Data Record. General Fourier theory is developed here to motivate the infinite time FT of two sinusoids. If the measurement interval of a signal, i.e., the data record, approaches infinity, the signal can be represented using the FT as [16]

$$x(t) = \int_{-\infty}^{\infty} X(f)e^{j2\pi ft}df \quad (3.1)$$

referred to as the Inverse Fourier Transform (IFT) of $X(f)$. The FT, $X(f)$, represents the frequency content of $x(t)$ [16]

$$X(f) = \int_{-\infty}^{\infty} x(t)e^{-j2\pi ft}dt. \quad (3.2)$$

Thus, $x(t)$ and $X(f)$ are both continuous-time and continuous-frequency representations of the signal in the respective time and frequency domains.

The infinite FT of the sum of two sinusoids is the simplest to analyze from an IDR standpoint. Let the infinite signal, $x_I(t)$, of interest consist of the sum of two carriers,

$$x_I(t) = A_1\cos(2\pi f_1t + \phi_1) + A_2\cos(2\pi f_2t + \phi_2). \quad (3.3)$$

The FT of $x_I(t)$ is

$$X_I(f) = \frac{A_1e^{j\phi_1}}{j2}\delta(f - f_1) - \frac{A_1e^{-j\phi_1}}{j2}\delta(f + f_1) + \frac{A_2e^{j\phi_2}}{j2}\delta(f - f_2) - \frac{A_2e^{-j\phi_2}}{j2}\delta(f + f_2). \quad (3.4)$$

Equation (3.4) is the infinite time (ideal) FT of the sum of two sinusoids without noise. Note that in the noiseless, infinite time frequency representation of two sinusoids, the frequency resolution is theoretically infinite. As far as IDR performance is concerned, the frequencies can be detected/estimated perfectly regardless of frequency spacing. Figure 3.1 illustrates the infinite resolution for frequency detection/estimation using the magnitude of the FT. Real world finite signal records do not yield infinite resolution.

3.2.3 Finite Data Record. For finite data record analysis, some background tools must be developed. To analyze the finite data records, the rectangular window is

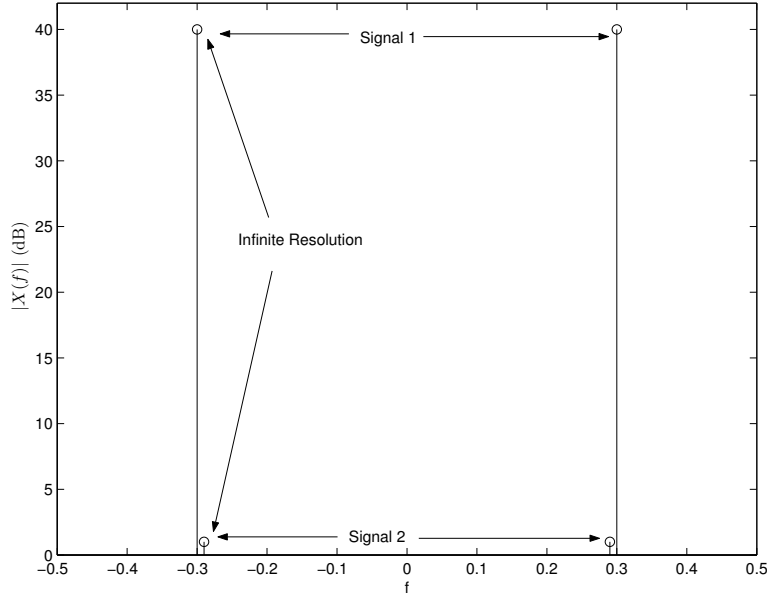


Figure 3.1: Infinite measurement two sinusoid PSD.

introduced

$$\text{rect}\left(\frac{t}{\tau}\right) = \begin{cases} 1, & \text{if } -\frac{\tau}{2} \leq t \leq \frac{\tau}{2} \\ 0, & \text{else} \end{cases} \quad (3.5)$$

where τ is the measurement time/period¹. The FT of $\text{rect}(\frac{t}{\tau})$ is

$$F\left\{\text{rect}\left(\frac{t}{\tau}\right)\right\} = \frac{\cos(\pi f \tau)}{\pi f} = \tau \text{sinc}(f \tau). \quad (3.6)$$

Since the signals of interest are always causal, the rectangular window is shifted in the time domain introducing a phase shift term in the FT of the rectangle window

$$F\left\{\text{rect}\left(\frac{t - \tau/2}{\tau}\right)\right\} = e^{-j\pi f \tau} \tau \text{sinc}(f \tau). \quad (3.7)$$

The following general convolution property of FT's also aids the mathematical analysis of the time-limited signal [16]

$$F\{v(t)z(t)\} = V(f) * Z(f). \quad (3.8)$$

¹A typical measurement time for a digital EW receiver is 100 nanoseconds [1].

The above FT tools are applied to the Fourier analysis of a signal consisting of the sum of two sinusoids.

The signal of (3.3) is multiplied by the time-shifted rectangular time window to model a finite data record. The Fourier Transform of the finite data record is

$$F\{x(t)\} = F\left\{x_I(t)\text{rect}\left(\frac{t - \tau/2}{\tau}\right)\right\} = X_I(f) * e^{-j\pi f\tau}\tau\text{sinc}(f\tau), \quad (3.9)$$

using the convolution property of (3.8). Using the integral sifting property of the δ function and linearity, the FT of two finite-time sinusoids is

$$\begin{aligned} X(f) &= X_I(f) * e^{-j\pi f\tau}\tau\text{sinc}(f\tau) \\ &= \frac{\tau A_1}{2} e^{-j(\phi_1 + \frac{\pi}{2} + \pi(f+f_1)\tau)}\text{sinc}(\tau(f+f_1)) - \frac{\tau A_1}{2} e^{-j(-\phi_1 + \frac{\pi}{2} + \pi(f-f_1)\tau)}\text{sinc}(\tau(f-f_1)) \\ &\quad + \frac{\tau A_2}{2} e^{-j(\phi_2 + \frac{\pi}{2} + \pi(f+f_2)\tau)}\text{sinc}(\tau(f+f_2)) - \frac{\tau A_2}{2} e^{-j(-\phi_2 + \frac{\pi}{2} + \pi(f-f_2)\tau)}\text{sinc}(\tau(f-f_2)) \end{aligned} \quad (3.10)$$

The sinc function side-lobe structure (called spectral leakage in academia or the splatter effect by analog microwave receiver designers) is exclusively a result of the finite data record and limits the detection/estimation of a small amplitude sinusoid in the presence of a high amplitude sinusoid; even in the absence of measurement noise. Side-lobes can be reduced using a technique called windowing. Windows are applied in the same manner as the rectangular function, and gradually reduce the transition of the signal value to zero; decreasing the side-lobe magnitude while increasing the main beam size - Reference [17] is an excellent resource for windowing². Another important limitation of the sinc structure besides sidelobes: The signals cannot be detected/resolved (only one peak will occur) if the sinusoids are closer in frequency than $\frac{1}{\tau}$, referred to as the Fourier resolution.

Figure 3.2 contains a plot³ of the sum of two sinusoids FT with the following parameters: $[A_1 = 1, f_1 = 0.32815, \phi_1 = \frac{\pi}{3}]$, $[A_2 = 0.01, f_2 = 0.1875, \phi_2 = \frac{3\pi}{4}]$, $\tau = 32s$. The amplitude ratio between the two signals is 40 dB. In Fig. 3.2(a), the side-lobes from the higher magnitude sinusoid masks the presence of the lower amplitude sinusoid. Thus, the

²Note the author has successfully applied windowing techniques to Space-Time Adaptive Processing (STAP) for radar [18].

³This plot was generated using Matlab's DFT function and zero padding to approximate a continuous FT, thus some minor aliasing occurs. However, the general shape of the continuous FT is the same.

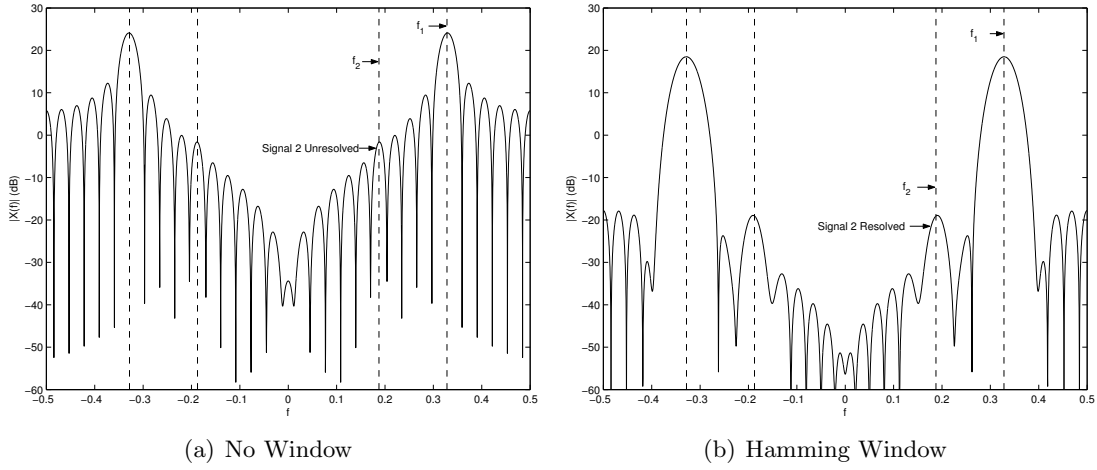


Figure 3.2: Two Sinusoids Non-windowed and Windowed FT Magnitude.

no noise non-windowed FT IDR for this particular frequency difference is less than 40 dB. In Figure 3.2(b), the side-lobes are reduced by windowing, and the presence of the lower amplitude sinusoid is easily discerned. The *no noise* Hamming windowed FT IDR at this particular frequency difference is greater than 40 dB.

Figure 3.3 contains a plot of the sum of two sinusoids FT with the following parameters: $[A_1 = 1, f_1 = 0.32815, \phi_1 = \frac{\pi}{3}]$, $[A_2 = 1, f_2 = 0.1875, \phi_2 = \frac{3\pi}{4}]$, $\tau = 32s$. These frequencies are within the Fourier resolution, $\frac{1}{\tau}$, thus the two frequencies cannot be resolved using conventional FT methods (windowing exacerbates the situation because of the widening of the main beam). The *no noise* FT IDR for these two signals is zero; they are not resolved.

3.2.4 Sampling. Since the EW receiver samples the signal, the sampling effects on the above developments are now analyzed; however, quantization effects are ignored. Assuming the signal is sampled uniformly, the following sampling function is introduced to model the sampling [19]

$$g(t) = \sum_{n=-\infty}^{\infty} \delta(t - nT), \quad (3.11)$$

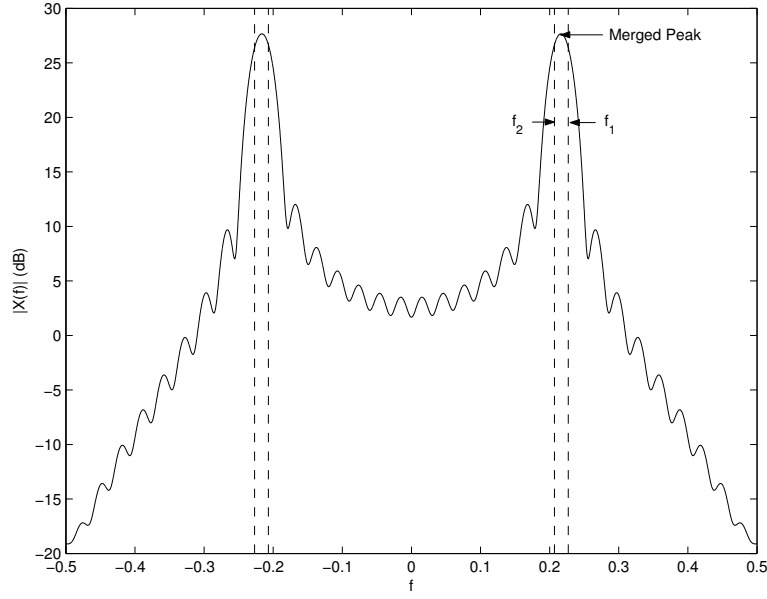


Figure 3.3: Two Sinusoids within Fourier Resolution FT Magnitude.

where T is the sampling period. Equation (3.11) is periodic and can be represented in terms of a Fourier Series [19],

$$g(t) = \sum_{n=-\infty}^{\infty} C_n e^{jn2\pi f_o t}, \quad (3.12)$$

where f_o is the sampling frequency, $f_o = \frac{1}{T}$, and C_n is defined as

$$\begin{aligned} C_n &= \frac{1}{T} \int_0^T \delta(t) e^{-jn2\pi f_o t} dt \\ &= \frac{1}{T}. \end{aligned} \quad (3.13)$$

Recall that $x(t)$ is the signal of interest and let $x_s(t)$ represent the sampled version of the signal,

$$\begin{aligned} x_s(t) &= g(t)x(t) \\ &= \sum_{n=-\infty}^{\infty} \frac{1}{T} e^{jn2\pi f_o t} x(t) \end{aligned} \quad (3.14)$$

Taking the FT of (3.14) and reversing the order of integration and summation yields the following expression

$$\begin{aligned}
F\{x_s(t)\} &= \int_{-\infty}^{\infty} \sum_{n=-\infty}^{\infty} \frac{1}{T} e^{jn2\pi f_o t} x(t) e^{-j2\pi f t} dt \\
&= \frac{1}{T} \sum_{n=-\infty}^{\infty} \int_{-\infty}^{\infty} x(t) e^{-j2\pi(f-nf_o)t} dt \\
&= \frac{1}{T} \sum_{n=-\infty}^{\infty} X(f - nf_o).
\end{aligned} \tag{3.15}$$

Thus, as (3.15) illustrates, the sampled signal's FT is a periodic version of the continuous signal FT about the sampling frequency. The major developments for the continuous two sinusoid signal will hold for the sampled sinusoid signal as long as the sampling rate is at least twice the highest frequency in the signal, to prevent aliasing. However, since finite signals have infinite frequency content, the infinite side-lobes of the sinc function will cause some distortion effects from aliasing in (3.10).

Figure 3.4 contains a plot of a sampled signal FT and a continuous FT for a single sinusoid with the following simulation parameters: $[A_1 = 1, f_1 = 0.32815, \phi_1 = \frac{\pi}{3}]$, $N = 32$. The effects of aliasing are noticeable on side-lobes near $f = 0.5$ and $f = -0.5$. The aliasing causes the side-lobes of the sampled signal FT to be higher than the continuous FT, while effects near the main lobe are negligible.

3.2.5 Discrete Fourier Transform of Two Sinusoids. Since the intercept receiver is a digital receiver, the frequency domain is also digital. The FT of a finite, uniformly sampled signal is

$$X(f) = \sum_{n=0}^{N-1} x(nT) e^{-j2\pi f nT}. \tag{3.16}$$

The signal is uniformly sampled in the frequency domain by letting $f = \frac{k}{NT}$ $k = 0, \dots, N-1$ [19]. Equation (3.16) then becomes

$$X(k) = \sum_{n=0}^{N-1} x(nT) e^{-j2\pi \frac{kn}{N}}, \tag{3.17}$$

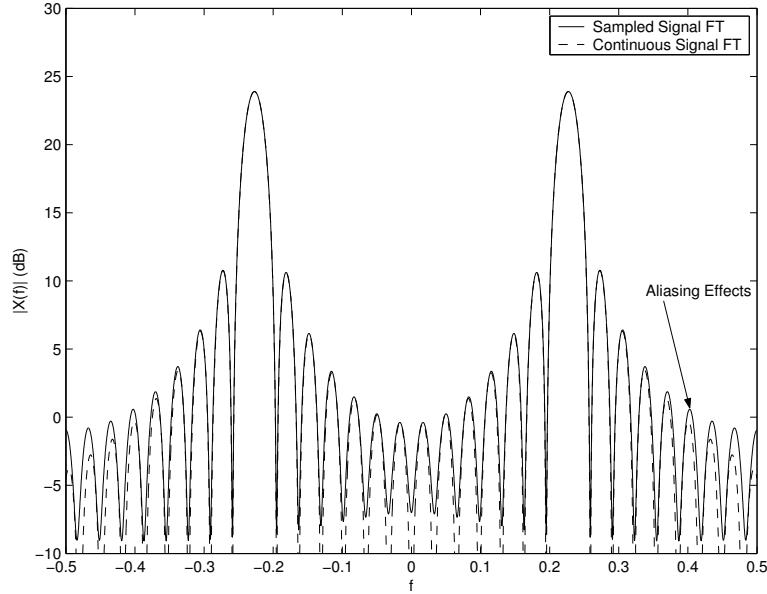


Figure 3.4: Single sinusoid continuous and sampled FT magnitude.

where $X(k)$ is the DFT of $x(nT)$ ⁴. $X(k)$ is referred to as the Discrete Fourier Spectrum (DFS). Note that if the number of frequency samples is a power of two (the number of frequency samples can be more than the number of time samples if the signal is zero padded), the number of arithmetic operations required to perform the DFT is reduced dramatically using the Fast Fourier Transform (FFT) algorithm. The inverse of the DFT, the Inverse Discrete Fourier Transform (IDFT), is

$$F^{-1}\{X(k)\} = x(n) = \frac{1}{N} \sum_{k=0}^{N-1} X(k) e^{j2\pi \frac{kn}{N}}. \quad (3.18)$$

Through use of the IDFT and DFT, a discrete-time signal can be digitally represented in the time or frequency domain. The resolution in frequency when the DFT is used is delimited by the number of frequency sample points, i.e. frequency quantization [15]. Increasing the frequency sampling by zero padding the time sequence increases the frequency resolution, but at a cost of increased computational complexity. When the sinusoids are orthogonal,

⁴Further developments will assume that the sampling rate, T , is equal to one unless stated otherwise since all results can be scaled for the appropriate sampling rate (This is a standard practice in most of the literature on Signal Processing).

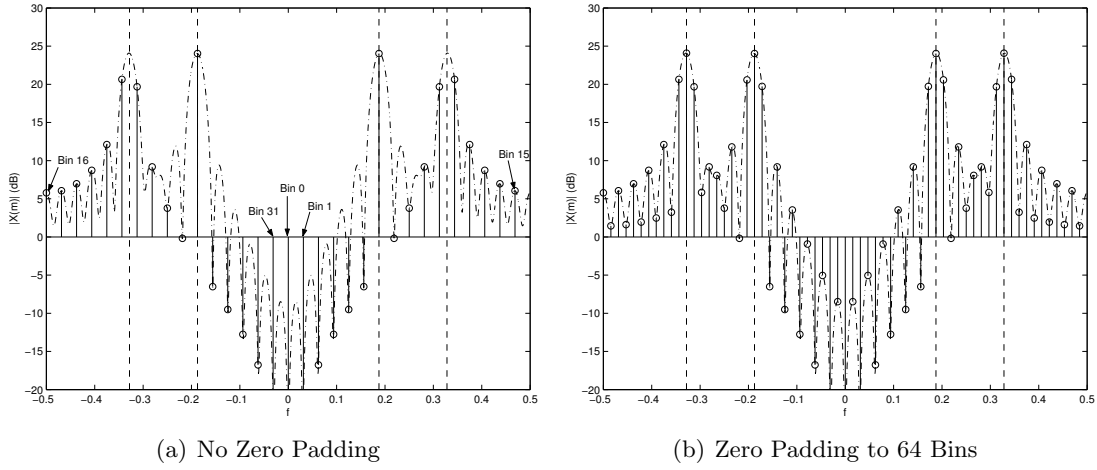


Figure 3.5: Two Sinusoids Zero Padded and Not Zero Padded DFT Magnitude.

i.e. their frequencies are exactly sample points of the DFT, the side-lobes do not mask the signals, and the *no noise* DFT IDR is infinite.

Figure 3.5 contains a plot of the sum of two sinusoids zero padded and non-zero padded DFT with the following parameters: $[A_1 = 1, f_1 = 0.32815, \phi_1 = \frac{\pi}{3}]$, $[A_2 = 1, f_2 = 0.1875, \phi_2 = \frac{3\pi}{4}]$, $N = 32$. The outline of the continuous FT (generated using a 4096-point zero-padded DFT) is also plotted to illustrate where the samples are located. Fig. 3.5(a) shows the frequency sample points are referred to as bins, numbered 0 to 31 starting with the positive frequencies. A common way to refer to frequency in the DFT is the bin position. Thus, $f_1 = 0.32815$ is bin position 10.5, $f_1 = 10.5/M$. The plot in Fig. 3.5(b) illustrates the point that zero padding increases the number of frequency samples.

Figure 3.6 contains of plot of the sum of two sinusoids for orthogonal and non-orthogonal sinusoids over the observation interval for the simulation parameters: $[A_1 = 200, f_1 = \text{Bin } 10, \phi_1 = \frac{\pi}{3}]$, $[A_2 = 2, f_2 = \text{Bin } 6, \phi_2 = \frac{3\pi}{4}]$, $M = 32$. For the orthogonal sinusoids plotted in Fig. 3.6(a), the *no noise* DFT IDR is infinite in because the frequency samples lie along the zeroes of the other signals sinc functions. For Fig. 3.6(b), the frequency of f_1 is changed to Bin 10.5. The spectral leakage of signal 1 is maximum in this case, and signal 2 cannot be resolved. Thus in this situation, the *no noise* DFT IDR is less than 40 dB.

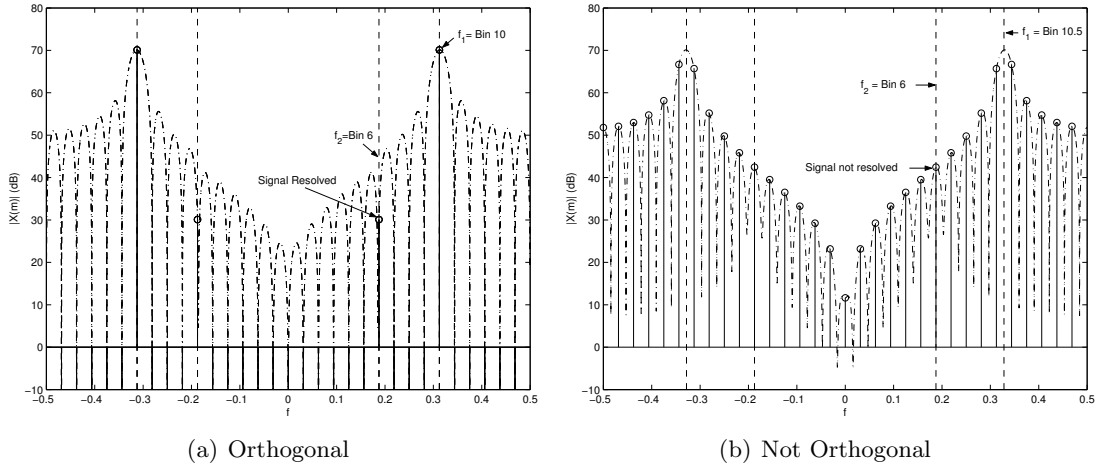


Figure 3.6: Orthogonal and Not Orthogonal Sinusoids DFT magnitude.

3.2.6 Conclusion. The above discussion shows that Fourier techniques are quite robust for the detection and estimation sinusoids *at least, so far, in the absence of noise*. The two areas where the *no noise* FT needs compensation to increase *no noise* IDR are

1. **Sinusoids within the Fourier Resolution Limit.** Other frequency estimation and detection methods must be employed when within the Fourier resolution, regardless of amplitude.
2. **Detection interference from the side lobes of a stronger signal.** Windowing is one popular method to increase no noise IDR.

The next section analyzes a DFT-based EW intercept receiver for its IDR in the presence of sidelobes *and noise*.

3.3 DFT-Based Intercept Receiver Frequency Detection/Estimation in Noise

Now, return to the measurement model of (1.2)

$$x(t) = A_1 \cos(2\pi f_1 + \phi_1) + A_2 \cos(2\pi f_2 n + \phi_2) + w(n). \quad (3.19)$$

In the following analysis, signal 1 is considered the higher amplitude signal, while signal 2 is considered the lower amplitude signal. Determining the number of sinusoids present for signals buried in white noise is a difficult problem, especially for high amplitude ratio

signals. The most accurate methods employ statistical tests that attempt to find the hypothesis with the least error energy, such as information theoretic criteria approaches [13]. Such methods are preferred because they avoid the use of thresholds and have higher resolution than the Fourier resolution. However, the methods are computationally intensive and not practical for Electronic Warfare applications.

The most robust method for an EW intercept receiver is to use either the DFS or Periodogram - described in Appendix B. Assuming the noise variance is known, a noise threshold can be set for detection by determining an acceptable probability of false alarm P_{fa} , i.e. probability that the noise will exceed the threshold at any frequency bin for a single measurement interval, and setting the threshold accordingly⁵. If any bin exceeds the threshold, a detection is declared, and the maximum bin of the measurement is a coarse (quantized) frequency estimate (if noise exceeds the threshold, it is a false alarm).

Figure 3.7 contains a demonstration of the above concepts. The noise alone exceeds the bin threshold for Fig. 3.7(a), thus a false alarm would be declared for this measurement interval. If multiple bins exceed the threshold for a given measurement, only one false alarm is declared. In Figure 3.7(b), a single sinusoid has exceeded the threshold and a detection is declared with simulation parameters⁶: $[A_1 = 1, f_1 = 10.5 \text{ bins}, \phi_1 = \frac{4\pi}{3}]$, $SNR = 20$ (dB), $N = 32$. A coarse frequency estimate for the sinusoid is the bin location of the maximum peak, as shown in the figure. Note that for the assumed single sinusoid case, the side-lobes exceeding the threshold are ignored.

If more than one signal could be in the measurement record, as is the case in EW, the detection problem becomes more complex because of the spectral leakage. Fig. 3.8 contains a plot of the DFT with simulation parameters: $[A_1 = 1, f_1 = 10.5 \text{ bins}, \phi_1 = \frac{\pi}{3}]$, $[A_2 = 0.2, f_2 = 14.2 \text{ bins}, \phi_2 = \frac{3\pi}{4}]$, $SNR = 20$ (dB) referenced to signal 1, $N = 32$. Note that the side-lobe bin magnitude pointed to in the figure is above the signal 2 bin magnitude. EW receivers require that the presence of the weaker signal must be recognized by automation; the spectral leakage exceeding the threshold near the main lobe must be

⁵Typical P_{fa} for an EW receiver is 10^{-11} .

⁶Since real signals are considered, from here on out in this development only bins 1 through $\frac{M}{2}$ (sample number is assumed even) will be considered; the negative frequency images will be ignored unless stated otherwise.

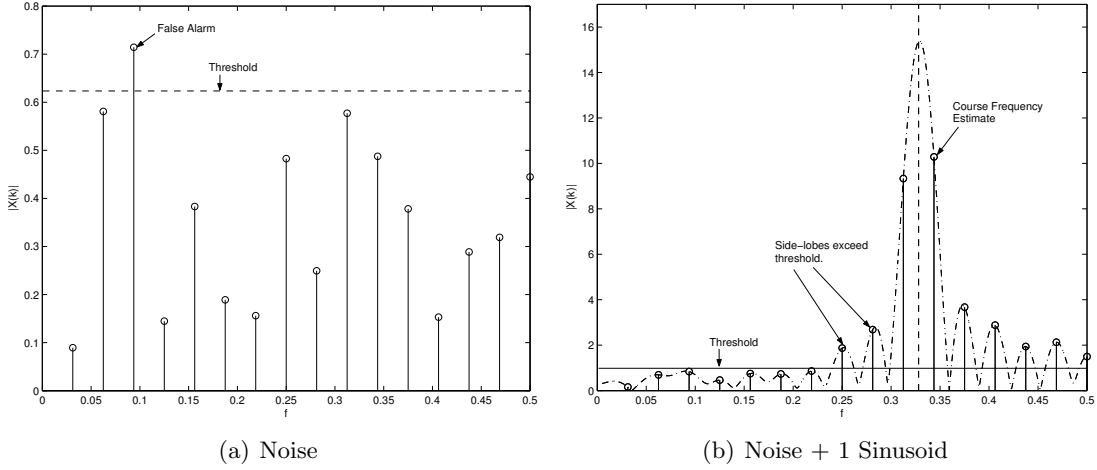


Figure 3.7: Threshold Demonstration with Noise and Noise+1 Sinusoid.

disregarded, and the presence of the weaker signal must be recognized. This is a difficult pattern recognition problem to implement in a machine [1]. Recall that the frequency estimate must be numerical. There is no human evaluating a DFS display.

A method employed to avoid the pattern recognition problem by the AFRL Laboratory exploits the prior knowledge of the spectral leakage shape to subtract the spectral leakage [9]. Thus, a method, referred to here as the Spectral Leakage Reduction (SLR) method, with the same general concept is proposed and analyzed here. The method entails the following steps

1. Find the peak of the DFS and ensure it is above threshold.
2. Estimate the high amplitude signal's frequency, amplitude, and phase.
3. Subtract the spectral leakage from the DFS (this subtraction would be accomplished via a lookup table with the actual system; for simulations, the DFS is calculated).
4. Find the peak of the subtracted DFS and check if it is above threshold.
5. Declare a detection if the peak is above threshold.

If the sinusoidal model is correct, the above method hinges on the accuracy of the frequency, phase, and amplitude estimates for accurate spectral leakage estimation. This method is similar to a method proposed in [20], although [20] is using the method to reduce bias for extremely accurate interpolation multiple frequency estimation (the approximate

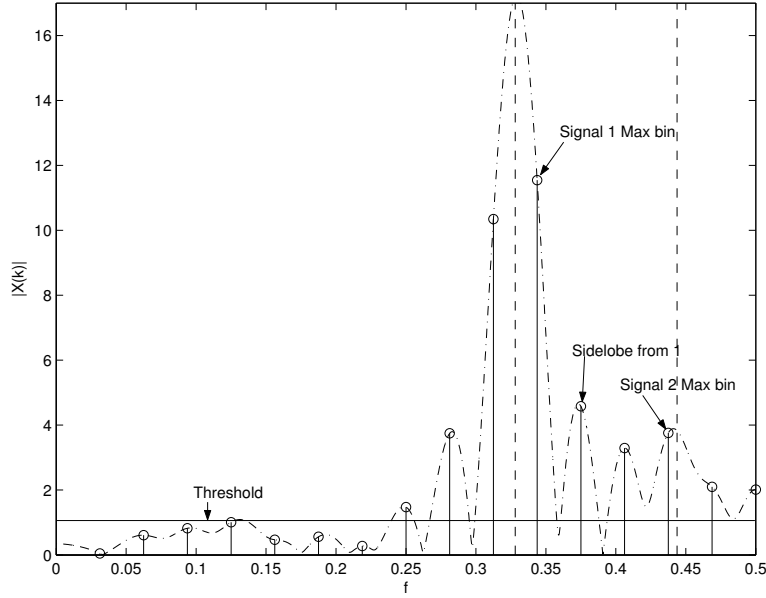


Figure 3.8: Two Sinusoid + Noise DFT Magnitude.

locations of the peaks are assumed known). Whereas, the SLR method is reducing the spectral leakage in order to detect low amplitude sinusoids in the presence of high amplitude sinusoids.

Figure 3.9 contains a plot of the signal DFT of Figure 3.8 with the spectral leakage of signal 1 compensated for by subtracting the DFT magnitude of signal 1 from the DFT magnitude of signal 1 and 2 + noise

$$\begin{aligned}
 X_{SLR}(k) &= |S_2(k) + S_1(k) + W(k) - \hat{S}_1(k)| \\
 &= |S_2(k) + W(k) + \mathbf{e}_{SLR}(k)|
 \end{aligned} \tag{3.20}$$

where $X_{SLR}(k)$ is the SLR method DFS (with the spectral leakage from signal one compensated for), $\hat{S}_1(k)$ is the estimated DFS of signal 1, $S_1(k)$ is the estimated DFS of signal 1, $W(k)$ is the DFS of the noise, $S_2(k)$ is the estimated DFS of signal 2 and \mathbf{e}_{SLR} is the error between the estimated signal 1 DFS and the actual DFS of signal 1. In Fig. 3.9(a), the first signal frequency is known exactly and, as expected, the compensation removes the side-lobes to below threshold, allowing the second signal to be detected via a threshold test, i.e. \mathbf{e}_{SLR} is very low. In Fig. 3.9(b), the frequency used to estimate the side-lobes is

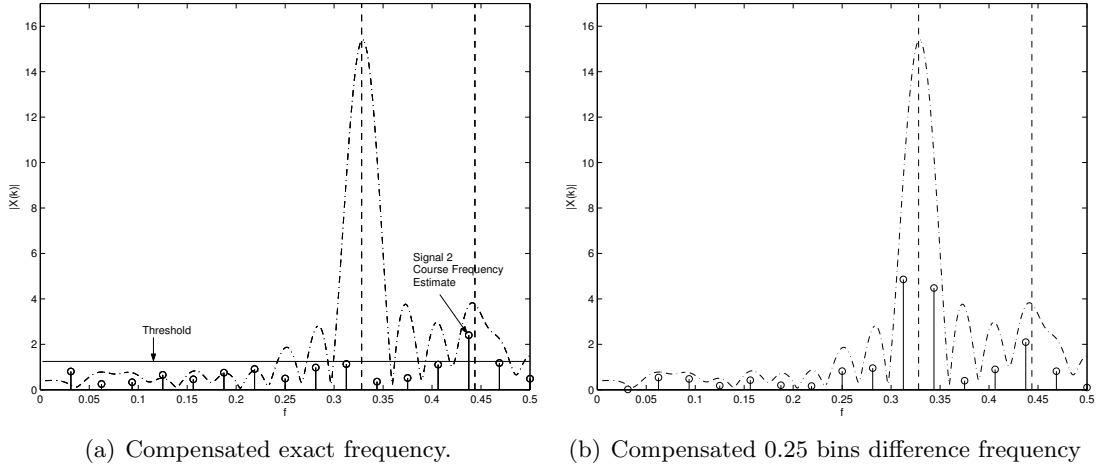


Figure 3.9: Sinc Lobe Compensation Demonstration.

at 10.75 bins and, as a result of the poor frequency estimate, the side-lobes are not adequately compensated for, i.e. a larger \mathbf{e}_{SLR} . Thus, good frequency estimates are required for the SLR method.

3.3.1 Frequency Interpolation Methods. DFS peak interpolation algorithms are developed in this section in order to estimate the frequency for the SLR method accurately. The algorithms analyzed are computationally efficient and only rely on the three DFS points closest to the actual sinusoids frequency (note that these three points contain $\geq 85\%$ of the signal energy [20]), thus they are suitable for EW applications. All algorithms are developed for the one *complex* sinusoidal signal condition, or cisoid, because there is no spectral leakage bias to contend with (for one real signal, the negative frequency image has spectral leakage in the positive frequency image). Simulations are performed to gauge the effect of the presence of one and two real sinusoids on algorithm performance.

3.3.1.1 Modulus Peak Position Interpolation. The first DFS interpolation algorithm, called here the Modulus Peak Position (MPP) interpolator, is discussed in [1,20]. The MPP estimates the points by using the largest DFS absolute value peak and the largest absolute value of the peak's two neighbors (the one also lying on the main lobe). It then interpolates the value in between them. The mathematics of this interpolation follows.

First, find the maximum DFS sample point magnitude, $\max(|X(k)|)$ equals $|X(p)|$. Next, find the neighboring peak with the highest absolute value amplitude and set the variable α according to the position, that is

$$\alpha = \begin{cases} 1, & \text{if } |x(p+1)| > |x(p-1)|; \\ -1, & \text{otherwise.} \end{cases} \quad (3.21)$$

Now, assume the DFS value is $X(\frac{\Delta}{N})$ where Δ is the distance from the true signal frequency in fractions of a bin $\frac{1}{N}(p + \Delta) = f$, where $\Delta \leq |0.5|$. Thus, the value is

$$X\left(\frac{\Delta}{N}\right) = N\beta \text{sinc}\left(\frac{\Delta}{N}\right) = \beta \frac{\sin(\pi\Delta)}{\pi\frac{\Delta}{N}} \quad (3.22)$$

where β is the continuous signal complex amplitude. The highest magnitude neighbor DFS value is

$$X\left(\frac{1-\Delta}{N}\right) = \beta \frac{\sin(\pi(1-\Delta))}{\pi(\frac{1-\Delta}{N})} \quad (3.23)$$

Now, Δ is interpolated as [1, 20]

$$\hat{\Delta} = \alpha \frac{|X(m+\alpha)|}{|X(m)| + |X(m+\alpha)|}. \quad (3.24)$$

The corresponding frequency estimate is

$$\hat{f} = (p + \hat{\Delta}) \frac{1}{N}. \quad (3.25)$$

where the sampling frequency is assumed one for the above development.

Figure 3.10 is an illustration of the above math. For larger Δ , as in Fig. 3.10(a), the amplitude difference is well pronounced between $|X(p-1)|$ and $|X(p+1)|$ (For this example $\alpha = -1$). For small Δ , as in Fig. 3.10(b), the amplitude difference is negligible and this will cause errors when noise is present.

Small systematic errors are present in all of the interpolation algorithms (including the above method) which cause a slight bias in the estimate [20]. When real signals are considered, the negative frequency image side-lobes introduce larger bias to the interpolator

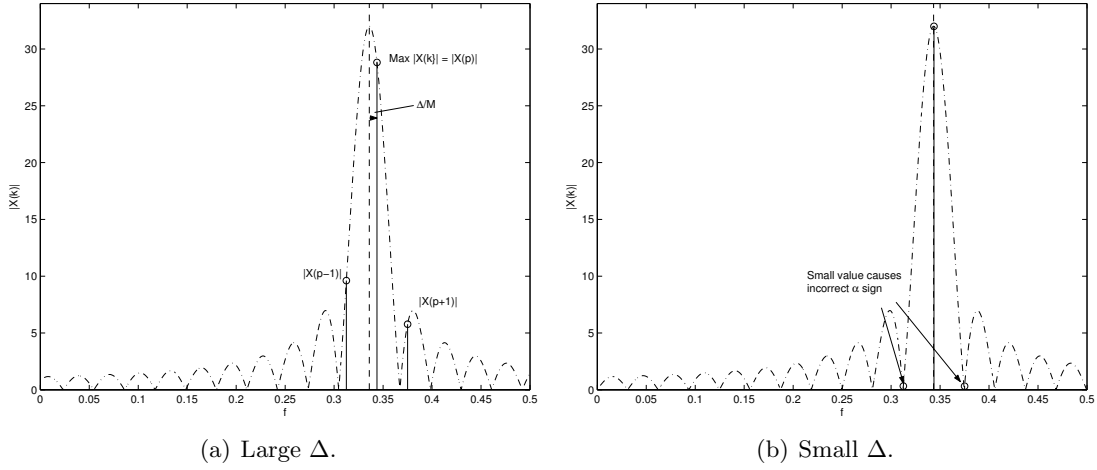


Figure 3.10: MPP concept illustration.

frequency estimates. Figure 3.11 contains a MPP *no noise* frequency estimate deterministic bias analysis for a single real sinusoid and complex cisoid with the following parameters: $[A_1 = 1, \phi_1 = 0]$. In the figure, the deterministic bias is calculated between the interpolated frequency, \hat{f}_Δ , and the actual frequency, f_Δ , for the bin positions indicated

$$\text{bias} = |f_\Delta - \hat{f}_\Delta| \quad (3.26)$$

at 0.01 intervals of Δ and plotted as $-10 \log_{10}(\text{bias})$ (which means good performance is plotted above bad performance). The negative frequency side-lobe aliasing into the positive frequencies causes an increase in bias of approx 30 dB at some points over the complex cisoid case. This real signal bias value varies according to the bin position. This real signal bias would be reduced by using a window based interpolator because of the associated spectral leakage reduction, but windowing adversely effects probability of detection and frequency resolution of close frequency signals.

Figure 3.12 contains a pseudocolor plot of a Monte Carlo (MC) MSE analysis for estimating a real sinusoid's frequency using the MPP interpolator with one real sinusoid and noise, where MSE is calculated as

$$MSE_{var} = \frac{1}{M} \sum_{i=1}^M (f_\Delta - \hat{f}_\Delta^i)^2. \quad (3.27)$$

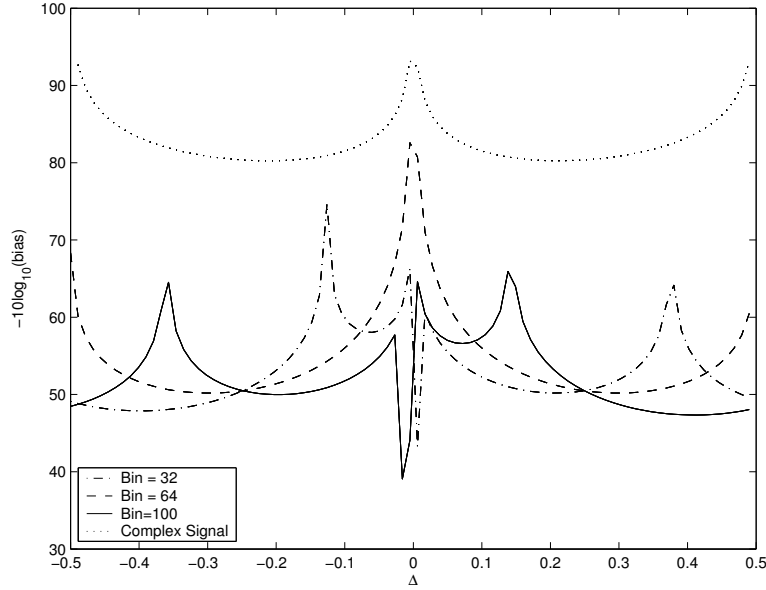


Figure 3.11: Deterministic bias of MPP interpolator for real and complex signals.

where M is the number of Monte Carlo trials and \hat{f}_{Δ}^i is the i th frequency estimate of the MC trial. For the intercept receiver simulations, the phase is randomly distributed between 0 and 2π . The plot is generated by performing 1000 MC trials at each of 33 evenly spaced Δ from bin 32 and repeating for each SNR step with simulation parameters: $[A_1 = 1, \phi_1 = U[0, 2\pi]]$, $N=256$. The color bar indicates the $-10 \log_{10}(MSE)$, thus the higher the value, the better the estimate. From the plots, the MPP interpolator performance significantly degrades for low Δ values. This poor performance is due to the α sign being switched at low Δ , which introduces a larger error and bias. Also, the bias from the real signal spectral leakage dominates the MSE above 30 dB SNR, which is why the MSE values plateau at this point.

3.3.1.2 Phase Based Interpolator. Because of inaccuracy in determining α for low Δ , the following phase based interpolation algorithms, called the Phase Based Interpolator (PBI), is introduced to overcome this deficiency [20]. First, the two neighboring DFS bins phase $X(\alpha)$ are referenced to the largest bin's phase and then the real part of

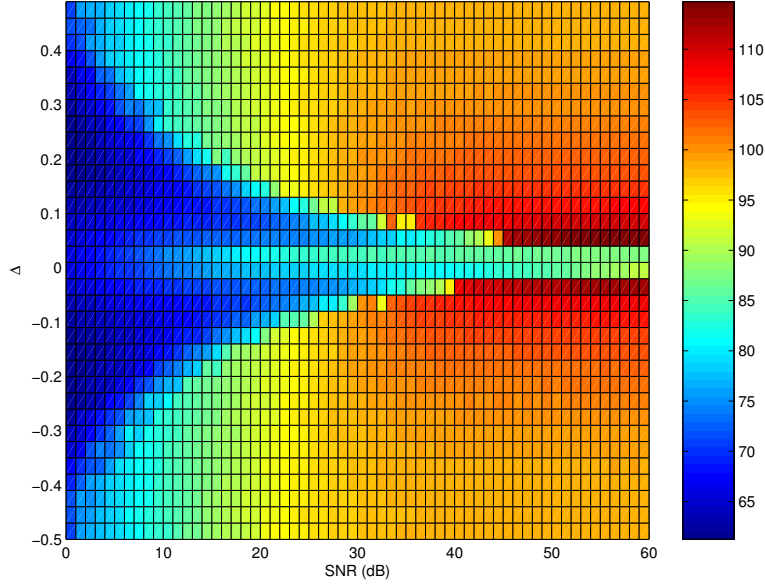


Figure 3.12: MPP Interpolator MSE versus Δ and SNR. Color bar indicates value of $-10\log_{10}(MSE)$. Thus the higher the value is, the better the performance.

this operation is taken [20]

$$V(\mu) = \text{Re}\{X(p + \mu)X^*(p)\} \quad (3.28)$$

where $V(\mu)$ is called the Phase Indexed Variable (PIV). The following test is used to calculate $\hat{\Delta}$ [20]

$$\text{iff } V(-1) - V(1) > 0, \hat{\Delta} = \hat{\Delta}_+, \text{ else } \hat{\Delta} = \hat{\Delta}_-. \quad (3.29)$$

where $\hat{\Delta}_+$ and $\hat{\Delta}_-$ are defined as [20]

$$\hat{\Delta}_+ = \frac{-V(1)}{V(0) - V(1)} \quad \hat{\Delta}_- = \frac{V(-1)}{V(0) - V(-1)}. \quad (3.30)$$

As Δ approaches zero, $V(1) \approx V(-1)$ and the PBI estimate exhibits much less error than the MPP.

Figure 3.13 contains a PBI *no noise* frequency estimate bias analysis for a single real sinusoid and complex cisoid with the same setup as Fig. 3.11. The negative frequency sidelobe aliasing into the positive frequencies causes an increase in bias of approx 20 dB at

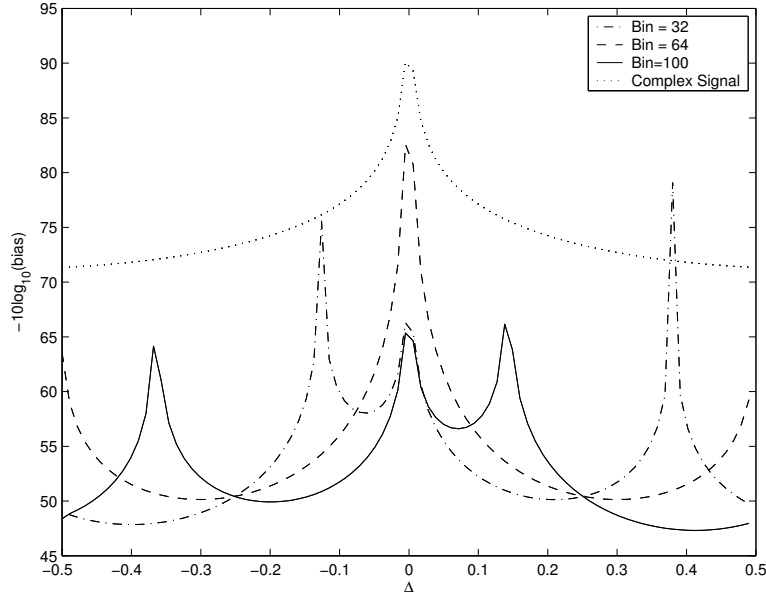


Figure 3.13: Deterministic bias of PBI interpolator for real and complex signals.

some points over the complex cisoid case. This real signal bias value varies according to the bin position, which is no different than the MPP. The PBI complex cisoid bias is slightly higher than the MPP bias. However, the PBI does not experience the jagged increase in bias at low Δ .

Figure 3.14 contains a pseudocolor plot of a MC MSE analysis for estimating a real sinusoid's frequency using the PBI interpolator with one real sinusoid and noise with the same setup as Fig. 3.12. From comparing Fig. 3.14 to Fig. 3.12, the PBI performance significantly improves for low Δ values over the MPP, which is expected because of the phase referencing to decrease the increased MPP bias associated with picking the wrong α value. Also, the bias from the real signal spectral leakage dominates the MSE above 30 dB SNR, which is why the MSE values plateau at this point (except for the spike locations in 3.13 for bin 32).

3.3.1.3 Gamma Phase Based Interpolator. The PBI can also be improved upon by using the following algorithm, the Gamma Phase Based Interpolator (GPBI). When Δ is small, $V(1)$ and $V(-1)$ provide independent estimates of Δ . Thus, some estimation gain over PBI is gained by averaging the two [20]. In [20], the following average is

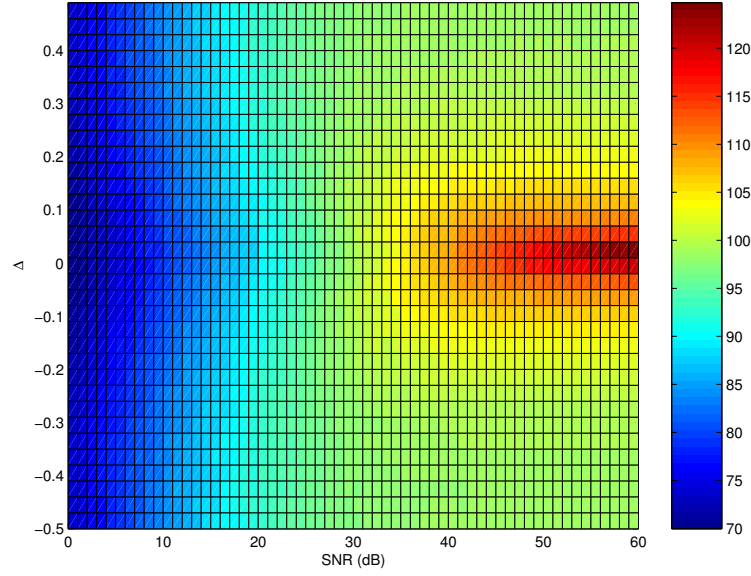


Figure 3.14: PBI Interpolator MSE versus Δ and SNR. Color bar indicates value of $-10\log_{10}(MSE)$. Thus the higher the value is, the better the performance.

proposed

$$\gamma = \frac{V(-1) - V(1)}{2V(0) + V(-1) + V(1)}. \quad (3.31)$$

Using γ , Reference [20] gives the $\hat{\Delta}$ estimate as

$$\hat{\Delta} = \frac{\sqrt{1 + 8\gamma^2} - 1}{4\gamma}. \quad (3.32)$$

Figure 3.15 contains a GPBI *no noise* frequency estimate bias analysis for a single real sinusoid and complex cisoid with the same setup as Fig. 3.11. The negative frequency side-lobe aliasing into the positive frequencies bias is reduced from the PBI and MPP by using the gamma interpolator. The GPBI complex cisoid bias is also slightly higher than the MPP cisoid bias. Again, however, the GPBI does not experience the jagged increase in bias at low Δ .

Figure 3.16 contains a pseudocolor plot of a MC MSE analysis for estimating a real sinusoid's frequency using the PBI interpolator with one real sinusoid and noise with the same setup as Fig. 3.12. From the plots, the GPBI shows some improvement over the

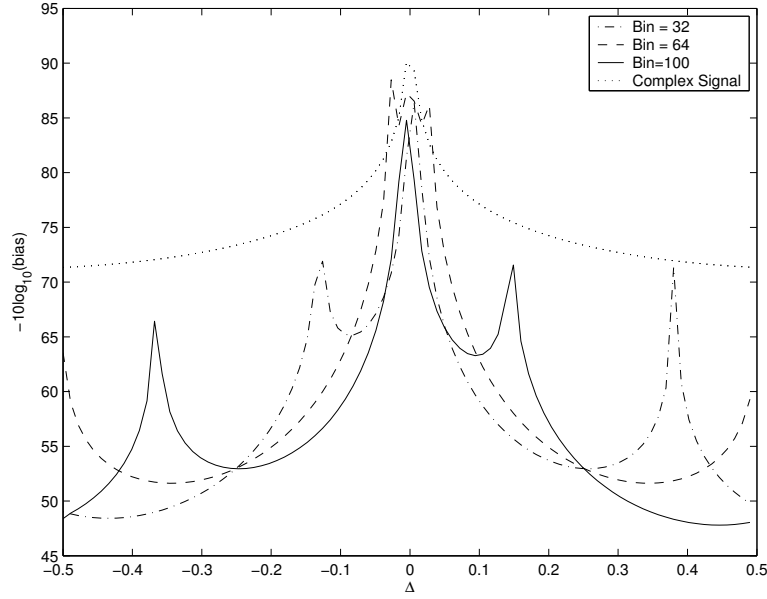


Figure 3.15: Deterministic bias of GPBI interpolator for real and complex signals.

PBI and marked improvement over the MPP. Also, the bias from the real signal spectral leakage dominates the MSE above 30 dB SNR, which is why the MSE values plateau at this point.

3.3.1.4 Two Sinusoid Interpolator Performance. With two sinusoids, the interpolator estimate bias increases. Figure 3.17 is a two sinusoid bias analysis of the interpolator algorithms for the following parameters: $[A_1 = 1, \phi_1 = 0]$, $[A_2 = 0.8, \phi_2 = 0]$. Three bin positions are considered for the first sinusoid: 32, 64, and 100. The second sinusoid is at bin 35.5 for maximum leakage. Sinusoids within 2 bins will be considered high resolution for the DFT-based intercept receiver and are not considered in this Chapter [9]. For reference, the bias of using $|X(p)|$ as an estimate is plotted. For the MPP estimate in Fig. 3.17(a), the low Δ performance decreases considerably; below using the FFT bin $|X(p)|$ as the estimate. The PBI and GPBI for Figures 3.17(b) and 3.17(c) both outperform using the FFT bin as the estimate, with the GPBI performing the best of the three interpolation algorithms. In terms of IDR, the 2 sinusoid interpolator bias decreases as the IDR increases, which is good in terms of estimating the spectral leakage. In other

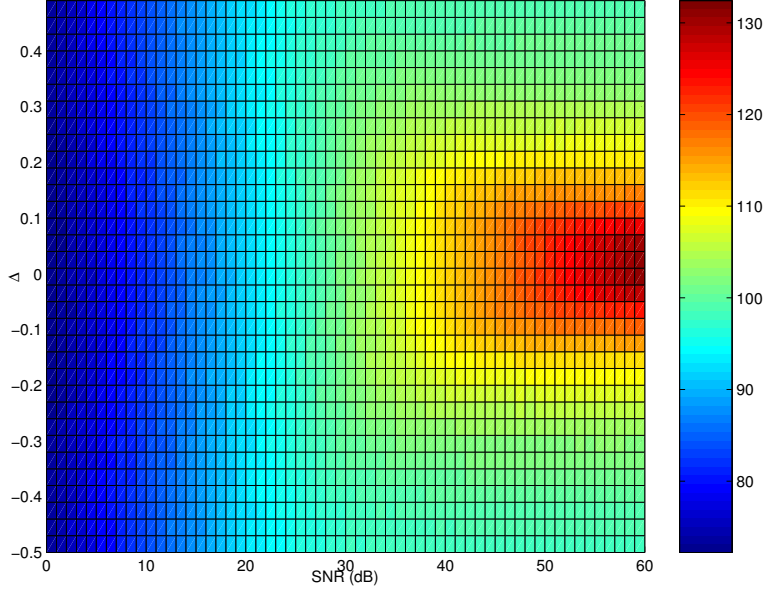
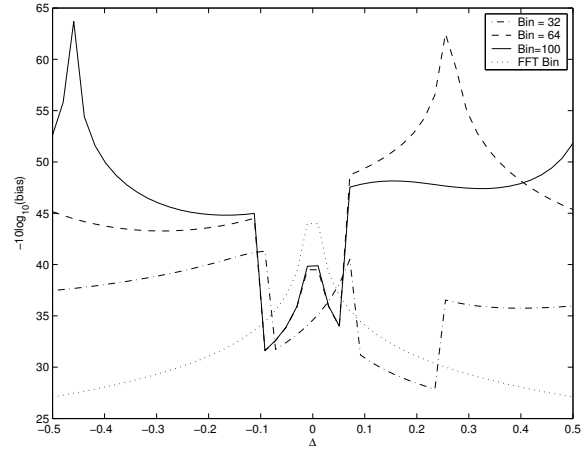


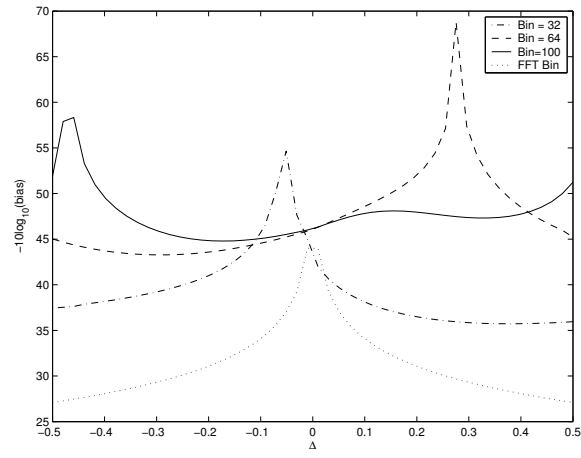
Figure 3.16: GPBI Interpolator MSE versus Δ and SNR. Color bar indicates value of $-10\log_{10}(MSE)$. Thus the higher the value is, the better the performance.

words, the estimate performance improves as the IDR increases, which in turn means the spectral leakage estimate is improving, which is a desirable characteristic.

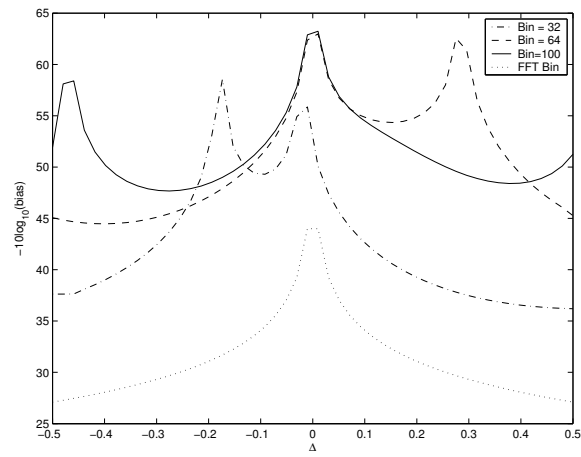
Figure 3.18 contains a pseudocolor plot of a two sinusoid MSE analysis of the interpolator algorithms with the same signal parameters as Fig. 3.17 except the phase is uniformly distributed for both signals between 0 and 2π . The colorbar indicates the value of $-10\log_{10}(MSE)$ between f_1 and \hat{f}_1 for 1000 MC runs at the specified SNR and Δ value. The first sinusoid is centered at bin 32 with 34 Δ evenly distributed around the bin. The second sinusoid is located at bin 35.5 for maximum leakage with the amplitude ratio of the signals maintained the same as Fig. 3.17. The close proximity of frequency and amplitude of the first signal to the second signal makes this a demanding test. As expected, the MPP algorithm exhibits the worst MSE performance of the three interpolation algorithms, especially for small Δ . The GPBI algorithm exhibits a slightly better performance than the PBI. Above 20 dB SNR, the MSE of all of the algorithms is dominated by the bias. Once again though, the estimate performance improves as the IDR increases, which in turn means the spectral leakage estimate is improving, which is a desirable characteristic.



(a) MPP

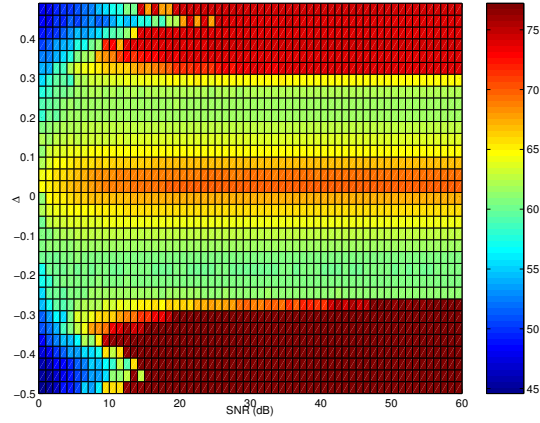


(b) PBI

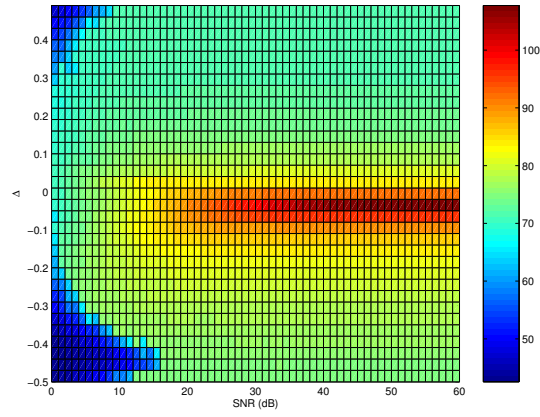


(c) GPBI

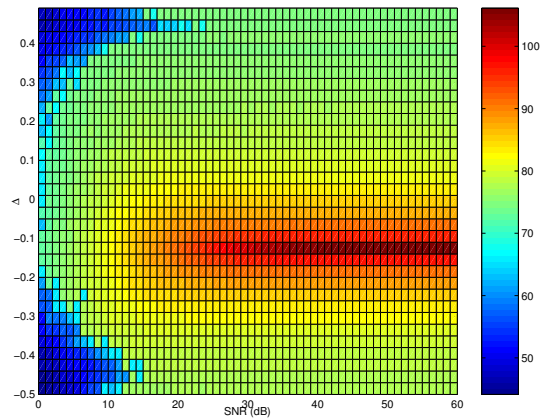
Figure 3.17: Interpolator 2 Sin Bias.



(a) MPP



(b) PBI



(c) GPBI

Figure 3.18: Interpolator 2 Sin interpolator estimate \hat{f}_1 MSE versus Δ and SNR. Colorbar indicates $-10\log_{10}(MSE)$ value.

3.4 SLR Method Analysis

As discussed in the introduction to this section, the following algorithm, called the SLR Method, is proposed to increase weak signal detection/estimation performance using the frequency interpolation algorithms developed above.

1. Calculate the signal DFT, the DFS.
2. Find the DFS maximum $\max(|X(k)|) = |X(p)|$, and check if above threshold.
3. Interpolate signal frequency, amplitude, and phase using interpolation algorithms.
4. Subtract estimated spectral leakage of large signal values from DFS .
5. Check if the maximum subtracted DFS bin, $\max(X_{SLR}(k)) = X_{SLR}(p)$, is above threshold.

For the above interpolation algorithms, the amplitude of the sinc peak, \hat{a} , is estimated as [20]

$$\hat{a} = |B| \frac{(1 - |\hat{\Delta}|)}{(1 - 2|\hat{\Delta}| + 2\hat{\Delta}^2)} \left(\frac{\pi \hat{\Delta}}{\sin(\pi \hat{\Delta})} \right). \quad (3.33)$$

where B is a weighted combination of the peak $X(p)$ and the peak's largest neighbor

$$B = (1 - |\hat{\Delta}|)X(p) - |\hat{\Delta}|X(p + \alpha). \quad (3.34)$$

For real signals, the signal amplitude is obtained from the sinc peak amplitude using $A_i = \frac{2\hat{a}}{N}$. The signal phase is estimated as [20]

$$\hat{\phi}_i = \arg(B) - \pi \hat{\Delta}. \quad (3.35)$$

3.4.1 SLR Error Analysis. As stated previously, the effectiveness of the SLR method hinges on how well the side-lobes have been estimated, which depends on the frequency (i.e. centering), amplitude, and phase estimates. Figure 3.19(a) contains a plot of the mean spectral leakage estimate error versus bins and Signal 1 SNR from a 1000 trial MC trial using the GPBI algorithm for frequency estimates for the following simulation parameters: $[f_1 = 32 + \Delta \text{ bins}, \phi_1 = U[0, 2\pi]]$, Signal 2 SNR=10 dB, $[f_1 =$

$35 + \Delta$ bins, $\phi_2 = U[0, 2\pi]$, $N=256$. The Δ values are uniformly distributed between -0.5 and 0.5 for the MC simulation. The estimated DFS spectral leakage for signal 1 is estimated as (the real system would use a look-up table)

$$\hat{S}_1(k) = \text{DFS}\{\hat{A}_1 \cos(2\pi \hat{f}_1 + \hat{\phi}_1)\} \quad (3.36)$$

The error is calculated in dB as

$$\mathbf{e}_{SLR}^m(k) = 20 \log_{10} \left(\frac{1}{M} \sum_{i=1}^M |S_1(k) - \hat{S}_1^i(k)| \right) \quad (3.37)$$

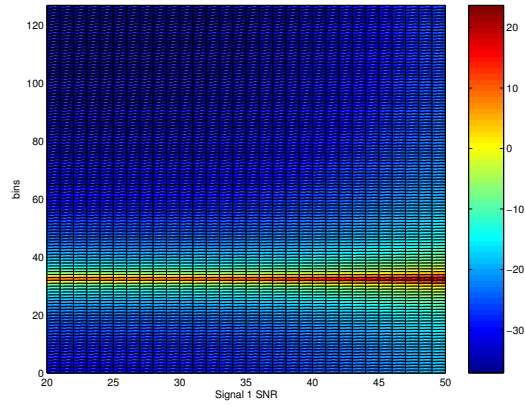
where $\mathbf{e}_{SLR}^m(k)$ is the mean error for the k th bin. The mean estimated spectral leakage error is extremely small except near the peak which is expected since any percentage error is higher near the peak since the spectral leakage is higher (the peak and its two neighbors used for interpolation are ignored for detection purposes in the SLR method). Also the mean error increases as SNR 1 increases which is also expected because the magnitude of the spectral leakage increases.

For comparison to the mean error, the signal 1 spectral leakage versus bins and Signal 1 SNR is plotted in Fig. 3.19(b). The mean error is close to 55 dB down from the associated Signal 1 Spectral leakage in most places.

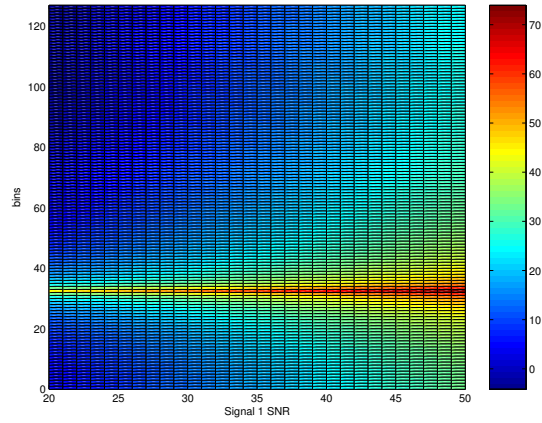
Figure 3.19(c) contains a plot of the estimated spectral leakage for signal 1. The variance is relatively small, except near the signal 1 peak which is expected due to the large swing in values from varying Δ values.

The above analysis confirms that the SLR method compensates for the signal 1 spectral leakage. Thus, the next step is to determine how well the SLR method performs estimation/detection of the signal 2 through simulation.

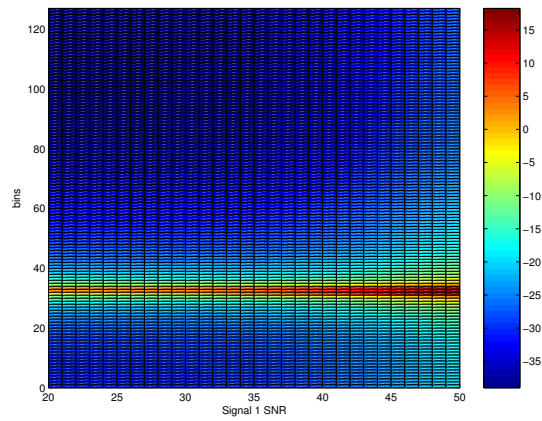
3.4.2 SLR Simulation Description. With so many variables in play, the best method is for a robust MC simulation to determine the Probability of Detection P_d and the Probability of False Alarm P_{fa} due to spectral leakage for a given noise threshold. The simulation is setup as follows:



(a) Mean SLR Error



(b) Signal 1 Spectral Leakage



(c) Variance SLR Error

Figure 3.19: Spectral Leakage Estimate Error Statistics vs. Signal 1 SNR and Bins. Colorbar indicates dB value of parameter.

1. Generate M N-length AWGN sequences, where M is the number of MC trials (set an arbitrary noise power, in the plots $\sigma^2 = 0.01$ is used).
2. Calculate the noise DFS of each N-length sequence.
3. Set the noise threshold by taking the max magnitude of each of the M N-length noise sequences for the positive frequency bins. Then, sorting the max values by magnitude and setting the threshold at the 10th highest value (for a noise only P_{fa} of $\frac{10}{M}$).
4. Specify center bins for two signals.
5. Generate M uniformly distributed Δ_1 and Δ_2 values and add to the corresponding center bins.
6. Generate the M N-length two sinusoids sequences for the generated Δ values for a specified Signal 1 SNR and Signal 2 SNR.
7. Calculate the DFS of the 2 sinusoids plus noise measurements.
8. Interpolate the Signal 1 frequency, amplitude and phase using one of the frequency interpolation algorithms (assuming Signal 1's amplitude is above threshold, which it is for all simulations).
9. To simulate a perfect look-up table, calculate the the signal 1 spectral leakage with estimated frequency, amplitude, and phase as in (3.36).
10. Subtract the estimated signal 1 DFS from the DFS of the 2 sinusoids plus noise and take the absolute value as in (3.20).
11. Perform a threshold check to see if any bin values exceed the threshold, ignoring the max Signal 1 DFT bin and its two closest neighbors⁷; i.e. the ones involved with the Signal 1 interpolation. a.) If the threshold is not exceeded, nothing is declared (Signal 2 is not detected). b.) If the threshold is exceeded for any bin, find the maximum bin value. If the maximum bin value is within 1 bin of the signal center bin a detection is declared, i.e. if true f_2 is 40.3, the threshold exceeded at bins 39,

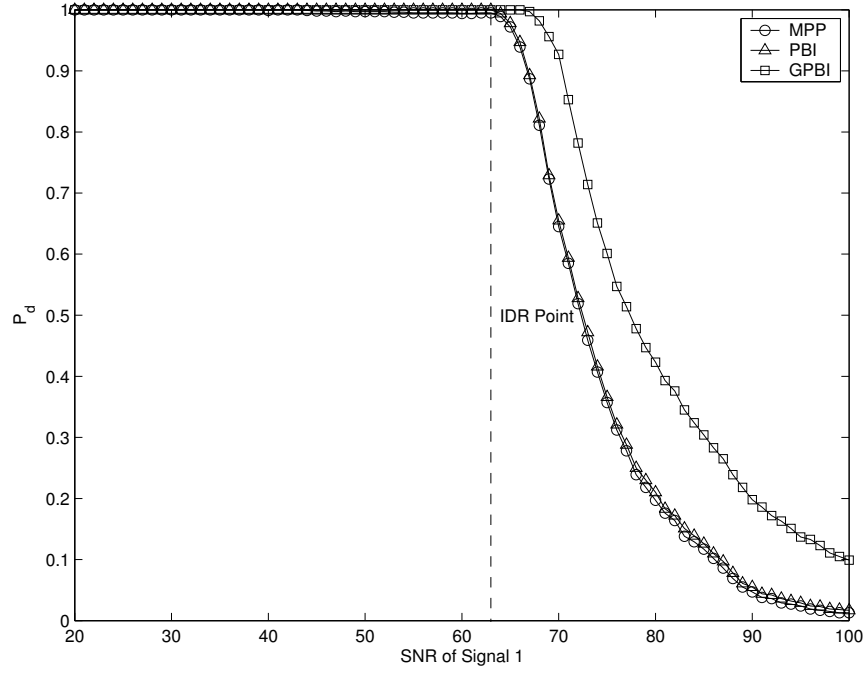
⁷Signals within 2 bins are considered high resolution in this thesis and are not considered for the DFT intercept receiver, they are analyzed in the IGLS parametric receiver in Chapter V.

40, and 41 would all be declared detections. c.) If the threshold is exceeded by other bins, a false alarm is declared.

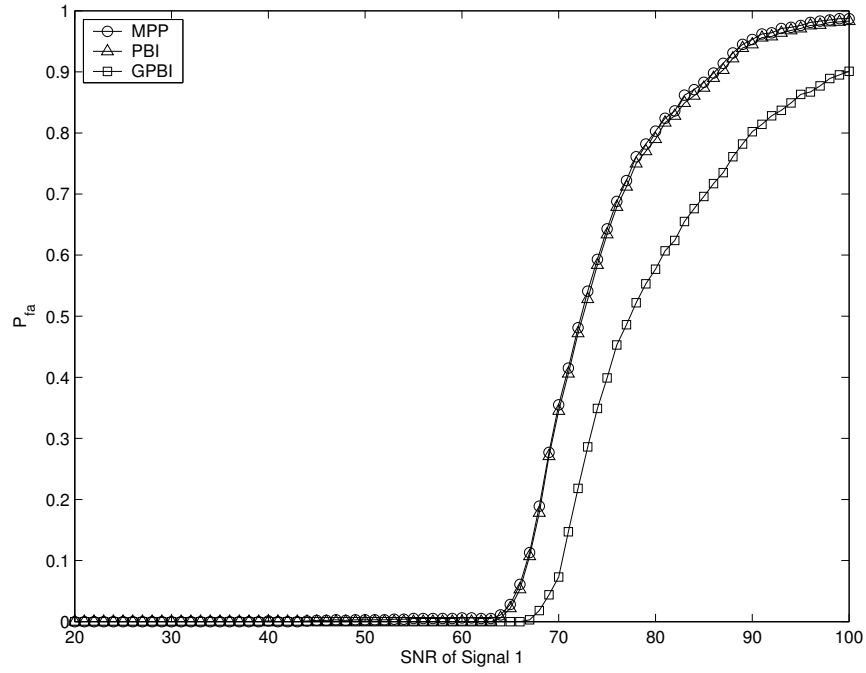
3.4.3 SLR Simulation Results. Figure 3.20 contains the P_d and P_{fa} for the MC simulation described above with the following simulation parameters: $[f_1 = 32 + \Delta \text{ bins}, \phi_1 = U[0, 2\pi]]$, $[f_1 = 36 + \Delta \text{ bins}, \phi_2 = U[0, 2\pi]]$, $N=256$, $\Delta = U[-0.5, 0.5]$. The second signal SNR is fixed at 10 dB (for a sinc peak that is well above the detection threshold), and the first signal SNR is increased at 1 dB increments. The threshold for the simulation is set at 0.01 P_{fa} for noise only by generating the 1000 trials of noise, thus the false alarms are for sinc sidelobes from signal 1 exceeding the threshold. The second signal is detected with a P_d of 1 until the signal 1 SNR exceeds 63 dB for the MPP and PBI algorithms, and 67 dB for the GPBI algorithm. Detection and false alarm performance deteriorates from this Signal 1 SNR value up. Thus for a P_d of 1, the IDR when the signals are this close is $63 - 10 = 53$ dB for the MPP and PBI algorithms, and $67 - 10 = 57$ dB for the GPBI algorithm. The MPP and PBI performance is similar because their signal 1 estimation performance is similar except for low Δ where there is little spectral leakage to contend with. The GPBI slightly outperformed the MPP and PBI algorithms across all Δ values, thus the GPBI has a slightly higher IDR.

Figure 3.21 contains the P_d and P_{fa} for the MC simulation described above with signal 2 centered at bin 64. The performance mirrors the performance for bin 36 in 3.21.

Figure 3.22 contains the P_d and P_{fa} for the MC simulation described above with signal 2 centered at bin 100. The performance mirrors the performance for bin 36 in 3.21. Thus, using the SLR method, the IDR has little dependence on frequency separation, which is an excellent property. This frequency separation independence can be explained by examining the histogram of the maximum bin for the compensated DFT at an SNR of 70 dB in Figure 3.23. The detections are clustered around bin 100 as expected, and the false alarms are all clustered at bin 30 and 34, which is where the spectral leakage is greatest in the signal 1 DFT (recall that bins 31, 32, and 33 are not considered because they are used by the interpolation algorithm). Which means that because of the signal 1 magnitude, the compensated spectral leakage of signal 1 is exceeding the signal 2 bins

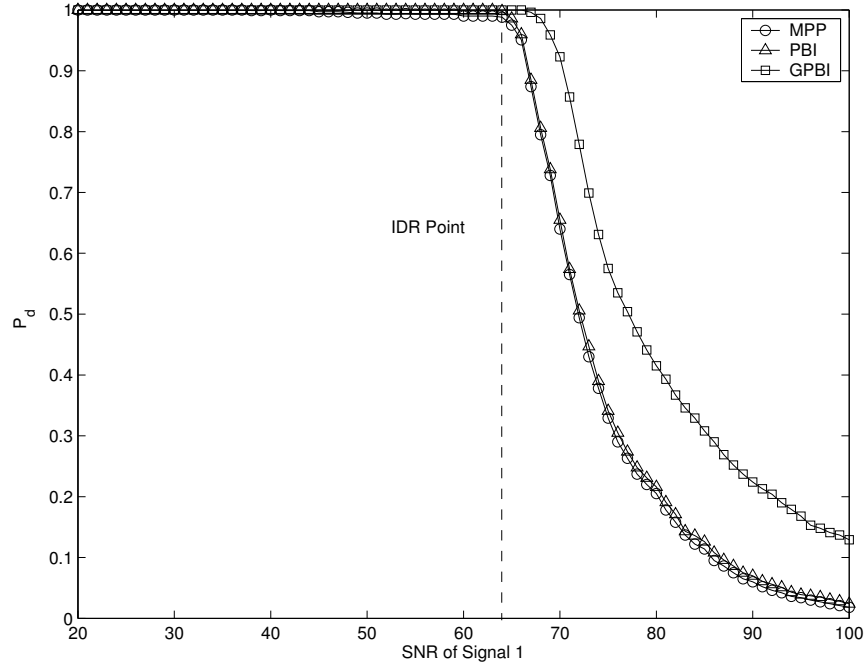


(a) Bin 36 P_d

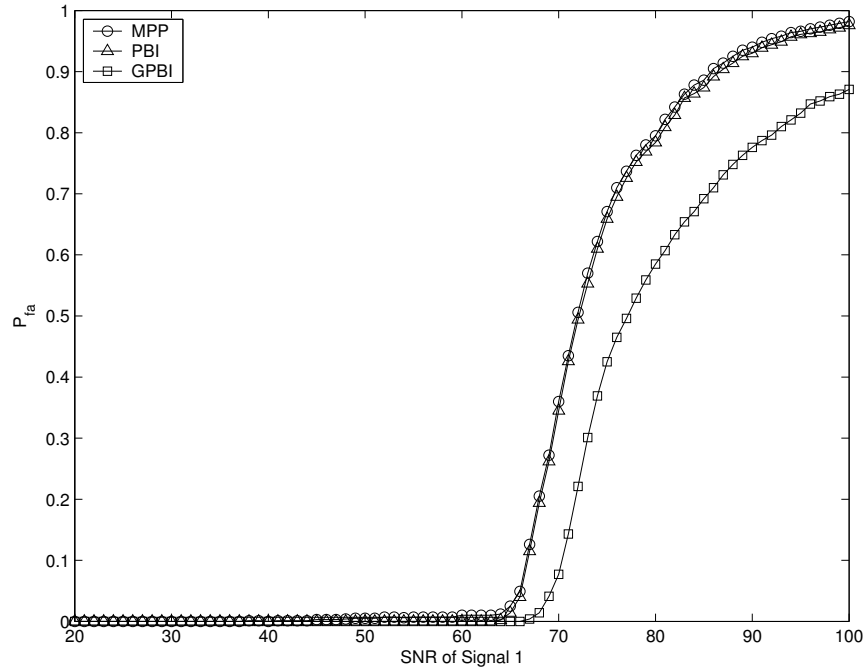


(b) Bin 36 P_{fa}

Figure 3.20: P_d and P_{fa} results for SLR method (Noise alone $P_{fa} = 0.01$, Signal 1 bin 32)).



(a) Bin 64 P_d



(b) Bin 64 P_{fa}

Figure 3.21: P_d and P_{fa} results for SLR method (Noise alone $P_{fa} = 0.01$, Signal 1 bin 32)).

Table 3.1: SLR IDR results (Noise only $P_{fa} = 0.01$)

f_{req}	Signal 2 SNR	Freq Sep	GPBI IDR
$f_{req} < 1.5$ bins	10 dB	4 bins	57 dB
$f_{req} < 1.5$ bins	10 dB	32 bins	57 dB
$f_{req} < 1.5$ bins	10 dB	68 bins	57 dB

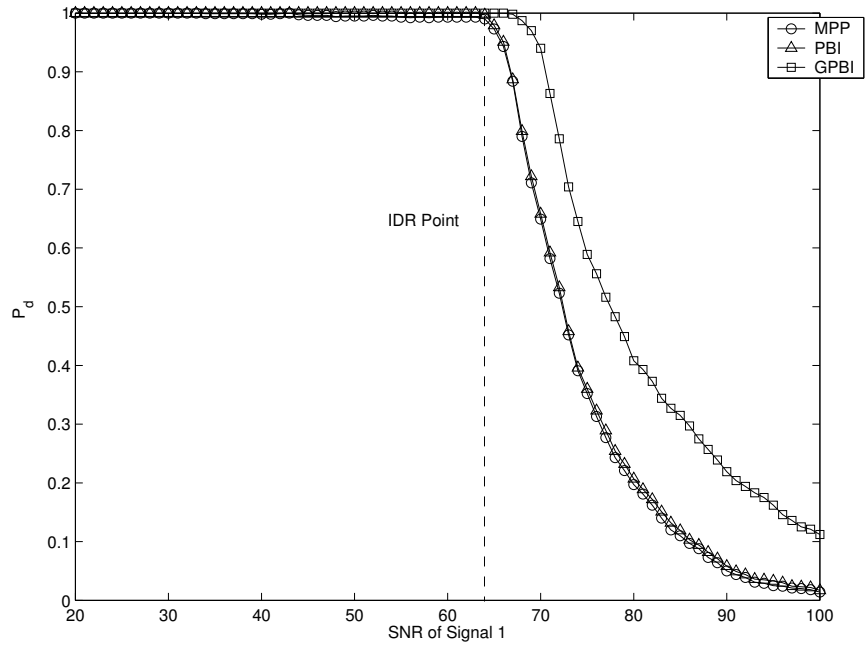
maximum height, most likely for large Δ values. The P_d and P_{fa} gracefully degrades as lower and lower Δ values compensated spectral leakage exceeds the signal 2 bins maximum height. The false alarms are clustered around the same 2 bins for simulations when signal 2 is centered around bins 64 and 36 also.

In Figure 3.24, the first signal SNR is set at 15 dB, and the SNR of Signal 2 is slowly increased until detected with a P_d of one at -2 dB for simulation parameters: $[f_1 = 32 + \Delta \text{ bins}, \phi_1 = U[0, 2\pi]]$, $[f_1 = 100 + \Delta \text{ bins}, \phi_2 = U[0, 2\pi]]$, $N=256$, $\Delta = U[-0.5, 0, 5]$. This can be considered the detection threshold limited detection scenario. Notice that all three methods exhibit the same performance since the side-lobes of signal are well compensated by all three methods to below the detection threshold. This threshold prevents false alarms from the noise, and thus is not considered to limit IDR.

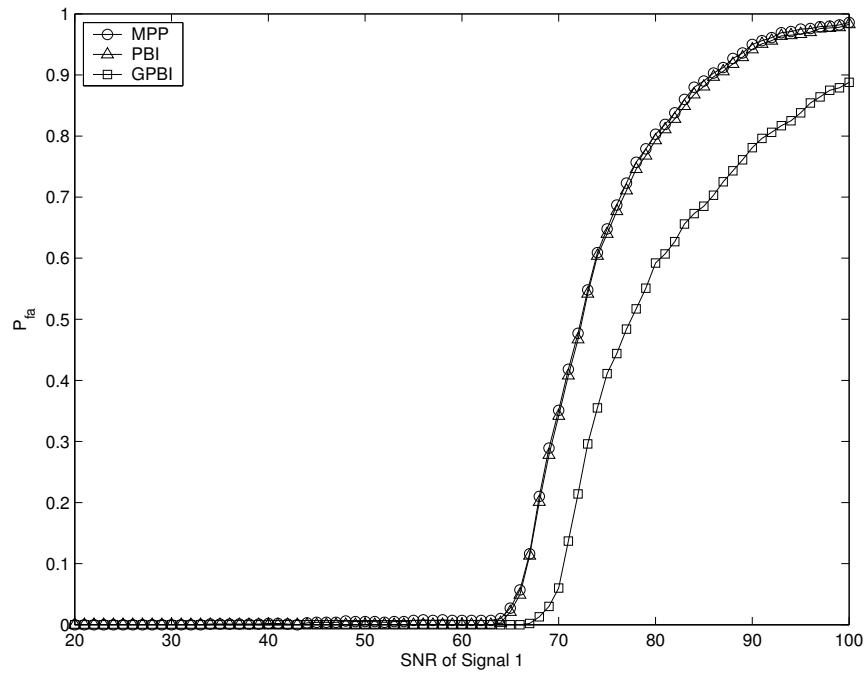
3.4.4 SLR IDR Results. The SLR method provides coarse numerical frequency estimates which is an EW requirement. Table 3.1 summarizes the SLR IDR results for the thesis definition of IDR. In the table, f_{req} is the required detection frequency accuracy (note that since the intercept receiver is detecting and quantizing that this is not the Mean Square Error accuracy). This number is worst case, most likely the worst case accuracy is $f_{req} < 1$ bin. Future work could analyze employing an interpolation algorithm on the signal 2 peak to improve frequency estimates.

3.5 Conclusion

A DFT-based intercept receiver is analyzed without and then with noise. With no noise, it is shown that the DFT-based intercept receiver IDR is limited by spectral leakage that is exclusively a result of finite measurement time. To handle spectral leakage, the novel SLR method is analyzed for its IDR performance in white noise using a detection threshold



(a) Bin 100 P_d



(b) Bin 100 P_{fa}

Figure 3.22: P_d and P_{fa} results for SLR method (Noise alone $P_{fa} = 0.01$, Signal 1 bin 32)).

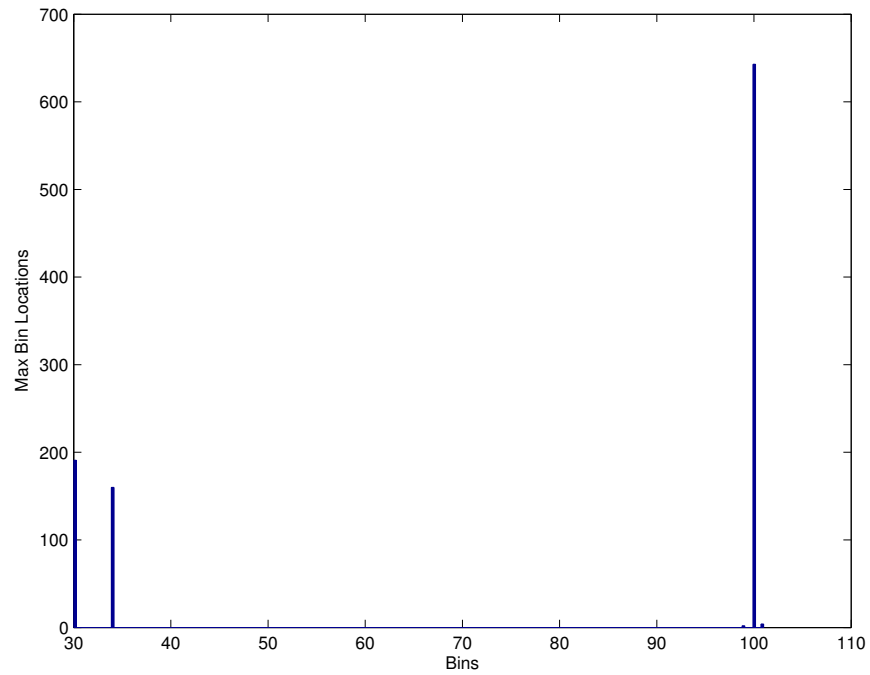


Figure 3.23: Histogram of SLR compensated DFT detections (Noise alone $P_{fa} = 0.01$, Signal 1 bin 32, Signal 2 bin 100).

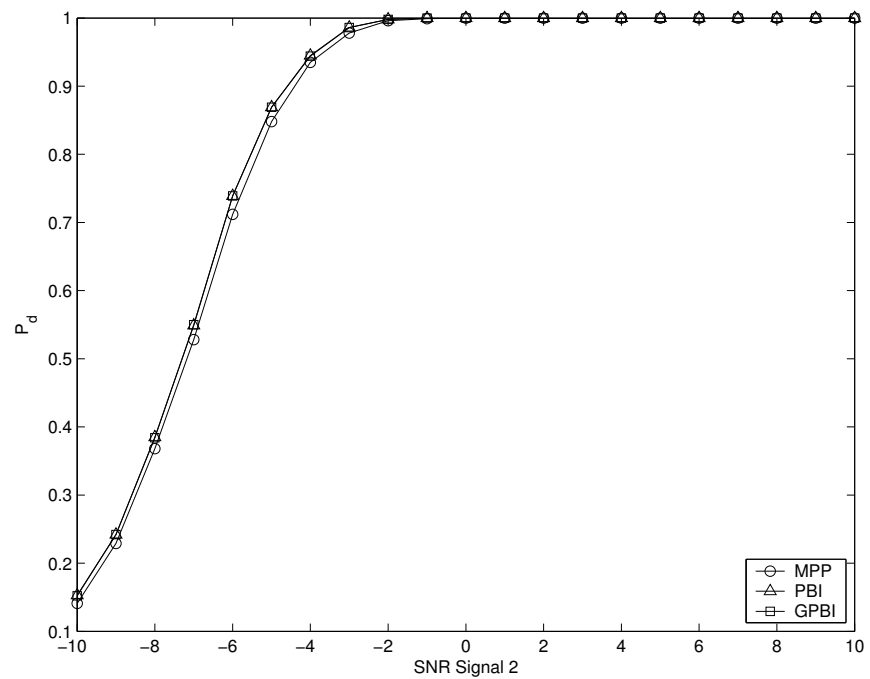


Figure 3.24: SLR method P_d for low SNR 1 (Noise alone $P_{fa} = 0.01$, Signal 1 bin 32).

scheme. The method's IDR performance is shown to have little frequency separation dependence and provides high IDR with the required numerical frequency estimates.

Because of the spectral leakage biasing the estimates, it is very difficult, if not impossible, to achieve optimal (ML) estimates using only the DFT. However, if the number of sinusoids present in the measurement is known already, optimal estimates can be obtained. This optimal estimate analysis is the topic of the next two chapters.

IV. Cramer-Rao Bound for Instantaneous Dynamic Range

! For Chapters IV and V in the thesis, the number of signals present in the measurement is assumed known.

4.1 Introduction

Before the discussion of the IGLS algorithm-based parametric receiver in Chapter V, a natural question is what is the best IDR that can be achieved for a desired RMS frequency estimation accuracy. For unbiased estimators, the Cramer-Rao Bound (CRB) is used to provide a lower bound on the MSE of the estimates [11–13]. The CRB is a lower bound for the variance of any unbiased ML Estimator. Thus, the IDR-CRB is derived below. Section 4.2 derives the multiple frequency CRB originally derived by Rife [6]. The multiple frequency CRB is modified by the author in Section 4.3 to arrive at the IDR-CRB for complex and real signals.

4.2 Derivation of the CRB for Multiple Sinusoids in AWGN

In this section, the CRB for multiple sinusoids in white noise, originally derived by Rife in [6], is derived. First, in Section 4.2.1, the multiple sinusoid CRB is derived for complex signals. Next, in Section 4.2.2, the complex signals' CRB [6] is extended to develop the real signals' CRB.

4.2.1 Complex Signal CRB. Consider the following complex sinusoidal signal vector, \mathbf{s}_c , with unknown parameters

$$s_c(n) = \sum_{i=1}^p A_i \exp\{j(\omega_i n + \phi_i)\} = \sum_{i=1}^p A_i \mathbf{h}(\omega_i, \phi_i). \quad n = 0 \dots N-1 \quad (4.1)$$

Let the unknown parameter vector $\boldsymbol{\theta}$ be defined as

$$\boldsymbol{\theta} = [\omega_1 \ A_1 \ \phi_1 \ \dots \ \omega_p \ A_p \ \phi_p]. \quad (4.2)$$

The signal \mathbf{s}_c is combined in a transmission channel with noise to form the measurement vector

$$\mathbf{x}_c = \mathbf{s}_c + \mathbf{w}_c, \quad (4.3)$$

where \mathbf{w}_c is complex noise distributed as

$$\mathbf{w}_c = \mathcal{N}(0, \mathbf{R}). \quad (4.4)$$

Since \mathbf{x}_c is a linear combination of a Gaussian distributed random variable, \mathbf{x}_c is itself a Gaussian distributed random variable

$$\mathbf{x}_c = \mathcal{N}(\mathbf{s}_c, \mathbf{R}). \quad (4.5)$$

Thus, the Probability Density Function (PDF) of \mathbf{x}_c (with the complex noise assumption) is [13]

$$f_{\theta}(\mathbf{x}_c) = (\pi\sigma^2)^{-N} |\mathbf{R}|^{-1} \exp \left\{ -(\mathbf{x}_c - \mathbf{s}_c)^H \mathbf{R}^{-1} (\mathbf{x}_c - \mathbf{s}_c) \right\}. \quad (4.6)$$

Using the AWGN assumption, Equation (4.6) simplifies to

$$f_{\theta}(\mathbf{x}_c) = (\pi\sigma^2)^{-N} \exp \left\{ -\frac{1}{\sigma^2} (\mathbf{x}_c - \mathbf{s}_c)^H (\mathbf{x}_c - \mathbf{s}_c) \right\}. \quad (4.7)$$

For the Cramer-Rao development, the natural log of (4.7) is helpful,

$$\ln(f_{\theta}(\mathbf{x}_c)) = L_{\theta}(\mathbf{x}_c) = -N \ln(\pi\sigma^2) - \frac{1}{\sigma^2} (\mathbf{x}_c - \mathbf{s}_c)^H (\mathbf{x}_c - \mathbf{s}_c), \quad (4.8)$$

where $L_{\theta}(\mathbf{x}_c)$ is called the log likelihood function (referred to as Likelihood because the value of the unknown parameter vector $\boldsymbol{\theta}$, which characterizes the transmitted signal \mathbf{s}_c , is estimated by determining the value that made the known measurement vector \mathbf{x}_c most likely to occur [10]).

The derivative of (4.8) is

$$s(\boldsymbol{\theta}, \mathbf{x}_c) = \frac{\partial L(\boldsymbol{\theta}, \mathbf{x}_c)}{\partial \boldsymbol{\theta}}, \quad (4.9)$$

where $s(\boldsymbol{\theta}, \mathbf{x}_c)$ is called the score function. The values of $\boldsymbol{\theta}$ where the score function vanishes is the ML estimate of $\boldsymbol{\theta}$ - see Section 2.4.1. The score function covariance is referred to as the Fisher information matrix, $\mathbf{J}(\boldsymbol{\theta})$

$$\mathbf{J}(\boldsymbol{\theta}) = \mathcal{E} \left\{ s(\boldsymbol{\theta}, \mathbf{x}_c) s(\boldsymbol{\theta}, \mathbf{x}_c)^H \right\}. \quad (4.10)$$

A per-element formula for the Fisher information matrix is [11]

$$J(\theta_i, \theta_j) = -\mathcal{E} \left\{ \frac{\partial^2 L(\boldsymbol{\theta}, \mathbf{x}_c)}{\partial \theta_i \partial \theta_j} \right\}. \quad (4.11)$$

The Fisher Information contains information on the maximum rate of change near the peak of the pdf which corresponds to the ML estimate. The inverse of the maximum rate of change yields the minimum variance the unbiased estimate can attain, thus the inverse of the Fisher information matrix contains information on the minimum value the covariance can attain [10]. If the estimate is *unbiased*, the inverse is also the *minimum MSE* a ML estimate can attain [10] - see Section 2.3.

A more specific formula for the per element Fisher information matrix of \mathbf{x}_c is derived below. Inserting (4.8) into (4.11) yields

$$J_x(\theta_i, \theta_j) = -\mathcal{E} \left\{ -\frac{1}{\sigma^2} \left(\frac{\partial^2}{\partial \theta_i \partial \theta_j} (\mathbf{x}_c - \mathbf{s}_c)^H (\mathbf{x}_c - \mathbf{s}_c) \right) \right\}. \quad (4.12)$$

Using the chain rule from Calculus, (4.12) becomes

$$J_x(\theta_i, \theta_j) = \mathcal{E} \left\{ \frac{1}{\sigma^2} \left(\left(\frac{\partial^2 \mathbf{s}_c^H}{\partial \theta_i \partial \theta_j} \right) (\mathbf{x}_c - \mathbf{s}_c) + (\mathbf{x}_c - \mathbf{s}_c)^H \left(\frac{\partial^2 \mathbf{s}_c}{\partial \theta_i \partial \theta_j} \right) + \left(\frac{\partial \mathbf{s}_c^H}{\partial \theta_i} \right) \left(\frac{\partial \mathbf{s}_c}{\partial \theta_j} \right) + \left(\frac{\partial \mathbf{s}_c^H}{\partial \theta_j} \right) \left(\frac{\partial \mathbf{s}_c}{\partial \theta_i} \right) \right) \right\}. \quad (4.13)$$

Taking the expectation of the terms of (4.13) and noting that following expectation value, $\mathcal{E} \{ \mathbf{x}_c - \mathbf{s}_c \} = \mathbf{0}$, the formula for the Fisher information matrix simplifies to

$$J_x(\theta_i, \theta_j) = \frac{1}{\sigma^2} \left(\left(\frac{\partial \mathbf{s}_c^H}{\partial \theta_i} \right) \left(\frac{\partial \mathbf{s}_c}{\partial \theta_j} \right) + \left(\frac{\partial \mathbf{s}_c^H}{\partial \theta_j} \right) \left(\frac{\partial \mathbf{s}_c}{\partial \theta_i} \right) \right). \quad (4.14)$$

Let

$$\frac{\partial \mathbf{s}_c}{\partial \theta_i} = \mathbf{a} + j\mathbf{b} \quad (4.15)$$

where \mathbf{a} is the real part and \mathbf{b} is the imaginary part of the complex vector quantity. Also, let

$$\frac{\partial \mathbf{s}_c}{\partial \theta_j} = \mathbf{c} + j\mathbf{d} \quad (4.16)$$

where \mathbf{c} is the real part and \mathbf{d} is the imaginary part of the vector quantity. Then (4.14) becomes

$$J_x(\theta_i, \theta_j) = \frac{1}{\sigma^2} ((\mathbf{a} + j\mathbf{b})^H (\mathbf{c} + j\mathbf{d}) + (\mathbf{c} + j\mathbf{d})^H (\mathbf{a} + j\mathbf{b})). \quad (4.17)$$

Equation (4.17) simplifies to

$$J_x(\theta_i, \theta_j) = \frac{2}{\sigma^2} (\mathbf{a}^T \mathbf{c} + \mathbf{d}^T \mathbf{b}). \quad (4.18)$$

Inserting the derivatives from (4.15) and (4.16) into (4.18), the desired formula for the Fisher information matrix for complex sinusoids in complex white Gaussian noise is obtained

$$J_x(\theta_i, \theta_j) = \frac{2}{\sigma^2} \text{Re} \left\{ \frac{\partial \mathbf{s}_c^H}{\partial \theta_i} \frac{\partial \mathbf{s}_c}{\partial \theta_j} \right\} = \frac{2}{\sigma^2} \text{Re} \{ \mathbf{S}_j \}, \quad (4.19)$$

where

$$\mathbf{S}_j = \frac{\partial \mathbf{s}_c^H}{\partial \theta_i} \frac{\partial \mathbf{s}_c}{\partial \theta_j}. \quad (4.20)$$

The above formula is used to calculate the Fisher information matrix elements for the following $\boldsymbol{\theta}$ vector parameters:

\mathbf{s}_{c1}	\mathbf{s}_{c2}
$\theta(1) = \omega_1$	$\theta(4) = \omega_2$
$\theta(2) = A_1$	$\theta(5) = A_2$
$\theta(3) = \phi_1$	$\theta(6) = \phi_2$

The hermitian matrix \mathbf{S}_j contains the values

$$\mathbf{S}_j = \begin{bmatrix} A_1^2 \frac{\partial \mathbf{h}_1^H}{\partial \omega_1} \frac{\partial \mathbf{h}_1}{\partial \omega_1} & A_1 \frac{\partial \mathbf{h}_1^H}{\partial \omega_1} \mathbf{h}_1 & A_1^2 \frac{\partial \mathbf{h}_1^H}{\partial \omega_1} \frac{\partial \mathbf{h}_1}{\partial \phi_1} & A_1 A_2 \frac{\partial \mathbf{h}_1^H}{\partial \omega_1} \frac{\partial \mathbf{h}_2}{\partial \omega_2} & A_1 \frac{\partial \mathbf{h}_1^H}{\partial \omega_1} \mathbf{h}_2 & A_1 A_2 \frac{\partial \mathbf{h}_1^H}{\partial \omega_1} \frac{\partial \mathbf{h}_2}{\partial \phi_2} \\ (1,2)^* & \mathbf{h}_1^H \mathbf{h}_1 & A_1 \mathbf{h}_1 \frac{\partial \mathbf{h}_1^H}{\partial \phi_1} & A_2 \mathbf{h}_1 \frac{\partial \mathbf{h}_2^H}{\partial \omega_2} & \mathbf{h}_1^H \mathbf{h}_2 & A_2 \mathbf{h}_1 \frac{\partial \mathbf{h}_2^H}{\partial \phi_2} \\ (1,3)^* & (2,3)^* & A_1^2 \frac{\partial \mathbf{h}_1^H}{\partial \phi_1} \frac{\partial \mathbf{h}_1}{\partial \phi_1} & A_1 A_2 \frac{\partial \mathbf{h}_1^H}{\partial \phi_1} \frac{\partial \mathbf{h}_2}{\partial \omega_2} & A_1 \frac{\partial \mathbf{h}_1^H}{\partial \phi_1} \mathbf{h}_2 & A_2 A_1 \frac{\partial \mathbf{h}_1^H}{\partial \phi_1} \frac{\partial \mathbf{h}_2}{\partial \phi_2} \\ (1,4)^* & (2,4)^* & (3,4)^* & A_2^2 \frac{\partial \mathbf{h}_2^H}{\partial \omega_2} \frac{\partial \mathbf{h}_2}{\partial \omega_2} & A_2 \frac{\partial \mathbf{h}_2^H}{\partial \omega_2} \mathbf{h}_2 & A_2^2 \frac{\partial \mathbf{h}_2^H}{\partial \omega_2} \frac{\partial \mathbf{h}_2}{\partial \phi_2} \\ (1,5)^* & (2,5)^* & (3,5)^* & (4,5)^* & \mathbf{h}_2^H \mathbf{h}_2 & A_2 \mathbf{h}_2 \frac{\partial \mathbf{h}_2^H}{\partial \phi_2} \\ (1,6)^* & (2,6)^* & (3,6)^* & (4,6)^* & (5,6)^* & A_2^2 \frac{\partial \mathbf{h}_2^H}{\partial \phi_2} \frac{\partial \mathbf{h}_2}{\partial \phi_2} \end{bmatrix} \quad (4.21)$$

The structure of \mathbf{S}_j allows the Fisher information matrix (4.19) to be factored as [6]

$$\mathbf{J} = \frac{2}{\sigma^2} \mathbf{C} \mathbf{M} \mathbf{C}, \quad (4.22)$$

where \mathbf{C} is the diagonal matrix of amplitudes

$$\mathbf{C} = \begin{bmatrix} \mathbf{C}_1 & \mathbf{0} \\ \mathbf{0} & \mathbf{C}_2 \end{bmatrix}, \quad \mathbf{C}_i = \begin{bmatrix} A_i & 0 & 0 \\ 0 & 1 & 0 \\ 0 & 0 & A_i \end{bmatrix}. \quad (4.23)$$

The \mathbf{M} matrix from (4.22) incorporates the \mathbf{h} terms of (4.19) and has the following block form

$$\mathbf{M} = \begin{bmatrix} \mathbf{M}_{11} & \mathbf{M}_{12} \\ \mathbf{M}_{21} & \mathbf{M}_{22} \end{bmatrix}. \quad (4.24)$$

\mathbf{M}_{ij} is a 3 by 3 matrix that is derived in the following manner. Note the following

$$\frac{\partial \mathbf{h}(\omega_i, \phi_i)}{\partial \omega_i} = j n \exp\{j(\omega_i n + \phi_i)\} \quad (4.25)$$

$$\frac{\partial \mathbf{h}(\omega_i, \phi_i)}{\partial \phi_i} = j \exp\{j(\omega_i n + \phi_i)\} \quad (4.26)$$

Using (4.25), the elements of \mathbf{M}_{ij} are

$$M_{ij}(1,1) = \text{Re}\left\{ \frac{\partial \mathbf{h}_i^H}{\partial \omega_i} \frac{\partial \mathbf{h}_j}{\partial \omega_j} \right\} = \sum_{n=0}^{N-1} n^2 \cos((\omega_i - \omega_j)n + (\phi_i - \phi_j)) \quad (4.27)$$

$$M_{ij}(1, 2) = Re\left\{\frac{\partial \mathbf{h}_i^H}{\partial \omega_i} \mathbf{h}_j\right\} = \sum_{n=0}^{N-1} -n \sin((\omega_i - \omega_j)n + (\phi_i - \phi_j)) \quad (4.28)$$

$$M_{ij}(1, 3) = Re\left\{\frac{\partial \mathbf{h}_i^H}{\partial \omega_i} \frac{\partial \mathbf{h}_j}{\partial \phi_j}\right\} = \sum_{n=0}^{N-1} n \cos((\omega_i - \omega_j)n + (\phi_i - \phi_j)) \quad (4.29)$$

$$M_{ij}(2, 1) = Re\left\{\mathbf{h}_i^H \frac{\partial \mathbf{h}_j}{\partial \omega_j}\right\} = \sum_{n=0}^{N-1} n \sin((\omega_i - \omega_j)n + (\phi_i - \phi_j)) \quad (4.30)$$

$$M_{ij}(2, 2) = Re\left\{\mathbf{h}_i^H \mathbf{h}_j\right\} = \sum_{n=0}^{N-1} \cos((\omega_i - \omega_j)n + (\phi_i - \phi_j)) \quad (4.31)$$

$$M_{ij}(2, 3) = Re\left\{\mathbf{h}_i^H \frac{\partial \mathbf{h}_j}{\partial \phi_j}\right\} = \sum_{n=0}^{N-1} \sin((\omega_i - \omega_j)n + (\phi_i - \phi_j)) \quad (4.32)$$

$$M_{ij}(3, 1) = Re\left\{\frac{\partial \mathbf{h}_i^H}{\partial \phi_i} \frac{\partial \mathbf{h}_j}{\partial \omega_j}\right\} = \sum_{n=0}^{N-1} n \cos((\omega_i - \omega_j)n + (\phi_i - \phi_j)) \quad (4.33)$$

$$M_{ij}(3, 2) = Re\left\{\frac{\partial \mathbf{h}_i^H}{\partial \phi_i} \mathbf{h}_j\right\} = \sum_{n=0}^{N-1} -\sin((\omega_i - \omega_j)n + (\phi_i - \phi_j)) \quad (4.34)$$

$$M_{ij}(3, 3) = Re\left\{\frac{\partial \mathbf{h}_i^H}{\partial \phi_i} \frac{\partial \mathbf{h}_j}{\partial \phi_j}\right\} = \sum_{n=0}^{N-1} \cos((\omega_i - \omega_j)n + (\phi_i - \phi_j)) \quad (4.35)$$

Let $\Delta_{ij} = (\omega_i - \omega_j)n + (\phi_i - \phi_j)$, then the matrix form of \mathbf{M}_{ij} is

$$\mathbf{M}_{ij} = \begin{bmatrix} \sum_{n=0}^{N-1} n^2 \cos(\Delta_{ij}) & \sum_{n=0}^{N-1} -n \sin(\Delta_{ij}) & \sum_{n=0}^{N-1} n \cos(\Delta_{ij}) \\ \sum_{n=0}^{N-1} n \sin(\Delta_{ij}) & \sum_{n=0}^{N-1} \cos(\Delta_{ij}) & \sum_{n=0}^{N-1} \sin(\Delta_{ij}) \\ \sum_{n=0}^{N-1} n \cos(\Delta_{ij}) & \sum_{n=0}^{N-1} -\sin(\Delta_{ij}) & \sum_{n=0}^{N-1} \cos(\Delta_{ij}) \end{bmatrix}. \quad (4.36)$$

The inverse of the Fisher Information Matrix is the minimum estimation error covariance matrix

$$\mathbf{J}^{-1} = \frac{\sigma^2}{2} \mathbf{C}^{-1} \mathbf{M}^{-1} \mathbf{C}^{-1}. \quad (4.37)$$

Each element of the diagonal of (4.37) is the CRB for the corresponding parameter. It can be shown that a formula for the inverse of the blocked matrix \mathbf{M} is [13]

$$\mathbf{M}^{-1} = \begin{bmatrix} (\mathbf{M}_{11} - \mathbf{M}_{12}\mathbf{M}_{22}^{-1}\mathbf{M}_{21})^{-1} & -(\mathbf{M}_{11} - \mathbf{M}_{12}\mathbf{M}_{22}^{-1}\mathbf{M}_{21})^{-1}\mathbf{M}_{12}\mathbf{M}_{22}^{-1} \\ -(\mathbf{M}_{22} - \mathbf{M}_{21}\mathbf{M}_{11}^{-1}\mathbf{M}_{12})^{-1}\mathbf{M}_{21}\mathbf{M}_{11}^{-1} & (\mathbf{M}_{22} - \mathbf{M}_{21}\mathbf{M}_{11}^{-1}\mathbf{M}_{12})^{-1} \end{bmatrix}. \quad (4.38)$$

Due to the symmetry of \mathbf{M} for the complex sinusoid case, $\mathbf{M}^{-1}(1, 1) = \mathbf{M}^{-1}(4, 4)$ [6].

Thus, the CRB for minimum ω_i estimation variance is

$$\text{var}\{\hat{\omega}_i\} \geq \frac{\sigma^2 D(1, 1)}{2A_i^2} \quad (4.39)$$

where \mathbf{D} is defined as

$$\mathbf{D} = (\mathbf{M}_{11} - \mathbf{M}_{12}\mathbf{M}_{22}^{-1}\mathbf{M}_{21})^{-1}. \quad (4.40)$$

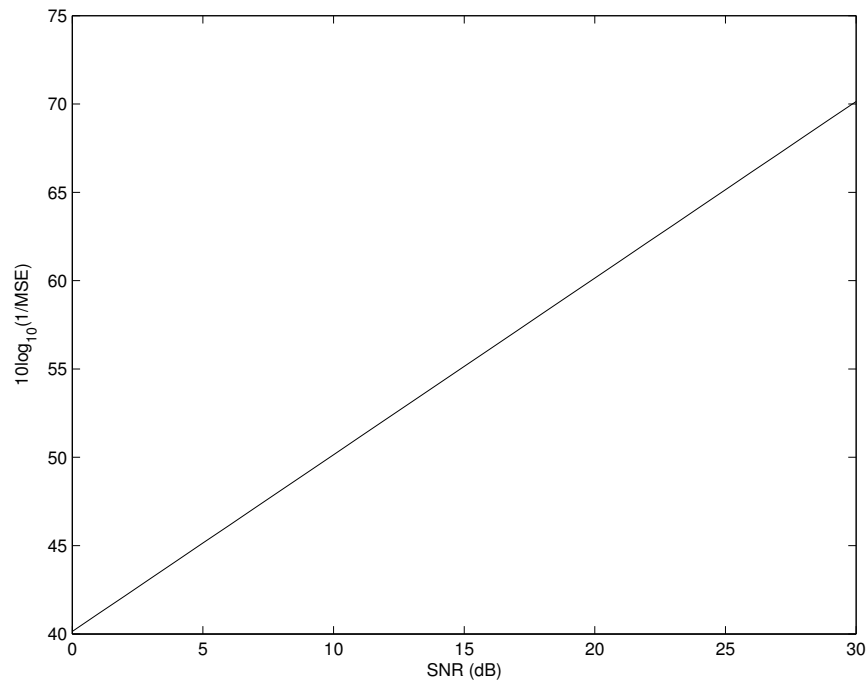
The corresponding CRB for frequency estimation is

$$\text{var}\{\hat{f}_i\} \geq \frac{\sigma^2 D(1, 1)}{2(2\pi)^2 A_i^2}. \quad (4.41)$$

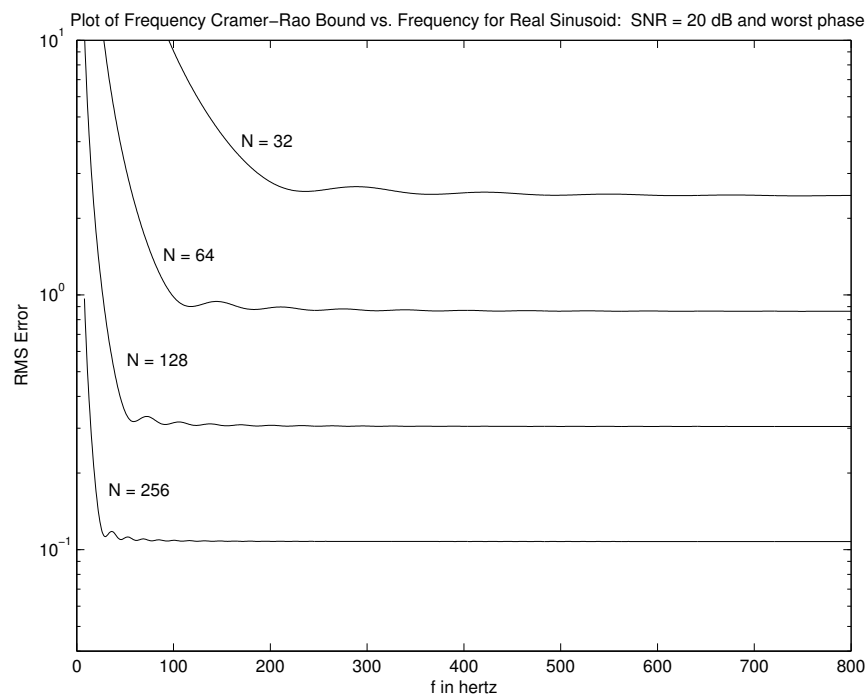
To ensure the computer code generating the multiple sinusoid CRB accuracy, comparisons to the results in [13] and [6] are contained in Figure 4.1. Figure 4.1(a) contains the CRB versus SNR for two complex sinusoids in complex noise with the following parameters: $N=25$, $[A_1 = 1, f_1 = 0.5, \phi_1 = 0]$, $[A_2 = 1, f_2 = 0.52, \phi_2 = \frac{\pi}{4}]$; $SNR = -10 \log_{10}(\sigma^2)$. The results match those in [13]. Figure 4.1(a) contains the CRB versus frequency for one real sinusoid with worst phase difference between negative and positive frequency images (which consists of two complex sinusoids) in real noise with the following parameters: $[A_1 = 1, \phi_1 = 0, \phi_{1i} = N\pi f_2 - \pi - N\pi f_1]$; $SNR = -10 \log_{10}(2\sigma^2) = 20$. Results match [6]. Thus, the code generating the multiple sinusoid CRB is validated.

4.2.2 Real Signal CRB. For real signals in real white noise, the development from above is modified. The signal is now

$$s(n) = \sum_{i=1}^p A_i \cos(\omega_i n + \phi_i) = \sum_{i=1}^p A_i \mathbf{g}(\omega_i, \phi_i). \quad n = 0 \dots N-1 \quad (4.42)$$



(a) Kay Comparison



(b) Rife Comparison

Figure 4.1: Equi-amplitude CRB validation.

Equation (4.22) becomes [6]

$$\mathbf{J} = \frac{1}{\sigma^2} \mathbf{C} \mathbf{Q} \mathbf{C}, \quad (4.43)$$

where \mathbf{Q} has the same block structure as (4.24). Each block matrix of elements of \mathbf{Q} is defined as [6]

$$\mathbf{Q}_{ij} = \frac{1}{2} [\mathbf{M}_{ij}(\omega_i - \omega_j, \phi_i - \phi_j) - \mathbf{M}_{ij}(\omega_i + \omega_j, \phi_i + \phi_j) \mathbf{B}_J], \quad (4.44)$$

where \mathbf{M}_{ij} was defined in (4.36), and \mathbf{B}_J is a 3 by 3 diagonal matrix defined as

$$\mathbf{B}_J = \text{diag}(1, -1, 1). \quad (4.45)$$

Because the tones are real instead of complex, $J^{-1}(4, 4)$ is not in general equal to $J^{-1}(1, 1)$ (usually only a slight difference). Thus, a formula for each frequency is used for the bound on the corresponding frequency estimate of real signals. The Cramer-Rao bound for the first frequency estimate is

$$\text{var}\{\hat{f}_1\} \geq \frac{\sigma^2 E(1, 1)}{(2\pi)^2 A_1^2} \quad (4.46)$$

where \mathbf{E} is defined by substituting \mathbf{Q}_{ij} for \mathbf{M}_{ij} in (4.40). The Cramer-Rao bound for the second frequency estimate is

$$\text{var}\{\hat{f}_2\} \geq \frac{\sigma^2 F(1, 1)}{(2\pi)^2 A_2^2} \quad (4.47)$$

where the matrix \mathbf{F} is defined as

$$\mathbf{F} = (\mathbf{Q}_{22} - \mathbf{Q}_{21} \mathbf{Q}_{11}^{-1} \mathbf{Q}_{12})^{-1}. \quad (4.48)$$

4.3 Cramer-Rao Bound for Instantaneous Dynamic Range

In [5], the IDR-CRB for complex signals is derived. The method of [5] uses an iterative method in terms of delta values for the calculation of the IDR-CRB, which is computationally intensive and difficult to implement. Because the Fisher information matrix can be factored as shown in (4.22), a simpler and more reliable method is introduced here to calculate the complex signal IDR-CRB and then extended to the real signal IDR-CRB.

Recall the definition of IDR employed in this thesis

- The thesis IDR definition – IDR is defined as the maximum signal difference for a given frequency estimation accuracy, a given frequency separation and a given SNR [5].

From this definition, the CRB for instantaneous dynamic range for two complex exponentials is derived by modifying the multiple sinusoid CRB using the following method.

1. Specify the noise power, σ^2 , and the desired SNR (in terms of A_1), RMS frequency estimation accuracy¹, and frequency separation Δf .
2. The A_1 amplitude is

$$A_1 = \sqrt{\sigma^2 10^{(SNR/10)}}. \quad (4.49)$$

3. Use the following modified form of (4.41) to solve for the bound amplitude of A_2

$$A_{2b} \geq \sqrt{\frac{\sigma^2 D(1, 1)}{2(2\pi)^2 f_{acc}^2}} \quad (4.50)$$

where f_{acc} is the desired RMS frequency estimation accuracy and A_{2b} is the bound amplitude. *If A_{2b} is greater than A_1 , then the desired frequency accuracy is not achievable for the given parameters.*

4. If achievable, the Cramer Rao bound for the instantaneous dynamic range is then defined as

$$\text{IDR(dB)} \leq 20 \log_{10} \left(\frac{A_1}{A_{2b}} \right). \quad (4.51)$$

Figure 4.2 is a plot of the complex signal IDR-CRB vs. frequency difference for the parameters: $[A_1 = 1, f_1 = 0.2, \phi_1 = 0]$, $[\phi_2 = N\pi f_2 - \pi - N\pi f_1]$; $f_{acc} = \frac{1}{10N}$; $SNR = -10 \log_{10}(\sigma^2) = 20, N = 100$. The phase value ϕ_2 used to generate Fig. 4.2

$$\phi_2 = N\pi f_2 - \pi - N\pi f_1, \quad (4.52)$$

¹Recall from Chapter 2.3 that the RMS squared is the MSE, which is equal to the estimate variance for an unbiased estimator.

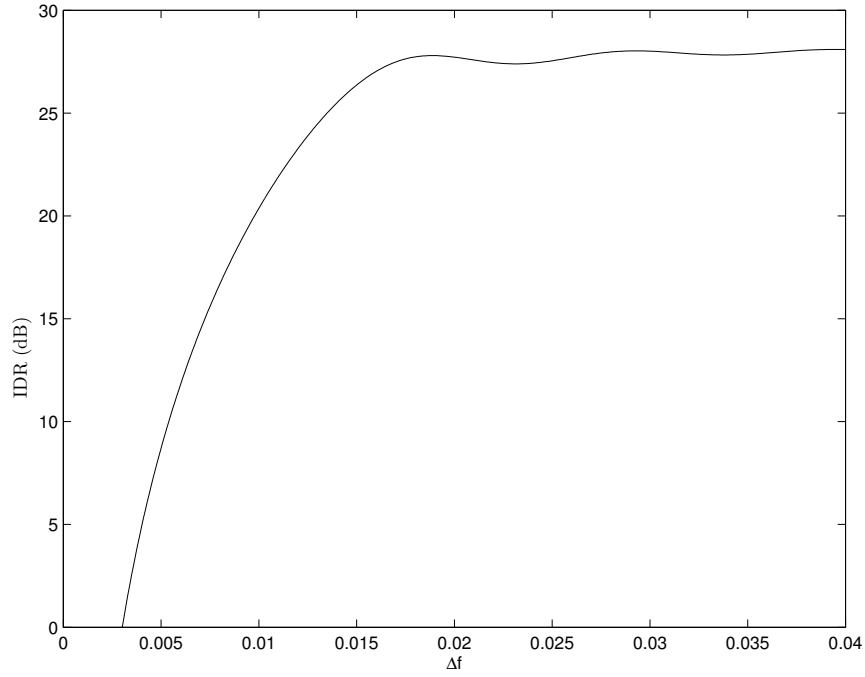


Figure 4.2: Complex IDR-CRB versus Δf .

is the worst phase difference for frequency estimation [5]. The point where the plot flattens out where the phase difference and frequency difference interaction terms \mathbf{M} become negligible and the single signal required amplitude is attained for the desired estimation accuracy.

The method of calculating the real signal IDR-CRB is similar to the method for complex signals, with the following exceptions:

- The A_1 is now calculated as

$$A_1 = \sqrt{2\sigma^2 10^{(SNR/10)}}. \quad (4.53)$$

- The following equation must be used in place of (4.50) to calculate the bound amplitude

$$A_{2b} \geq \sqrt{\frac{\sigma^2 E(1, 1)}{(2\pi)^2 f_{acc}^2}} \quad (4.54)$$

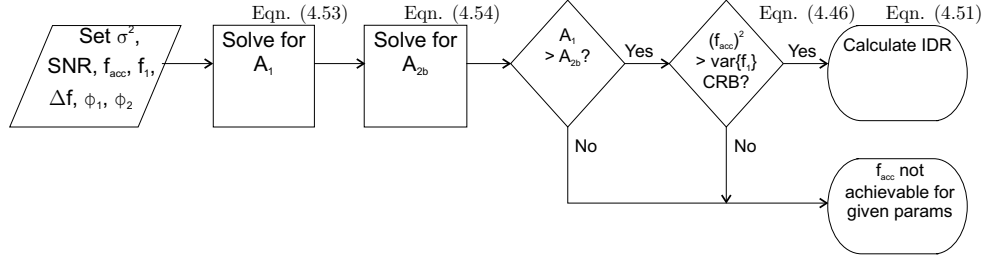


Figure 4.3: Real Signal IDR-CRB Algorithm Flowchart.

A slight error term is introduced using the above equation when the amplitude is near the instantaneous dynamic range resolvable threshold because of the slight difference in the values of $J^{-1}(1, 1)$ and $J^{-1}(4, 4)$ for real tones. The algorithm is modified without iterating to handle this slight difference in the following way.

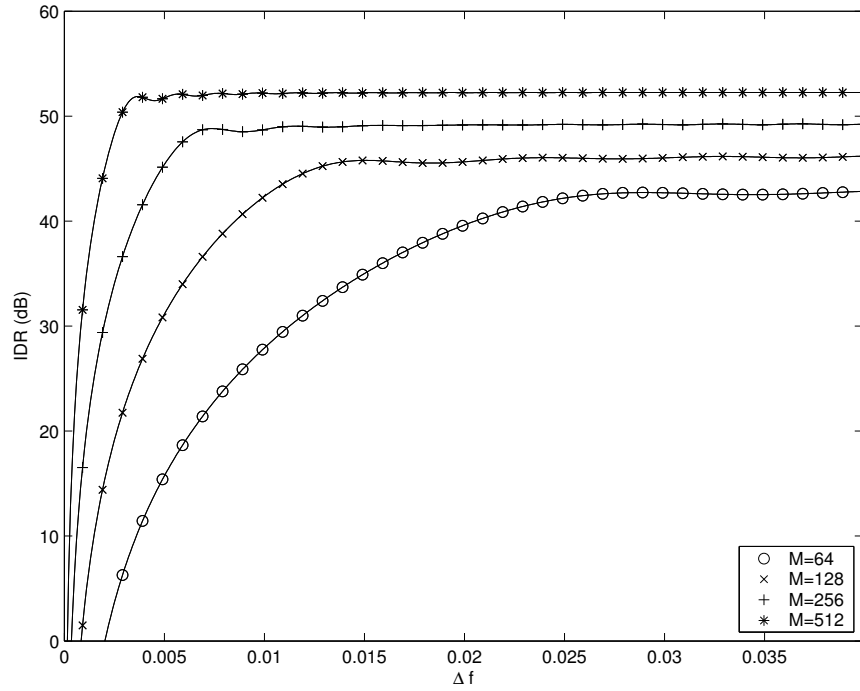
- Compare the estimation accuracy of (4.46) to the desired estimation accuracy if the value of A_{2b} is close to the value of A_1 . If the estimation accuracy is higher, the threshold has not been met even though A_2 amplitude is less than one, and the desired estimation accuracy is not achievable.
- *The IDR-CRB values for real signals are frequency dependent, especially at frequencies near zero (i.e. if $f_1 = 0.001$).*

Figure 4.3 is a flow chart representation of the method to generate the IDR-CRB.

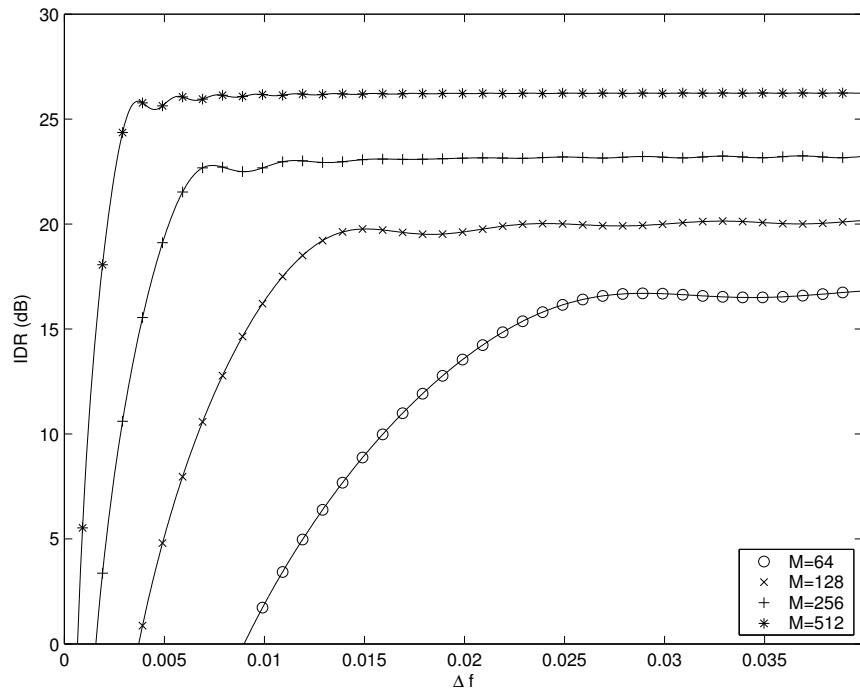


Throughout the rest of the thesis, IDR-CRB denotes the real signal IDR-CRB unless otherwise stated.

Figure 4.4 is a plot of the real signal IDR-CRB for different values of N generated using the method of Figure 4.3. In the plots, the IDR-CRB is calculated at $\Delta f = 0.001$ intervals for specified N samples of two sinusoids in noise with worst phase difference with parameters: $[A_1 = 1, f_1 = 0.2, \phi_1 = 0], [\phi_2 = N\pi f_2 - \pi - N\pi f_1]; SNR = -10 \log_{10}(2\sigma^2) = 20$ dB. For comparison purposes, the frequency estimation accuracy is also scaled as a function of N , where N is the number of measurement points. As expected, the bound for the higher N exhibits a sharper rise time than the lower N . In the Chapter V, an IGLS algorithm-based parametric receiver IDR-CRB comparison validates the IDR-CRB results.



(a) $f_{acc} = \frac{1}{N}$



(b) $f_{acc} = \frac{1}{20N}$

Figure 4.4: Real Signal IDR-CRB ($N = 64, 128, 256, 512$) versus Δf .

4.4 *Conclusion*

A Cramer-Rao bound is developed for an unbiased estimator's IDR by modifying Rife's result in [6] for both real and complex sinusoidal signals in AWGN. To achieve the IDR-CRB, the estimator must be an unbiased ML estimator of frequency; i.e. the estimator must be unbiased and efficient [11]. The next chapter compares an IGLS-algorithm based parametric receiver to the IDR-CRB derived in this chapter.

V. IGLS Algorithm-Based Parametric Receiver

5.1 Introduction

When the number of signals is known, the EW receiver frequency estimates are improved dramatically by basing the receiver on a parametric frequency estimation algorithm, i.e. a parametric EW receiver¹. The parametric algorithms achieve these improved estimates because prior knowledge of the signal form is exploited. To bound IDR performance and compare to the IDR-CRB derived in Chapter IV, a parametric frequency estimation algorithm that achieves ML results is desired. Thus, a frequency estimation algorithm based on Linear Prediction (LP) called Iterative Generalized Least Squares is introduced for application in the parametric receiver and shown to yield Maximum Likelihood frequency estimates in Section 5.2. The IGLS algorithm is compared to the IDR-CRB in Section 5.3. Finally, in Section 5.3.1, experimental results from the IDR-CRB comparison result in defining IDR differently for a Parametric based receiver when the frequency estimate requirements are loose.

5.2 IGLS Development

In this section, the IGLS algorithm, related to the IQML algorithm discussed in [14], is fully developed and shown to yield ML frequency estimates. This is the author's development of the IGLS algorithm originally derived by Dr. Pachter and researched by Ingham in [8] and Zahirniak in [7]. Section 5.2.1 provides the necessary background on LP theory including Prony's method and the Extended Prony Method. Section 5.2.2 derives the IGLS algorithm. In Section 5.2.3, frequency estimate confidence intervals are developed. Simulations then verify IGLS ML performance in Section 5.2.4.

5.2.1 Linear Prediction Theory. Consider the real sinusoidal signal

$$s(n) = \sum_{i=1}^p A_i \cos(\omega_i n + \phi_i). \quad (5.1)$$

¹Determining the number of signals for a parametric receiver is an area of research in its own right and is not discussed here. See Reference [13] for more details.

The signal's samples satisfy the difference equation [21,22]

$$s(n) = \sum_{m=1}^{2p} a(m)s(n-m), \quad (5.2)$$

where the coefficients of the $2p$ length vector \mathbf{a} are called the LP coefficients. The proof for this relationship is quite involved, but very informative (this proof follows [21] closely with an example at the end to clarify).

Consider now the following factored polynomial, $\Phi(z)$, with the real signal frequencies of (5.2) as roots (for a complex signal remove the negative exponential),

$$\Phi(z) = \prod_{i=1}^p (z - e^{j\omega_i})(z - e^{-j\omega_i}). \quad (5.3)$$

Expanding the above equation yields the following polynomial

$$\Phi(z) = \sum_{m=0}^{2p} a(m)z^{2p-m}. \quad (5.4)$$

where $a(0)$ is constrained to be 1. Form a linear difference equation by multiplying $a(m)$ by $s(n-m)$ and summing over m to yield

$$\sum_{m=0}^{2p} a(m)s(n-m) = \sum_{m=0}^{2p} a(m) \sum_{i=1}^{2p} \frac{A_i}{2} (e^{j\omega_i(n-m)} e^{j\phi_i} + e^{-j\omega_i(n-m)} e^{-j\phi_i}). \quad (5.5)$$

Switching the order of summations and making the following substitution $n-m = n-2p+2p-m$ (realizing that $n \geq 2p$), yields

$$\begin{aligned} \sum_{m=0}^{2p} a(m)s(n-m) &= \sum_{i=1}^{2p} \frac{A_i}{2} e^{j\omega_i(n-2p)} e^{j\phi_i} \sum_{m=0}^{2p} a(m) e^{j\omega_i(2p-m)} \\ &\quad + \sum_{i=1}^{2p} \frac{A_i}{2} e^{-j\omega_i(n-2p)} e^{-j\phi_i} \sum_{m=0}^{2p} a(m) e^{-j\omega_i(2p-m)} \end{aligned} \quad (5.6)$$

Note that (This is beautiful!!)

$$\sum_{m=0}^{2p} a(m)(e^{j\omega_i(2p-m)}) = 0 \quad (5.7)$$

$$\sum_{m=0}^{2p} a(m)e^{-j\omega_i(2p-m)} = 0. \quad (5.8)$$

because the exponentials are roots of the polynomial from (5.4) as shown in (5.3). Thus, the LP equation

$$s(n) = - \sum_{m=1}^{2p} a(m)s(n-m), \quad (5.9)$$

is arrived at (recall $a(0)$ is constrained to be one). In matrix format, the exactly determined system to solve for the polynomial values is

$$\begin{bmatrix} s(2p-1) & s(2p-2) & \dots & s(0) \\ s(2p) & s(2p-1) & \dots & s(1) \\ \vdots & \vdots & \ddots & \vdots \\ s(4p-2) & s(4p-3) & \dots & s(2p-1) \end{bmatrix} \begin{bmatrix} a(1) \\ a(2) \\ \vdots \\ a(2p) \end{bmatrix} = - \begin{bmatrix} s(2p) \\ s(2p+1) \\ \vdots \\ s(4p-1) \end{bmatrix} \quad (5.10)$$

where the matrix of signal values is $2p$ by $2p$. After solving for the $2p$ LP coefficients, the frequencies are obtained by rooting the polynomial (5.4) formed by the LP coefficients. Note that the nonlinearity of estimating the frequencies has been compressed into the rooting of the polynomial comprised of the LP coefficients \mathbf{a} [21]. The above math can be interpreted in the following way: Equation (5.9) is a linear difference equation with associated characteristic equation (5.4) that has the homogeneous solution given by (5.3) [21]. The above LP-based method of determining frequencies via rooting the LP coefficient characteristic polynomial is called Prony's Method [21]².

Formulas for the relationships between the LP coefficients \mathbf{a} and the frequencies \mathbf{f} are derived below for the case of two real sinusoids. For two real sinusoids, Equation (5.3)

²Originally developed by Gaspard Riche, Baron de Prony in 1795 in his study of the expansion of various gases [21].

Table 5.1: LP Coefficients to Frequency Relationship.

<i>LP Coeff</i>	<i>Formula</i>
a(0)	1
a(1)	$-2 \cos(\omega_1) - 2 \cos(\omega_2)$
a(2)	$2 + 4 \cos(\omega_1) \cos(\omega_2)$
a(3)	$-2 \cos(\omega_1) - 2 \cos(\omega_2)$
a(4)	1

becomes

$$\Phi(z) = (z - e^{j\omega_1})(z - e^{-j\omega_1})(z - e^{j\omega_2})(z - e^{-j\omega_2}). \quad (5.11)$$

Combining the two like frequency terms yields

$$\Phi(z) = (z^2 - 2 \cos(\omega_1)z + 1)(z^2 - 2 \cos(\omega_2)z + 1). \quad (5.12)$$

Multiplying out (5.12) yields the polynomial

$$\Phi(z) = z^4 - (2 \cos(\omega_1) + 2 \cos(\omega_2))z^3 + (2 + 4 \cos(\omega_1) \cos(\omega_2))z^2 - (2 \cos(\omega_1) + 2 \cos(\omega_2))z + 1. \quad (5.13)$$

Table 5.1 relates the coefficients of the polynomial to the frequencies. Note that the Table 5.1 polynomial terms are symmetric; it can be shown in general that the polynomial terms for real sinusoids are symmetric [22].

For two sinusoids a closed form solution for the cosines in Table 5.1 in terms of a(1) and a(2) using the formulas of Table 5.1 can be obtained. Solving the formula for a(2) in terms of $\cos(\omega_2)$ yields

$$\cos(\omega_2) = \frac{a(2) - 2}{4 \cos(\omega_1)}. \quad (5.14)$$

Insert the value for $\cos(\omega_2)$ into the formula for a(1) to obtain

$$-a(1) = 2 \cos(\omega_1) + \frac{a(2) - 2}{2 \cos(\omega_1)} \quad (5.15)$$

$$0 = \cos^2(\omega_1) + \frac{a(1)}{2} \cos(\omega_1) + \frac{a(2) - 2}{4} \quad (5.16)$$

The above is a quadratic equation with roots at $\cos(\omega_1)$ and at $\cos(\omega_2)$ (switch around (5.14) to see the second root). Thus, a quadratic must be solved, and the following relationship is arrived at

$$\cos(\omega_1), \cos(\omega_2) = \frac{-a(1) \pm \sqrt{a(1)^2 - 4a(2) + 8}}{4}. \quad (5.17)$$

When noise is not present, the LP coefficients are estimated perfectly from the data by solving (5.10) for the vector \mathbf{a} , and thereby the frequencies can be calculated error-free from (5.17) regardless of frequency spacing, i.e. no Fourier Resolution limit. Conceptually, the difference between the Periodogram method and Prony's method is that the Periodogram evaluates certain frequencies, while Prony's method estimates the frequencies exactly from the data [21].

When measurement noise is added to the system, error is introduced into the above linear prediction relationship and Prony's method performs poorly. Therefore, the above equations are modified to handle the presence of noise.

5.2.1.1 Extended Prony Method. The measured signal with noise is

$$x(n) = s(n) + w(n), \quad n = 0, \dots, N-1 \quad (5.18)$$

where $s(n)$ is defined in (5.1) and $w(n)$ is AWGN. Normally, more samples are present than required for the exact solution of the LP coefficients using Prony's Method. In the presence of noise, these additional samples can be exploited to obtain a least squares solution that washes out the error introduced by the measurement noise. For the following development, reshape the measurement vector \mathbf{x} of (5.18) into a $M-2p$ by $2p+1$ observation matrix \mathbf{X}

$$\mathbf{X} = \begin{bmatrix} x(M-1) & x(M-2) & \dots & x(M-2p) \\ x(M-2) & x(M-3) & \dots & x(M-2p-1) \\ \vdots & \vdots & \ddots & \vdots \\ x(2p) & x(2p-1) & \dots & x(0) \end{bmatrix}. \quad (5.19)$$

The following $2p + 1$ by $p + 1$ constraint matrix \mathbf{B} is introduced to exploit the real signal LP coefficients' symmetry and reduce the parameter vector size

$$\mathbf{B} = \begin{bmatrix} \mathbf{I}_p & \mathbf{0}_p \\ \mathbf{0}_p^T & 1 \\ \mathbf{IB}_p & \mathbf{0}_p \end{bmatrix}, \quad (5.20)$$

where \mathbf{IB}_p is the p by p 'backwards' identity matrix defined by $\mathbf{IB}_p = \delta(P + 1 - i - j)$, \mathbf{I}_p is a p by p identity matrix, and $\mathbf{0}_p$ is a p by 1 vector of zeroes. Using \mathbf{B} , the linear prediction vector $\mathbf{a} = [a(0) \dots a(2p)]^T$ can be formed in the following way

$$\mathbf{a} = \mathbf{B}\boldsymbol{\alpha}. \quad (5.21)$$

where the reduced parameter vector $\boldsymbol{\alpha}$ is defined as $\boldsymbol{\alpha} = [1 \ a(1) \dots a(p)]^T$. The observation matrix \mathbf{X} is multiplied by the constraint matrix \mathbf{B} yielding

$$\mathbf{X}_c = \mathbf{XB} = [\mathbf{x}_o | \mathbf{X}_o], \quad (5.22)$$

where the matrix \mathbf{X}_c is the constrained data matrix, \mathbf{x}_o contains the first column of \mathbf{X}_c , and \mathbf{X}_o contains the remaining columns of \mathbf{X}_c . Using (5.22), the linear prediction model is

$$\mathbf{e}_o = \mathbf{x}_o + \mathbf{X}_o \mathbf{a}_o. \quad (5.23)$$

where the vector \mathbf{a}_o is the vector of LP coefficients, $\mathbf{a}_o = [a(1) \dots a(p)]^T$, and the vector \mathbf{e}_o is the prediction error vector due to the noise.

The error power, $\|\mathbf{e}_o\|_2^2$, is equal to

$$\|\mathbf{e}_o\|_2^2 = (\mathbf{x}_o + \mathbf{X}_o \mathbf{a}_o)^T (\mathbf{x}_o + \mathbf{X}_o \mathbf{a}_o). \quad (5.24)$$

A good estimate of the unknown LP coefficients are the LP coefficients that minimize the expression in (5.24), i.e. the Least Squares (LS) estimate

$$\hat{\mathbf{a}}_o = -(\mathbf{X}_o^T \mathbf{X}_o)^{-1} \mathbf{X}_o^T \mathbf{x}_o. \quad (5.25)$$

Equation (5.25) is referred to as the Extended Prony Method (EPM) [21]. Although an improvement over the exactly determined method -e.g. (5.10)-, the EPM does not provide efficient LP estimates, and performs poorly in low SNR [21] as shown in the simulations in Section 5.2.4.

5.2.2 Iterative Generalized Least Squares. To improve upon (5.25), it is first necessary to understand why efficiency is not achieved. To this end, the M by $M - 2p$ Toeplitz matrix \mathbf{A}^T defined by the LP coefficients is introduced

$$\mathbf{A}^T = \text{Toeplitz}(1, a(1) \dots a(2p), 0 \dots 0). \quad (5.26)$$

Using (5.26), an equivalent representation of the LP equation error \mathbf{e}_o of (5.23) is

$$\begin{aligned} \mathbf{e}_o &= \mathbf{A}^T \mathbf{x} \\ &= \mathbf{A}^T \mathbf{s} + \mathbf{A}^T \mathbf{n} \\ &= \mathbf{A}^T \mathbf{n}. \end{aligned} \quad (5.27)$$

Thus, the noise vector \mathbf{n} of the measurement vector \mathbf{x} is subjected to a moving average process that yields \mathbf{e}_o . The vector \mathbf{e}_o is a colored, normally distributed, zero mean random vector with covariance matrix

$$\mathbf{C}_{e_o} = \mathbf{A}^T \mathbf{C}_n \mathbf{A}, \quad (5.28)$$

where \mathbf{C}_{e_o} is the error vector covariance, \mathbf{e}_o , and $\mathbf{C}_n = \sigma^2 \mathbf{I}$ is the noise vector covariance. The EPM least squares estimate in (5.25) weights each term's contribution equally. However, since a moving average process has been applied to the noise, coloring the error covariance matrix, this assumption is invalid [7]; unfortunately, this is often overlooked in system identification work [23, 24].

To account for the colored noise, the extended Prony method is modified in the following way. Perform a Cholesky decomposition of the positive semi-definite error covariance matrix inverse to obtain

$$\mathbf{C}_{e_o}^{-1} = \mathbf{G} \mathbf{G}^T, \quad (5.29)$$

where \mathbf{G} is the Cholesky decomposition of $\mathbf{C}_{e_o}^{-1}$, $\mathbf{G} = \mathbf{C}_{e_o}^{-\frac{1}{2}}$. Equation (5.27) is multiplied by \mathbf{G} to yield

$$\mathbf{e}_1 = \mathbf{G}\mathbf{A}^T\mathbf{n}, \quad (5.30)$$

where the vector \mathbf{e}_1 is a normally distributed, zero mean, random vector with covariance matrix

$$\begin{aligned} \mathbf{C}_{e_1} &= \mathcal{E} \{ \mathbf{G}\mathbf{A}^T\mathbf{n}\mathbf{n}^T\mathbf{A}\mathbf{G}^T \} \\ &= \mathbf{G}\mathbf{C}_{e_o}\mathbf{G}^T \\ &= \mathbf{I}. \end{aligned} \quad (5.31)$$

Thus the matrix \mathbf{G} has the desired effect of whitening, a.k.a. decorrelating, the error vector \mathbf{e}_1 .

Returning to the LP representation of (5.23), multiply (5.23) by the matrix \mathbf{G} to yield

$$\mathbf{e}_1 = \mathbf{G}\mathbf{x}_o + \mathbf{G}\mathbf{X}_o\mathbf{a}_o. \quad (5.32)$$

The error power of (5.32), $\|\mathbf{e}_1\|_2^2$, is equal to

$$\|\mathbf{e}_1\|_2^2 = (\mathbf{G}\mathbf{x}_o + \mathbf{G}\mathbf{X}_o\mathbf{a}_o)^T(\mathbf{G}\mathbf{x}_o + \mathbf{G}\mathbf{X}_o\mathbf{a}_o). \quad (5.33)$$

It can be shown that minimizing the expression in (5.33) is equivalent to minimizing (5.24). If \mathbf{G} is assumed not to be a function of \mathbf{a}_o , the weighted least squares solution to minimize (5.33) is

$$\hat{\mathbf{a}}_o = -(\mathbf{X}_o^T(\mathbf{G}^T\mathbf{G})\mathbf{X}_o)^{-1}\mathbf{X}_o^T(\mathbf{G}^T\mathbf{G})\mathbf{x}_o. \quad (5.34)$$

Inserting the value of $\mathbf{G}^T\mathbf{G}$ and $\mathbf{C}_n = \sigma^2\mathbf{I}$ from (5.29) into the above equation yields

$$\hat{\mathbf{a}}_o = -(\mathbf{X}_o^T(\mathbf{A}^T\mathbf{A})^{-1}\mathbf{X}_o)^{-1}\mathbf{X}_o^T(\mathbf{A}^T\mathbf{A})^{-1}\mathbf{x}_o. \quad (5.35)$$

Equation (5.35) correctly accounts for the coloring of the equation error by the moving average process.

\mathbf{G} is a function of \mathbf{a}_o . However, it can be shown that sufficiently close to \mathbf{a}_o (5.35) is a contraction mapping. Thus, when (5.35) is iterated, it will converge to a fixed point that is, in view of (5.34) and (5.35), close to the minimum of the error given by (5.33) (and thereby (5.24)) - see [7, 23–26]. Thus, the following iterative weighted least squares estimate of the LP coefficients is formed from (5.35)

$$\hat{\mathbf{a}}_o^{k+1} = -(\mathbf{X}_o^T (\mathbf{A}_k^T \mathbf{A}_k)^{-1} \mathbf{X}_o)^{-1} \mathbf{X}_o^T (\mathbf{A}_k^T \mathbf{A}_k)^{-1} \mathbf{x}_o, \quad (5.36)$$

where \mathbf{A}_k is constructed using the k th iterate of the LP coefficients $\hat{\mathbf{a}}_o^{(k)}$, and $\hat{\mathbf{a}}_o^{(k+1)}$ of the left hand side of (5.36) is the $k + 1$ iterate of the LP coefficients. Equation (5.32) is minimized when $\hat{\mathbf{a}}_o^{(k+1)} = \hat{\mathbf{a}}_o^{(k)}$. The above efficient algorithm is referred to as Iterative Generalized Least Squares (IGLS). A good initial guess for the values of $\mathbf{a}^{(0)}$ is needed to ensure convergence to the global minimum, especially in low SNR. Initializing via a low-resolution Periodogram or the EPM solution is normally sufficient. Note that initializing via the EPM can be accomplished by setting $\mathbf{A}^T \mathbf{A} = \mathbf{I}$ for the first iteration of (5.36). Simulation experiments have established 10 iteration steps will suffice.

In [7], it is shown that minimizing the objective function via (5.36) is equivalent to obtaining the ML estimate of the LP coefficients, since both same objective function is minimized. By the invariance property of ML estimation, since there is a one to one mapping from the LP coefficients to the frequencies, it is also a ML estimate of the frequencies [11]. Although derived under different assumptions, note there are many similarities between the IGLS algorithm and the Iterative Quadratic Maximum Likelihood (IQML) algorithm, as would be expected, since both yield ML estimates of the LP coefficients. IQML was itself shown to be equivalent to the Iterative Pre-filtering algorithm of Steiglitz and McBride [27]. For brevity's sake, those similarities are not discussed here. The interested reader should refer to [14] for the most comprehensive discussion of IQML and [8] for a comparison of IQML and IGLS. The author notes that the IGLS algorithm has been successfully applied to diverse applications [23, 24, 28].

5.2.3 Confidence Intervals for IGLS Estimates. It is important to predict the accuracy of the frequencies' estimates for EW receivers, especially when frequency can

discriminate different threat types as in Fig. 1.3. To this end, confidence intervals must be established. Normally, confidence intervals are specified in terms of probabilities of error contained within k standard deviations

$$P(-k\sigma < \epsilon < k\sigma) = 1 - \rho, \quad (5.37)$$

where σ is the estimate's standard deviation and $1-\rho$ is the probability the error is contained in the confidence interval. Data driven confidence intervals for IGLS estimates are developed below.

To establish confidence intervals for the LP coefficients, the LP coefficients' variance must be determined. This covariance can be determined using ML theory if the SNR is above threshold³. Note that the whitened Linear Prediction equation error is

$$\mathbf{e}_1 - \mathbf{G}\mathbf{s}_o = \mathbf{G}\mathbf{S}_o\mathbf{a}_o + \mathbf{G}\mathbf{A}^T\mathbf{n}, \quad (5.38)$$

where \mathbf{S}_o and \mathbf{s}_o are the signal components of \mathbf{X}_o and \mathbf{x}_o respectively. Let $\mathbf{q} = \mathbf{e}_1 - \mathbf{G}\mathbf{s}_o$. Since (5.38) is a linear transformation of a Gaussian random variable, \mathbf{q} is also a Gaussian random variable

$$\mathbf{q} = N(\mathbf{G}\mathbf{S}_o\mathbf{a}_o, \mathbf{I}). \quad (5.39)$$

Taking the log of the pdf of \mathbf{q} (5.39) and then the gradient with respect to \mathbf{a}_o yields

$$\frac{\partial \ln f_{\mathbf{q}}}{\partial \mathbf{a}_o} = \mathbf{S}_o^T \mathbf{G}^T \mathbf{q} - \mathbf{S}_o^T \mathbf{G}^T \mathbf{G} \mathbf{S}_o \mathbf{a}_o. \quad (5.40)$$

Setting the right hand side of (5.40) equal to zero and solving for $\hat{\mathbf{a}}_o$ yields the Maximum Likelihood estimate for the LP coefficients

$$\hat{\mathbf{a}}_{o \text{ ML}} = (\mathbf{S}_o^T \mathbf{G}^T \mathbf{G} \mathbf{S}_o)^{-1} \mathbf{S}_o^T \mathbf{G}^T \mathbf{q}. \quad (5.41)$$

The covariance of the LP coefficients' ML estimation error (Note that this estimator is unbiased) can be obtained by backtracking to Equation (5.40) and factoring its right hand

³The threshold effect is discussed in Section 5.2.4.

side

$$\frac{\partial \ln f_{\mathbf{q}}}{\partial \mathbf{a}_o} = (\mathbf{S}_o^T \mathbf{G}^T \mathbf{G} \mathbf{S}_o) ((\mathbf{S}_o^T \mathbf{G}^T \mathbf{G} \mathbf{S}_o)^{-1} \mathbf{S}_o^T \mathbf{G}^T \mathbf{q} - \mathbf{a}_o). \quad (5.42)$$

Note the form of (5.40) matches the form of the Cramer-Rao Lower bound theorem given by [10]; an estimator only achieves efficiency if the partial derivative with respect to the parameter to be estimated can be written in the following form

$$\frac{\partial \ln f_{\mathbf{x}}(\mathbf{x})}{\partial \boldsymbol{\theta}} = \mathbf{J}(\boldsymbol{\theta})(\mathbf{g}(\mathbf{x}) - \boldsymbol{\theta}), \quad (5.43)$$

where \mathbf{x} is an arbitrary vector of interest, $\mathbf{J}(\boldsymbol{\theta})$ is the Fisher information matrix, and $\mathbf{g}(\mathbf{x})$ is the ML estimator. Thus, the Fisher information matrix of the LP coefficient ML estimate of (5.41) is $(\mathbf{S}_o^T \mathbf{G}^T \mathbf{G} \mathbf{S}_o)$, and therefore the covariance of the estimation error, provided ML estimation of the LP coefficients, is

$$\mathbf{C}_{\hat{\mathbf{a}}_o} = (\mathbf{S}_o^T \mathbf{G}^T \mathbf{G} \mathbf{S}_o)^{-1}. \quad (5.44)$$

Unfortunately, (5.44) features \mathbf{S}_o which is not available. If the observation matrix is substituted for the signal matrix, the covariance has randomness associated with it because of the noise. However, if the SNR is high enough and assuming the LP coefficients are sufficiently close to the true value, the noise can be neglected, and an estimate of the LP coefficient estimation error covariance matrix is [7]

$$\begin{aligned} \hat{\mathbf{C}}_{\hat{\mathbf{a}}_o} &= (\mathbf{X}_o^T \mathbf{G}^T \mathbf{G} \mathbf{X}_o)^{-1} \\ &= \sigma^2 (\mathbf{X}_o^T (\mathbf{A}^T \mathbf{A})^{-1} \mathbf{X}_o)^{-1}. \end{aligned} \quad (5.45)$$

The $\hat{\mathbf{C}}_{\hat{\mathbf{a}}_o}$ diagonals are the LP coefficient's predicted estimation error variance, that is $\hat{C}_{\hat{\mathbf{a}}_o}(m, m) = \mathcal{E}\{(a_o(m) - \hat{a}_o(m))^2\}$.

Since above the threshold the LP coefficient's estimation error covariance matrix achieves efficiency, the method from [11] can be invoked to obtain the frequencies' estimation error covariance matrix

$$\mathbf{J}^{-1}(\hat{\mathbf{f}}) = \mathbf{H}^T \mathbf{J}^{-1}(\mathbf{a}_o) \mathbf{H}, \quad (5.46)$$

where the matrix \mathbf{H} is defined as $H(m, p) = \frac{\partial w_p}{\partial a_o(m)}$, and where w_p is the mapping from LP coefficients to frequency. Now, the unique mapping of LP coefficients to frequencies for two sinusoids is⁴

$$f_p = w_p(\mathbf{a}_o) = \frac{1}{2\pi} \cos^{-1} \left(\frac{-a(1) + (-1)^{p+1} \sqrt{a(1)^2 - 4a(2) + 8}}{4} \right). \quad (5.47)$$

Let $g_p = \frac{-a(1) + (-1)^{p+1} \sqrt{a(1)^2 - 4a(2) + 8}}{4}$, then using the above equation, the following derivatives can be calculated for the matrix \mathbf{H} (values of derivatives from [7])

$$\frac{\partial w_p(\mathbf{a}_o)}{\partial a_o(1)} = \frac{1}{8\pi \sqrt{1 - g_p^2}} \left[-1 - \frac{(-1)^p a(1)}{\sqrt{a(1)^2 - 4a(2) + 8}} \right] \quad (5.48)$$

$$\frac{\partial w_p(\mathbf{a}_o)}{\partial a_o(2)} = \frac{1}{8\pi \sqrt{1 - g_p^2}} \left[2 \frac{(-1)^p}{\sqrt{a(1)^2 - 4a(2) + 8}} \right]. \quad (5.49)$$

The above derivatives coupled with (5.46) yields

$$\hat{\mathbf{C}}_{\hat{\mathbf{f}}} = \mathbf{H}^T \hat{\mathbf{C}}_{\mathbf{a}_o} \mathbf{H}, \quad (5.50)$$

where $\hat{\mathbf{C}}_{\hat{\mathbf{f}}}$ is the frequency estimation error covariance the values of the matrix \mathbf{H} are defined in (5.48) and (5.49). The estimated error variance of the individual frequency estimates lie along the diagonal of the estimated frequency error covariance, $\hat{\mathbf{C}}_{\hat{\mathbf{f}}}(p, p) = \mathcal{E}\{(f_p - \hat{f}_p)^2\}$.

Because of the non-linearity of the transformation in (5.47), it is very difficult to calculate the value of ρ in (5.37) analytically. Therefore, Monte Carlo simulations are employed to determine the percentage of estimates within one, two and three standard deviations of the corresponding predicted variance to determine confidence intervals above threshold.

5.2.4 IGLS Algorithm Simulations. MC simulations are performed to validate the IGLS algorithm. The signal (5.18), with two real sinusoids, is considered in all of the

⁴For five sinusoids or greater a closed form relationship is not possible.

simulations. In the simulations, the experimental MSE is calculated as

$$\text{MSE} = \frac{1}{M} \sum_{i=1}^M (f - \hat{f}_i)^2 \quad (5.51)$$

where M is the number of MC trials and \hat{f}_i is the i th frequency estimate. The negative log of the MSE is plotted to highlight good performance. The SNR is defined as $-10 \log_{10}(2\sigma^2)$.

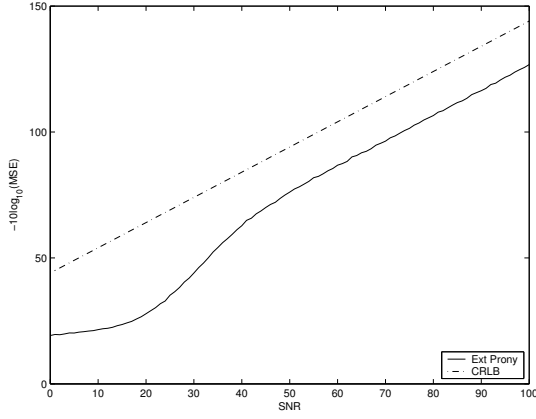
The bias is calculated as

$$\text{bias} = \frac{1}{M} \sum_{i=1}^M (f - \hat{f}_i). \quad (5.52)$$

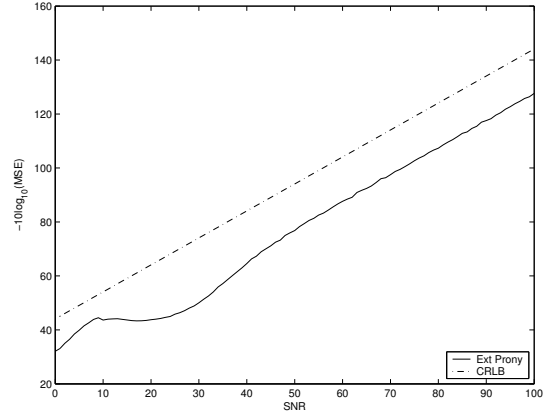
The emphasis is on signals with low SNR, short data record, and close frequencies to demonstrate the robustness of the IGLS algorithm-based parametric receiver in difficult estimation environments.

Figure 5.1 contains a plot of MSE vs. SNR for a Monte Carlo (MC) simulation calculated at every 1 dB using the EPM estimation algorithm with simulation parameters: $N=32$, $[A_1 = 1, f_1 = 0.227, \phi_1 = \frac{4\pi}{3}]$, $[A_2 = 1, f_2 = 0.207, \phi_2 = \frac{\pi}{3}]$; $SNR = -10 \log_{10}(2\sigma^2)$, $M=1000$. Note that the EPM does not achieve the CRB.

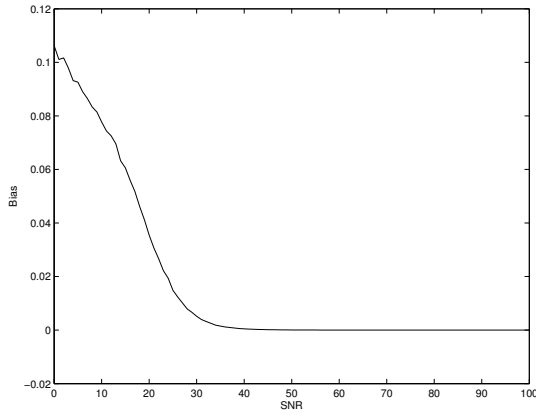
Figure 5.2 contains a plot of MSE vs. SNR for a MC simulation calculated at every 0.5 dB using the IGLS algorithm with the same parameters as Figure 5.1. The initial estimate for Figure 5.2 is taken from the extended Prony method estimate by setting $A^T A = I$ in Equation (5.36). From Figures 5.2(a) and 5.2(b), if the noise threshold is defined where the experimental MSE is within 2 dB of the CR bound, then the noise threshold for f_1 and f_2 is 10 dB and 12 dB respectively. Below the noise threshold, the algorithm's performance quickly drops well below the CRB because the noise has overwhelmed the estimation algorithm's ability to estimate the signal. The noise threshold is inherent to non-linear estimation. As expected, the experimental MSE achieves the CRB above the noise threshold since the IGLS algorithm is a ML estimator of frequency. Below the noise threshold, the estimates are biased, as can be seen in Figures 5.2(c) and 5.2(d) thus comparison to the CRB is not appropriate. However, above threshold the estimates are unbiased, and CRB comparison is appropriate. Finally, note by comparing Fig. 5.3 to Fig. 5.1 that the IGLS algorithm significantly outperforms the EPM algorithm.



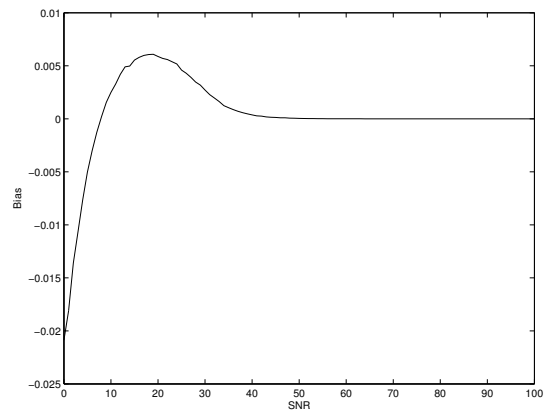
(a) \hat{f}_1 MSE



(b) \hat{f}_2 MSE



(c) \hat{f}_1 Bias



(d) \hat{f}_2 Bias

Figure 5.1: Extended Prony Method Estimation Accuracy.

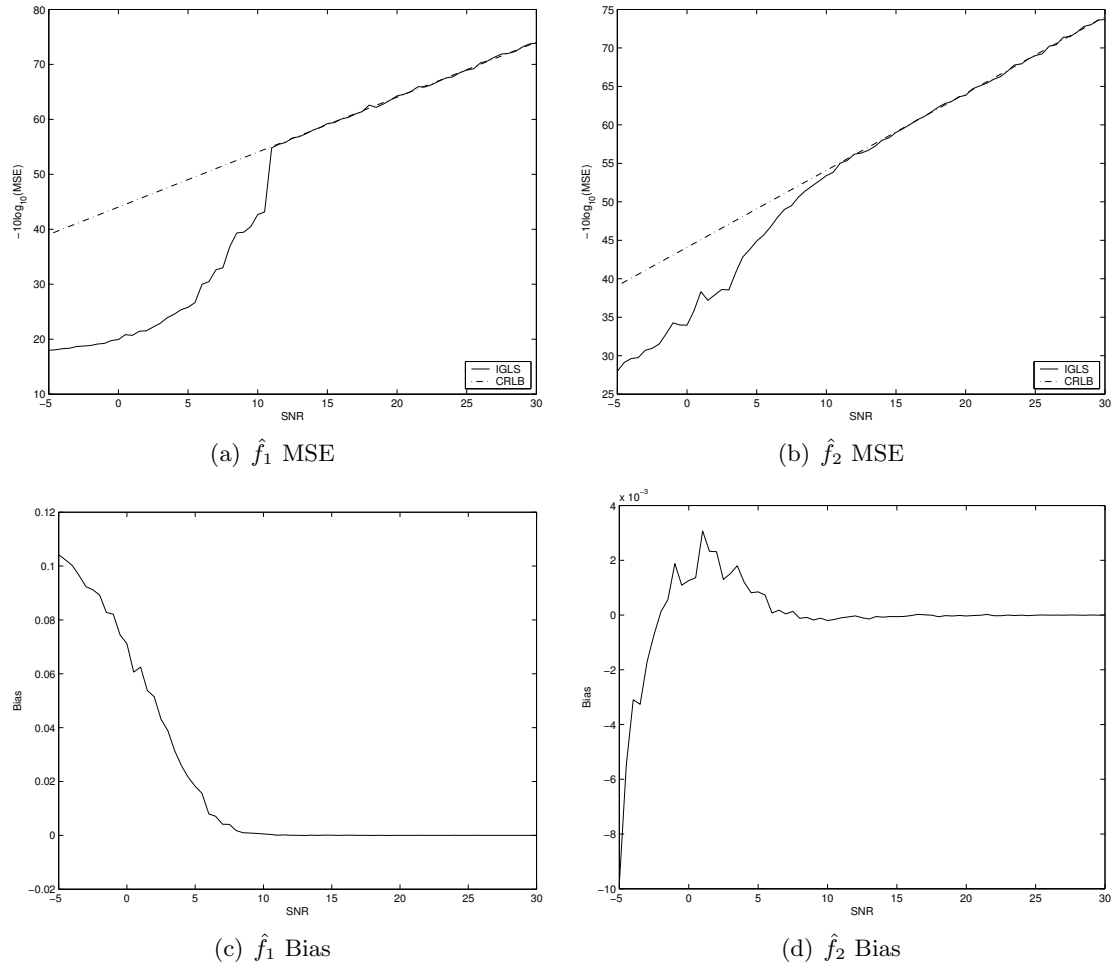


Figure 5.2: IGLS Estimation Accuracy with an EPM initial guess and N=32.

Figure 5.3 contains the IGLS algorithm Monte Carlo simulation results for the same parameters as Figure 5.2, except the initial guess is now *assumed* to be obtained from the closest 32 point FFT sample frequency point to the two signals frequencies. This FFT frequency sample point is used for both initial frequencies guesses and is converted to the initial LP coefficients guess by using Table 5.1. From Figures 5.3(a) and 5.3(b), if the noise threshold is defined where the experimental MSE is within 2 dB of the CR bound, then the noise threshold for f_1 and f_2 is 4.5 dB and 6 dB respectively. Thus, a better noise threshold is obtained by using more information about the frequencies values. As expected, the experimental MSE achieves the CR bound above the noise threshold since the IGLS algorithm is a MLE of frequency. Note from Figures 5.3(c) and 5.3(d) that the estimate becomes unbiased above the noise threshold, hence comparison to the CRB above the threshold is appropriate.

Figure 5.4 contains the IGLS algorithm Monte Carlo simulation results for the same parameters as Figure 5.3 including using the same 32 point FFT frequency sample point as the initial guess, except the number of sample points is increased to $M=128$. The IGLS algorithm noise threshold in Figures 5.4(a) and 5.4(b) for these parameters decreased dramatically to below -5 dB. Note that the bias in Figures 5.4(c) and 5.4(d) is negligible for all SNR's considered.

Figure 5.5 contains the IGLS algorithm Monte Carlo simulation results for the same parameters as Figure 5.4, except the initial guess is from the EPM. The IGLS algorithm noise threshold for the frequencies in Figures 5.5(a) and 5.5(b) is 7 dB and 5 dB respectively, much higher than when an initial guess is provided. Thus increasing the data length by a factor of four only decreases the noise threshold by 5 dB for both frequencies when using the extended Prony method to initialize the estimate. The jagged anomaly below the noise threshold contained in Figure 5.5(a) is partially explained by zooming in around the anomaly in both the bias and frequency as in Figure 5.6 and noticing that there is a slight rise in bias at the same point as the anomaly, which probably means the IGLS algorithm is converging to a local minimum more often. The IGLS MC simulations in [8] and [7] exhibited the same type of anomaly below the threshold.

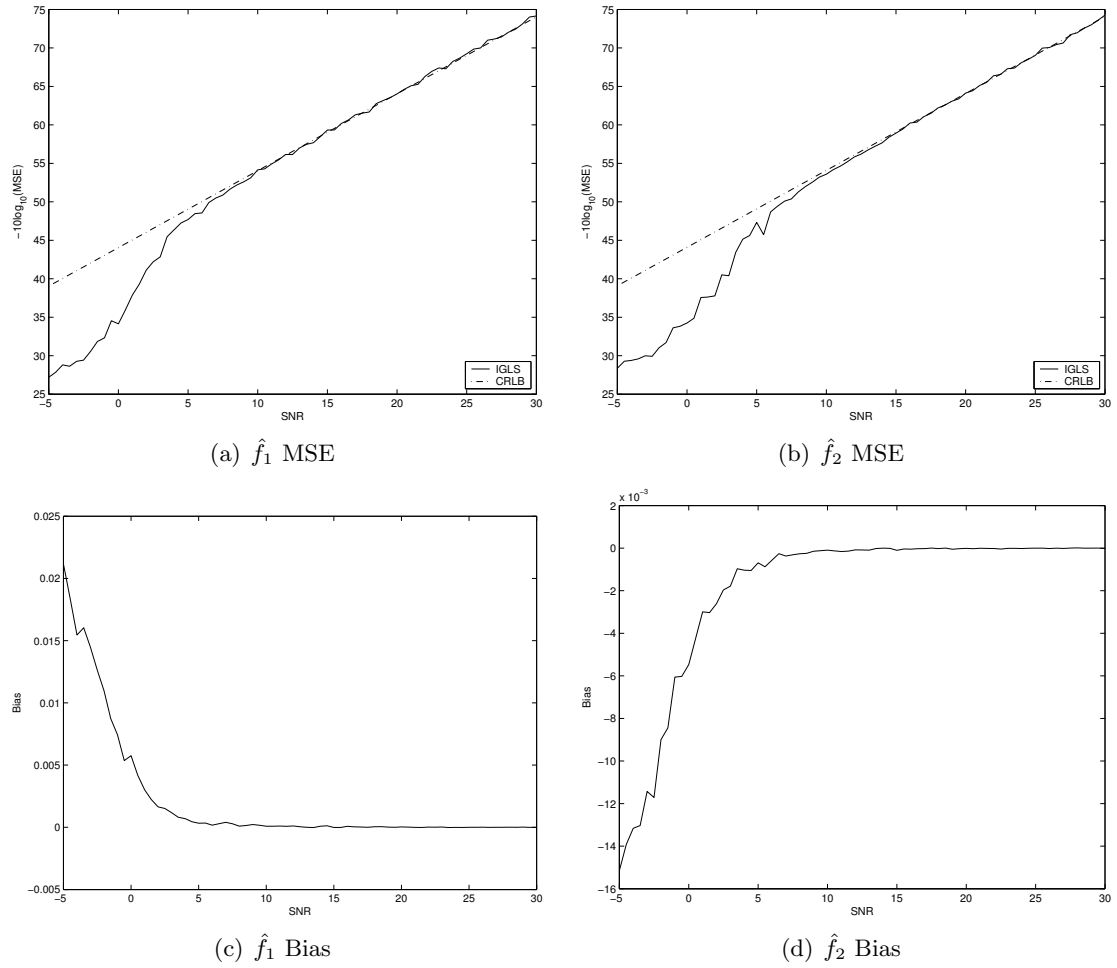


Figure 5.3: IGLS Estimation Accuracy with an FFT initial guess and $N=32$.

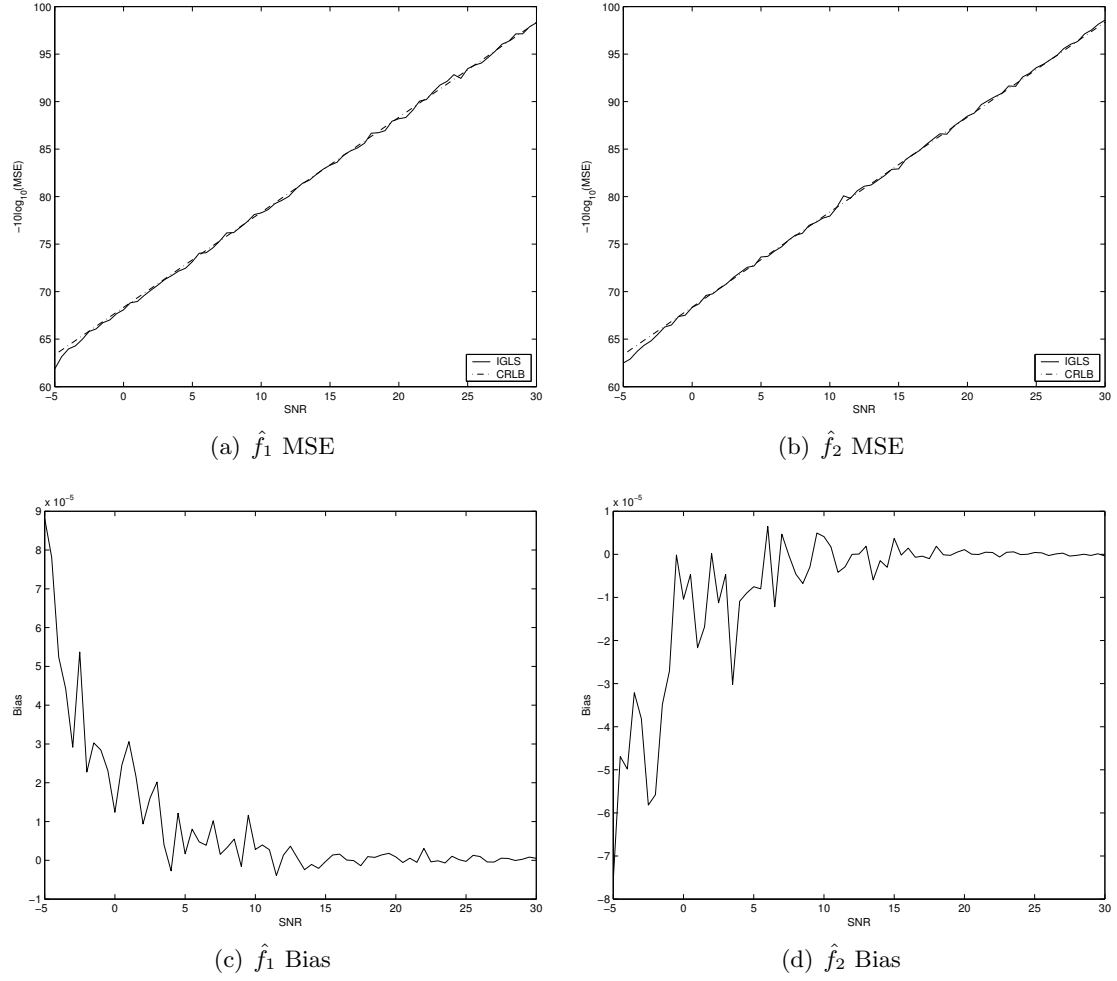


Figure 5.4: IGLS Estimation Accuracy with an FFT initial estimate and $N=128$.

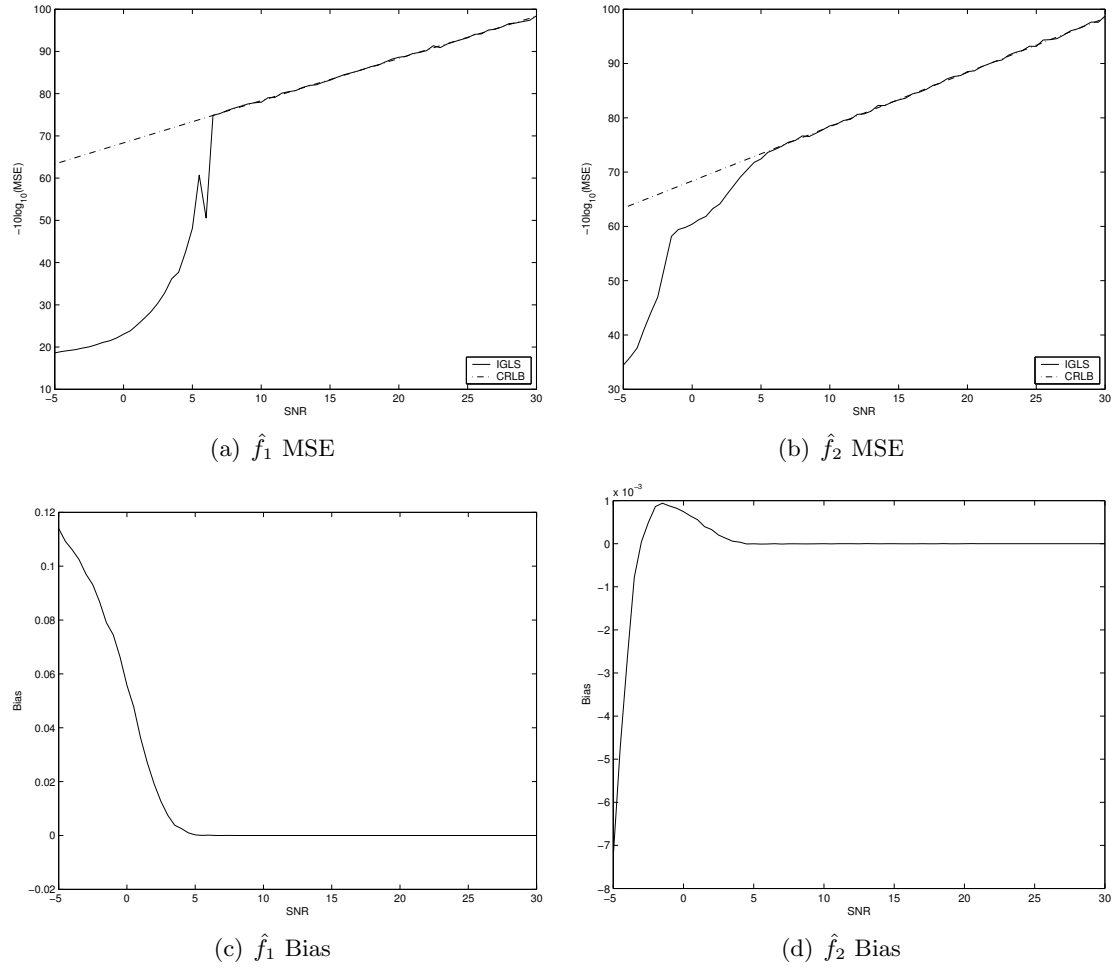


Figure 5.5: IGLS Estimation Accuracy with an EPM initial estimate and $N=128$.

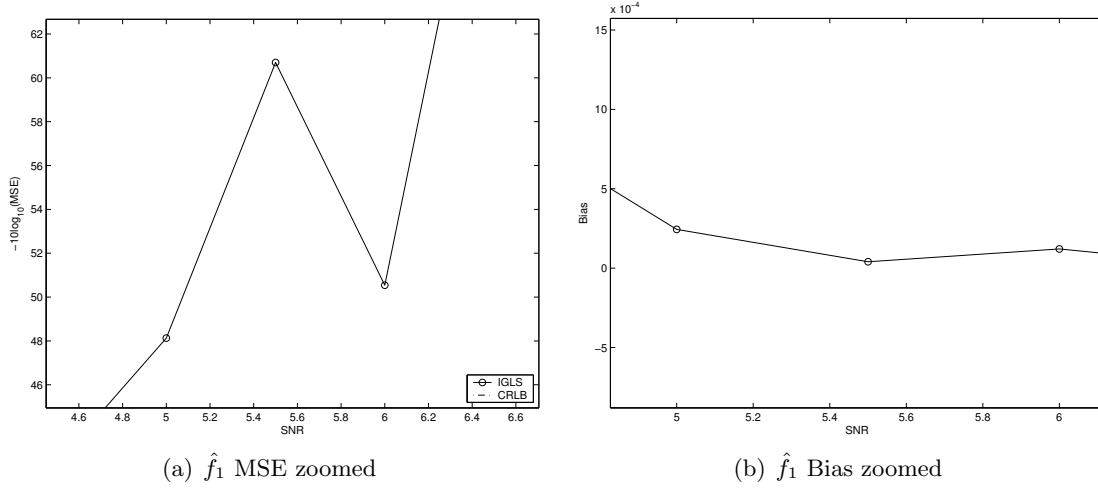


Figure 5.6: **Figure 5.5(a) zoom analysis:** Spike area of Figure 5.5(a) zoomed in along with bias of Figure 5.5(b). Note the dip in experimental bias which coincides with the spike reduction in experimental MSE.

5.2.4.1 IGLS Confidence Interval Simulations. Figure 5.7 contains a comparison of the average predicted LP coefficient estimation error variance for the signal of Fig. 5.1

$$\text{Var}_{pred}\{\hat{a}_o(m)\} = \frac{1}{M} \sum_{i=1}^M \hat{C}_{\hat{\mathbf{a}}_o}^i(m, m), \quad (5.53)$$

and the MC experimentally obtained variance

$$\text{Var}_{exp}\{\hat{a}_o(m)\} = \frac{1}{M-1} \sum_{i=1}^M (\hat{a}_o(m)_i - \text{mean}(\hat{a}_o(m)))^2, \quad (5.54)$$

where mean is calculated as $\frac{1}{M} \sum_{i=1}^M \hat{a}_o^i(m)$. Also plotted is the MSE between the calculated variance and each variance estimate. At 11 dB for both $\hat{a}(1)$ and $\hat{a}(2)$, the experimental variance converges to the calculated variance and the MSE is negligible. At this point the noise power can be neglected and (5.45) becomes a good estimate of the variance.

Fig. 5.8 establishes confidence intervals for frequency estimates via Monte Carlo simulation for the signal of Fig. 5.1. At each SNR point, the number of frequency estimates

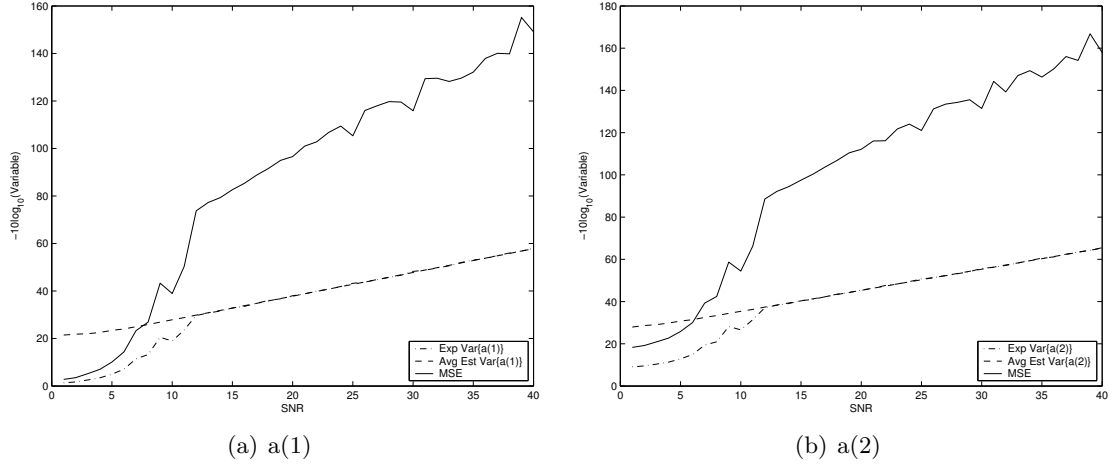


Figure 5.7: Average predicted LP estimation error variance, MC experimental variance, and MSE between MC experimental variance and predicted LP estimation error variance versus SNR.

within $K \sigma$ is calculated by

$$\sum_{i=1}^M (|\hat{f}_i - f| < k\hat{\sigma}_i) \text{ for } k = 1, 2, 3. \quad (5.55)$$

where $\hat{\sigma}_i$ is calculated using (5.50). From Fig. 5.8, the confidence intervals are valid for f_1 and f_2 greater than 11 dB. Rough estimates of ρ are 0.7, 0.95, and less than 0.99 for $K = 1, 2, 3$. Thus, good data driven confidence intervals are established using the measurements and knowledge of the noise variance.

In light of the results of the analysis and the MC simulations, it is apparent that the IGLS algorithm yields Maximum Likelihood estimates of frequencies and therefore, comparison to the IDR-CRB is valid *above the noise threshold*.

5.3 IGLS algorithm-based Parametric Receiver compared to the IDR-CRB

The IGLS algorithm-based parametric receiver, which is shown above to yield Maximum Likelihood estimates, is compared to the IDR-CRB by employing a Monte Carlo simulation. The simulation signal is defined for these simulations as

$$x(n) = A_1 \cos(2\pi f_1 t + \phi_1) + A_2 \cos(2\pi f_2 t + \phi_2) + n(t). \quad n = 0 \dots N - 1 \quad (5.56)$$

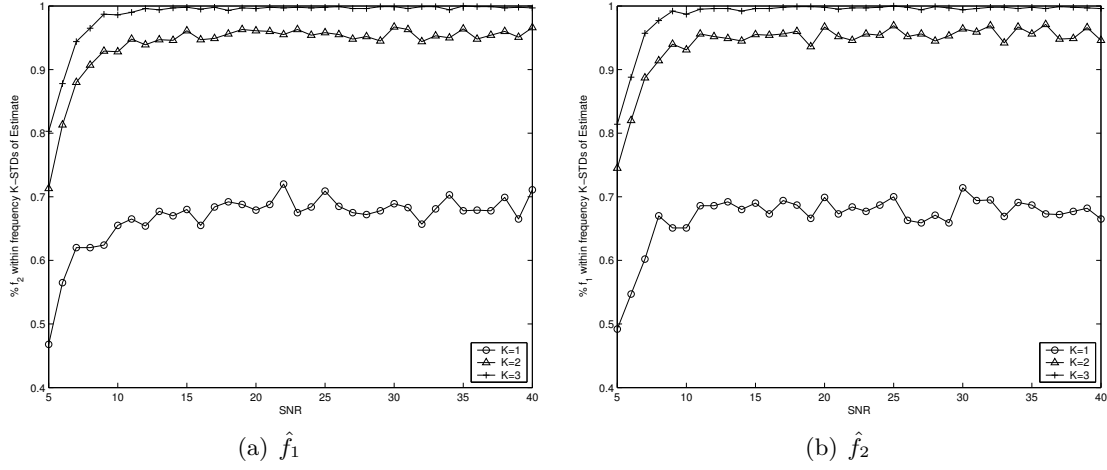


Figure 5.8: Frequency Estimate Confidence Intervals for $K = 1, 2$, and 3σ 's.

where A_{2b} is the minimum value of A_2 for the ML Estimator to still attain the desired MSE of f_2 as determined by the IDR-CRB. The simulation analysis follows the flowchart of Figure 5.9. First, the simulation parameters for each frequency separation of interest are input into the Fig. 4.3 IDR-CRB routine. If the IDR-CRB routine finds the parameters at any frequency separation not achievable, the parameters are not considered by the IGLS algorithm Monte Carlo simulation in the next step. If the parameters are viable, the IDR-CRB routine generates the A_2 bound amplitude, A_{2b} ; the lowest A_2 amplitude that will still theoretically achieve the given parameters. The IDR-CRB is plotted for valid A_{2b} values when this routine is finished. Also, as will become apparent from the simulation results, the A_{2b} SNR is also an important analysis tool and is defined as

$$SNR_{A_{2b}} = 10 \log \left(\frac{A_{2b}^2}{2\sigma^2} \right) \quad (5.57)$$

The $SNR_{A_{2b}}$ is also plotted after the IDR-CRB routine. The achievable parameters along with the corresponding A_{2b} values are sent to the next step, which is a Monte Carlo simulation of the signal defined in Equation (5.56). At each frequency separation value Δf , the corresponding A_{2b} amplitude is assigned along with the signal parameters listed in the caption and 1000 independent IGLS Monte Carlo trials are performed. The resulting experimental MSE and bias for \hat{f}_1 and \hat{f}_2 are plotted. For a successful experimental confirmation of the IDR-CRB, the \hat{f}_1 IGLS estimate experimental MSE should be less

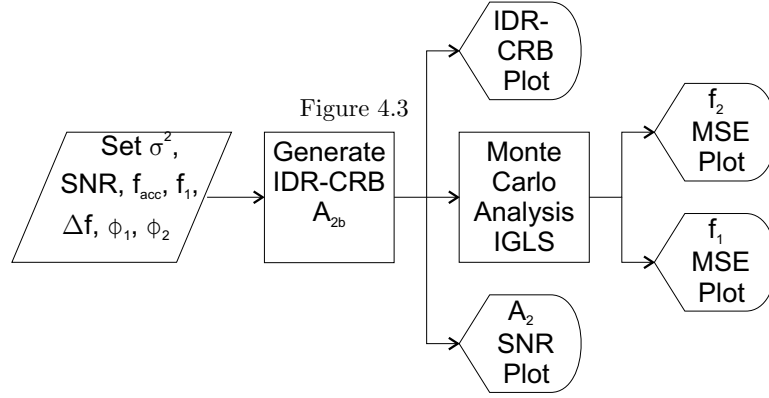


Figure 5.9: IDR-CRB IGLS Performance Analysis Flowchart.

than the desired RMS frequency, f_{acc}^2 , and the \hat{f}_2 IGLS estimate experimental MSE should equal the desired f_{acc}^2 for all frequency separation values.

Figure 5.10 contains the MC results for the desired RMS frequency estimation accuracies of $f_{acc} = \frac{1}{30N}$ and $f_{acc} = \frac{1}{10N}$ with initialization via the EPM and decreasing Δf evaluated at 0.001 increments for the parameters: $[A_1 = 1, f_1 = 0.207, \phi_1 = 0]$, $[A_2 = A_{2b}, f_2 = f_1 - \Delta f, \phi_2 = N\pi f_2 - \pi - N\pi f_1]$; $SNR = 10 \log_{10}(\frac{A_1}{2\sigma^2})$. In Figure 5.10(c), the estimates experimental MSE clearly shows the IGLS algorithm-based parametric receiver achieves the IDR-CRB for all applicable values since \hat{f}_1 MSE is below the desired MSE at all points and the \hat{f}_2 achieves the desired MSE within 1 dB at all points. In Figure 5.10(e), the experimental bias is negligible, thus comparison to the desired MSE is applicable for both frequency estimates. In Figure 5.10(d), the estimates MSE does not achieve the IDR-CRB for all applicable values. Noting that the SNR of A_{2b} of Figure 5.10(b) is well below the SNR of A_{2b} of Figure 5.10(a) and that the bias is no longer negligible in 5.10(f), the conjecture is the noise threshold of the IGLS algorithm has been exceeded for the parameter combination.

Figure 5.11 contains the performance analysis results for the same parameters as Figure 5.10 with initialization via the closest frequency sample of a 32 point FFT. Figure 5.11(c) matches closely to Figure 5.10(c), achieving the desired MSE within 1 dB for all applicable points. However, the \hat{f}_2 MSE in Figure 5.11(d) achieves the desired MSE within 4 dB for all applicable values, which means the estimate is right at the FFT initialized

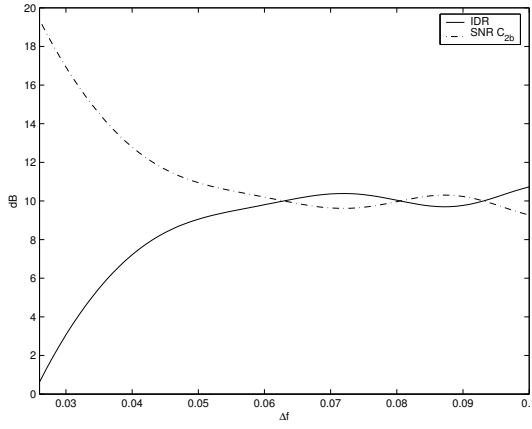
IGLS algorithm's noise threshold and the noise threshold is lower for the FFT initialized IGLS algorithm, as expected.

Figure 5.12 contains the performance analysis results with the measurement samples increased to $N = 128$, the desired RMS frequency tightened to $f_{acc} = \frac{1}{40N}$ with initializations via EPM or closest 32 point FFT frequency sample point. The IGLS algorithm performs as expected, once again validating the derived IDR-CRB in the FFT initialization. The noise threshold is once again encountered with the EPM initialization⁵.

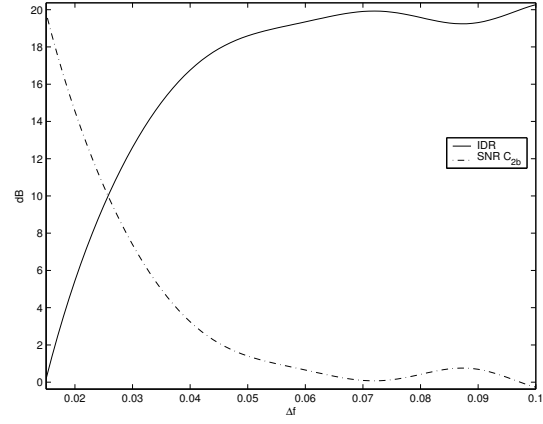
Thus, the Instantaneous Dynamic Range Cramer Rao Bound algorithm is validated using the IGLS algorithm. From the experimental results, the IDR-CRB is useful for tight bounds on parametric receivers performance. However, because of the noise threshold, the IDR-CRB does not provide a bound that can be used for parametric receiver analysis for loose frequency estimation requirements. Thus, in the next section, the author proposes a method to determine the IDR for a parametric receiver for a loose frequency estimate requirement.

5.3.1 IGLS Algorithm-based Parametric Receiver IDR for Loose Frequency Estimates. Loose frequency estimates are obtained above the noise threshold for a parametric receiver. When the amplitude ratio is high, so that the low amplitude carrier is buried in noise and the measurement is basically of a single carrier, overmodelling becomes an issue that causes both frequency estimates to deteriorate (the CRB does not consider this issue) as can be seen in Fig. 5.10(d). In an IGLS algorithm-based parametric receiver, for loose frequency estimates, the amplitude ratio at the point where the estimate begins to deteriorate can be considered the IDR for loose frequency estimate requirements. If the lower amplitude signal is below the threshold, it is better to reduce the model order to accurately estimate the higher amplitude sinusoid. Fig. 5.13 is a MC simulation with the same parameters as Fig. 5.2, except the Sinusoid 1 SNR is fixed at 23 dB and the A_2 SNR is increased in 0.5 dB steps by increasing the A_2 amplitude. For Sinusoid 2 SNR below 7.5 dB, the frequency estimates for Sinusoid 1 are almost 20 dB below efficiency, even though

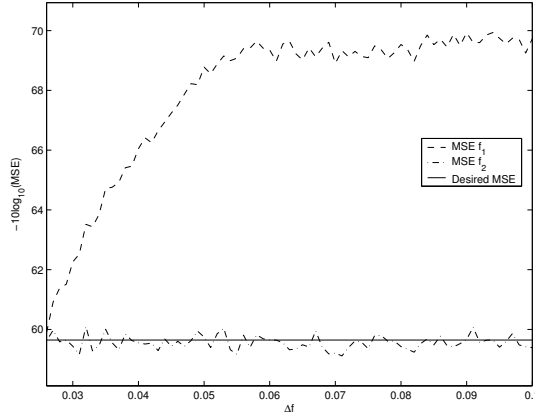
⁵This noise threshold will be encountered even by functions that minimize the objective functions for the two frequency estimates directly. It is inherent to non-linear estimation.



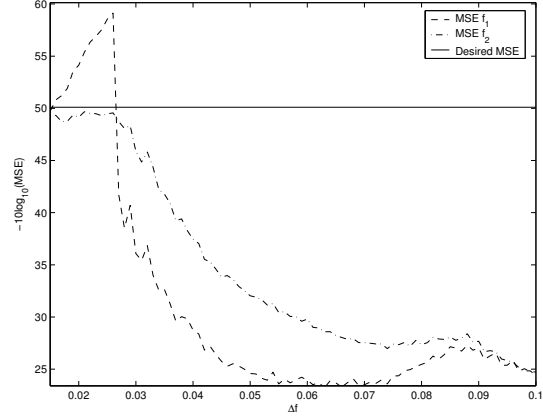
(a) IDR-CRB, SNR A_{2b} , $f_{acc} = \frac{1}{30N}$



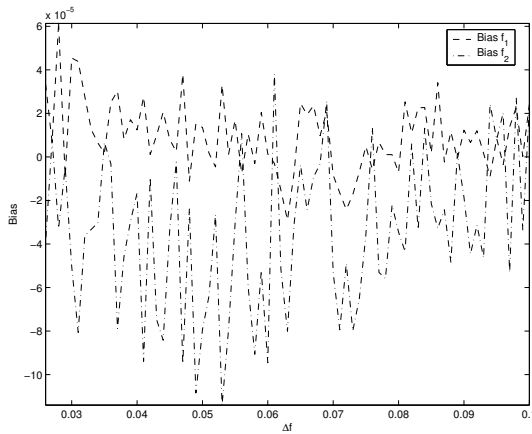
(b) IDR-CRB, SNR A_{2b} , $f_{acc} = \frac{1}{10N}$



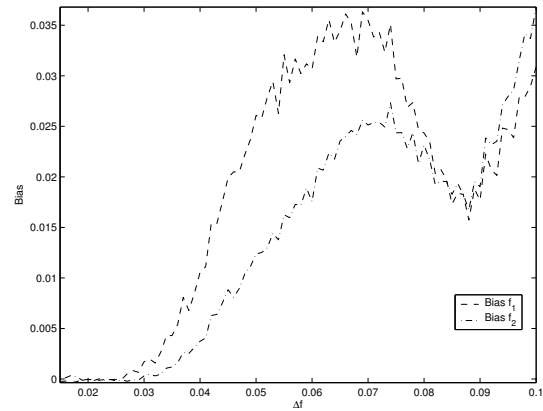
(c) \hat{f}_i MSE, $f_{acc} = \frac{1}{30N}$



(d) \hat{f}_i MSE, $f_{acc} = \frac{1}{10N}$

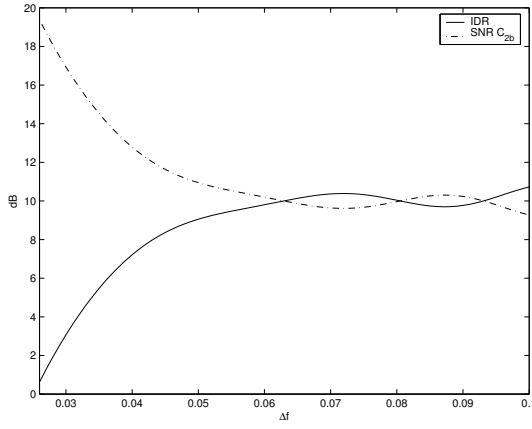


(e) \hat{f}_i Bias, $f_{acc} = \frac{1}{30N}$

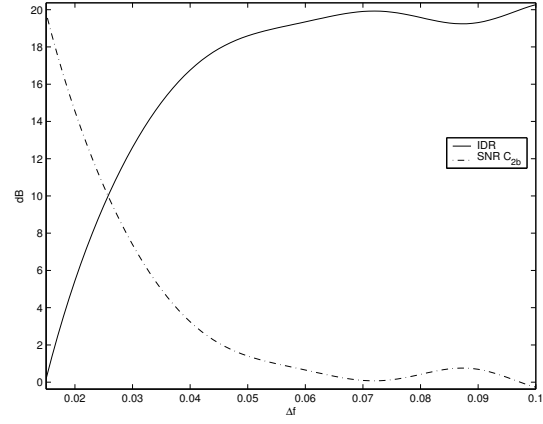


(f) \hat{f}_i Bias, $f_{acc} = \frac{1}{10N}$

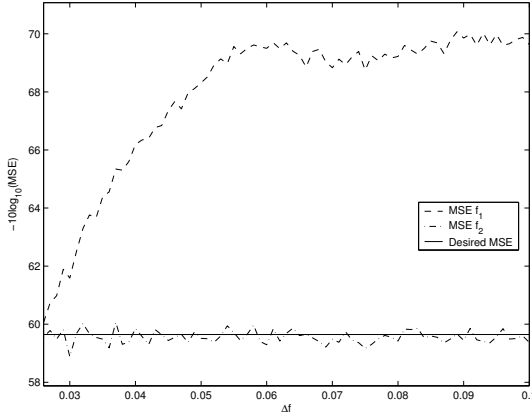
Figure 5.10: IGLS performance for IDR-CRB A_{2b} (EPM).



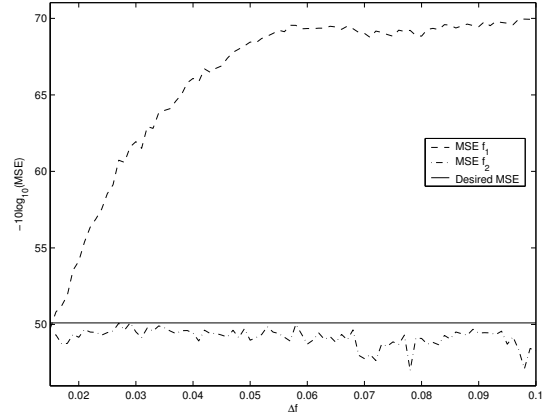
(a) IDR-CRB, SNR A_{2b} , $f_{acc} = \frac{1}{30N}$



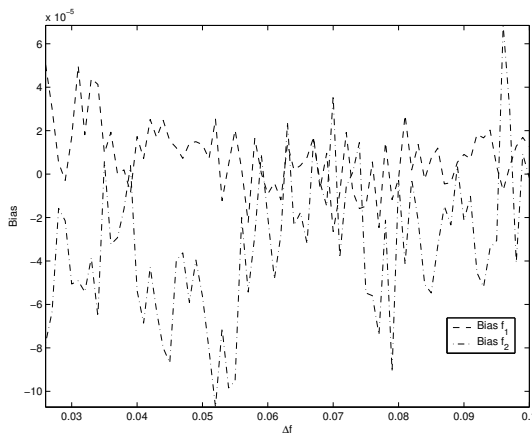
(b) IDR-CRB, SNR A_{2b} , $f_{acc} = \frac{1}{10N}$



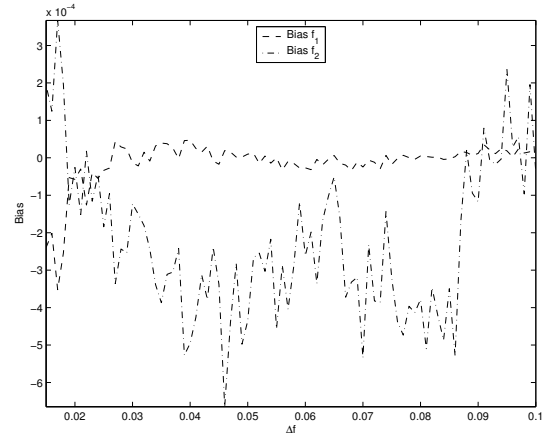
(c) \hat{f}_i MSE, $f_{acc} = \frac{1}{30N}$



(d) \hat{f}_i MSE, $f_{acc} = \frac{1}{10N}$

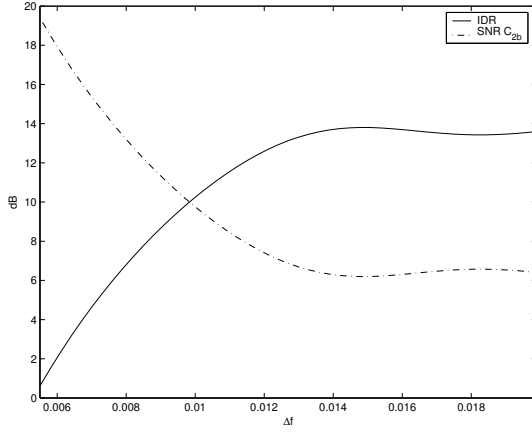


(e) \hat{f}_i Bias, $f_{acc} = \frac{1}{30N}$

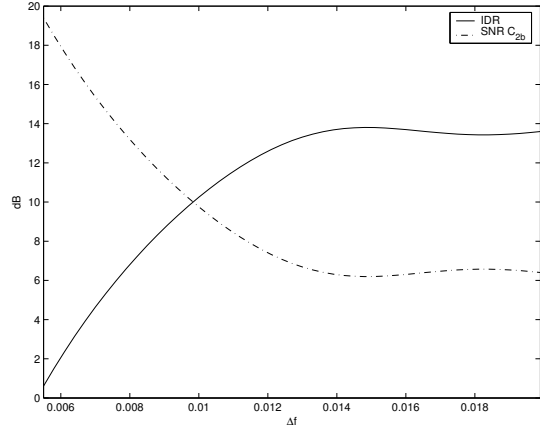


(f) \hat{f}_i Bias, $f_{acc} = \frac{1}{10N}$

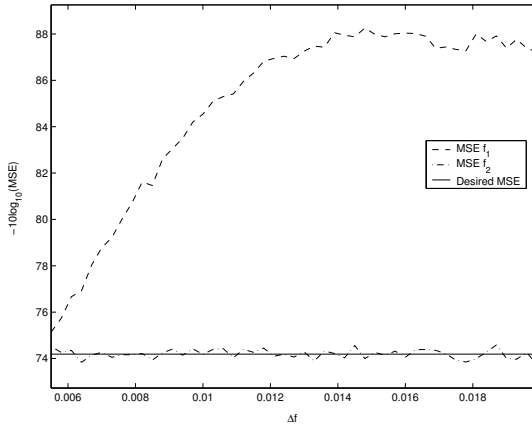
Figure 5.11: IGLS performance for IDR-CRB A_{2b} (FFT).



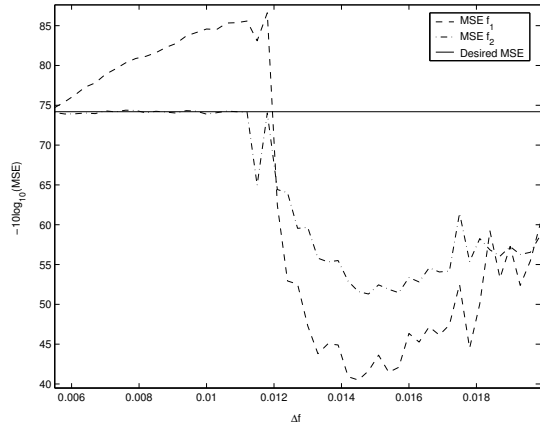
(a) IDR-CRB, SNR A_{2b} , FFT init



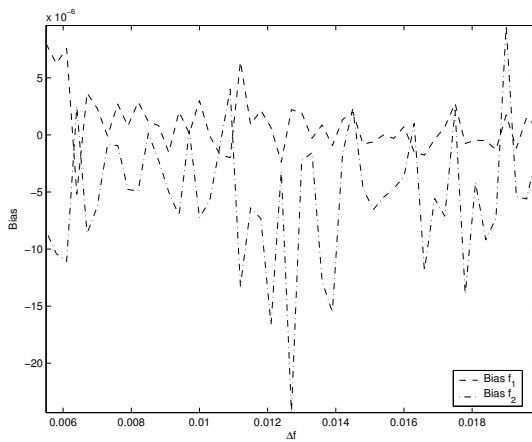
(b) IDR-CRB, SNR A_{2b} , EPM init



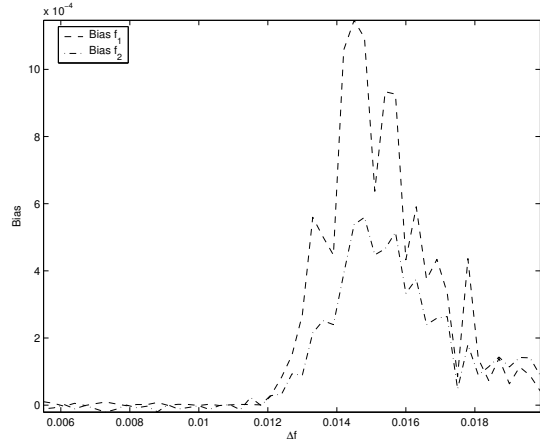
(c) \hat{f}_i MSE, FFT init



(d) \hat{f}_i MSE, EPM init



(e) \hat{f}_i Bias, FFT init



(f) \hat{f}_i Bias, , EPM init

Figure 5.12: IGLS performance for IDR-CRB A_{2b} ($M=128$, $f_{acc} = \frac{1}{40N}$).

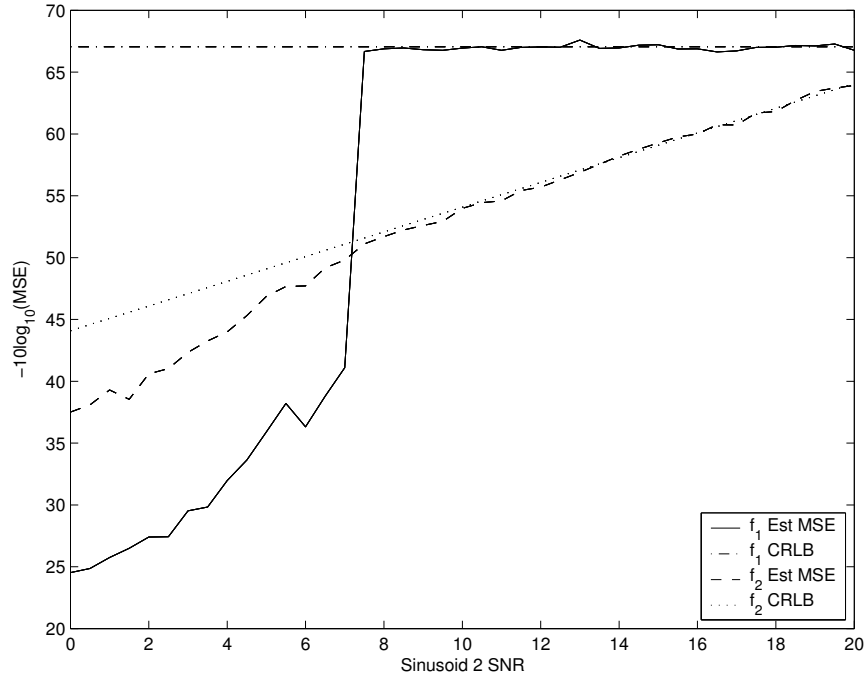


Figure 5.13: IDR determination for two sinusoids in white noise.

sinusoid 1 has an SNR of 23 dB. In this situation, the underlying model order in the algorithm should be reduced to efficiently estimate Sinusoid 1. At 7.5 dB both sinusoids are measured efficiently, thus the IDR is $23 - 7.5 = 15.5$ dB. This definition and simulation of the IGLS parametric algorithm's IDR for loose frequency estimates along with the IGLS algorithm development has been submitted for publication [29].

5.4 Conclusion

The IGLS frequency estimation algorithm is developed and shown to achieve ML estimates. The IDR-CRB is then experimentally verified using the IGLS algorithm-based parametric receiver for tight frequency estimate requirements. For loose requirements, the IDR-CRB is shown to be unachievable due to the noise threshold inherent to non-linear estimation. Thus, an alternate method to determine the IGLS algorithm-based parametric receiver IDR for loose estimation accuracies is proposed by determining the threshold point where both signals are measured efficiently.

VI. Conclusions

6.1 Introduction

This thesis investigates the EW receiver's IDR for the following IDR definition: IDR is defined as the maximum signal amplitude ratio for a given frequency estimation accuracy, a given frequency separation and a given SNR [5]. The measured signal is assumed to consist of multiple sinusoidal tones in white noise that fill the entire measurement window, i.e.

$$x(n) = s(n) + w(n), \quad n = 0 \dots N - 1 \quad (6.1)$$

Two types of EW receivers are considered; a DFT-Based Intercept Receiver and an IGLS Algorithm-Based Parametric Receiver. In Chapter III, the DFT-Based Intercept Receiver, using the novel SLR method, is evaluated for IDR. The results provide numerical estimates for 57 dB of IDR. The resulting analysis has a direct impact on digital EW receiver analysis and design. In Chapter IV, the method used to calculate the IDR-CRB in [1] is simplified, and the IDR-CRB is extended to real signals. In Chapter V, the novel IGLS frequency estimation algorithm, originally researched by [8] and [7], is completely developed and shown to yield ML results. The IDR-CRB validates using the IGLS Algorithm-Based Parametric Receiver for tight frequency estimate requirements. For loose frequency estimate requirements, the author proposes determining the parametric receiver IDR based on when both measurements achieve efficiency.

6.2 Contributions

In Chapter III, the main contribution is a solid method in order to evaluate a DFT-based intercept receiver's IDR. Also, the novel SLR method's IDR is evaluated and shown to yield the IDR in Table 3.1. This IDR is independent of bin spacing for signals separated by more than 2 bins and does not have the associated processing gain loss and widening of the main beam inherent to window based approaches.

In Chapter IV, an improved method to calculate the complex IDR-CRB is introduced. The old method in [1] relied on an iterative technique that is difficult to implement. The new method exploits the fact that the Fisher information matrix can be factored as shown

in [6] for a method that requires no iteration and is quite simple. The IDR-CRB is extended to real signals, again based on the results in [6]. Plots are provided to evaluate the results. Finally, it is firmly established that a receiver's frequency estimates should only be compared to the IDR-CRB if the estimates are unbiased, which is generally not the case in intercept receivers but is true for most parametric receivers.

In Chapter V, the novel IGLS frequency estimation algorithm, developed by Dr. Pachter and researched by Zahirniak [7] and Ingham [8], is completely developed and shown to yield ML estimates. The author feels the explanation of IGLS provided is the most concise and informative to date. The IDR-CRB is then evaluated using the IGLS Algorithm-Based Parametric Receiver. For tight frequency estimate requirements, the IDR-CRB is a valid bound on performance. For less stringent frequency estimate requirements, the author proposes determining the IDR based on when both estimates achieve efficiency. The author's loose definition of IDR coupled with the concise and informative description of IGLS has been submitted for publication [29].

6.3 Future Work

Areas of future work include

- Implement the SLR method results using a lookup table and compare to the ideal results in Table 3.1.
- Use the method of Chapter III to compare straight windowing results to the SLR method results for IDR in Table 3.1.
- Consider other non-parametric spectral/frequency estimation algorithms for the intercept receiver such as the minimum variance algorithm described in [13] and compare results for IDR to Table 3.1.
- Compare other algorithms to the IDR-CRB when tight frequency estimates are required.
- Apply the IGLS algorithm to other applications such as a discrete frequency rate estimator in a software radio.

- Research ways to improve the IGLS noise threshold when initialized by the EPM, such as an additional constraint.

6.4 Summary

The results in this thesis, whether taken collectively or individually, represent significant contributions to the field of Electronic Warfare. The IDR analysis performed in this thesis standardizes how the two types of EW receivers IDR should be evaluated. These contributions directly impact the design and updates for digital EW receivers. Thus, these results directly and positively impact USAF operations in the critical EW field.

Appendix A. Interference in an EW Receiver

A.1 Introduction

As with any system, noise interferes with the EW receiver measurements. Since the noise is random, the noise is characterized using statistics for mathematical analysis. The statistical noise model used throughout the thesis is developed below, with a brief review of random process theory preceding the noise model development.

A.2 Random Process Theory

Random signals consist of an ensemble of member functions. The signal measured in an experiment may only be a single member of a large ensemble of signals with a certain probability of selection associated with each member of the ensemble. Thus, instead of a deterministic mathematical description, random signals are specified in terms of their statistical characteristics, with the following being the most important:

- The mean of a random signal is defined as

$$\mu_x(n) = \mathcal{E} \{x(n)\}. \quad (1.1)$$

Thus, the mean of a random signal at time n is the expected value of the ensemble functions at time n .

- The autocorrelation of a random signal is defined as

$$R_{xx}(n, m) = \mathcal{E} \{x(n)x^*(m)\}. \quad (1.2)$$

where $R_{xx}(n, m)$ is an autocorrelation value. A signal is defined to be Wide Sense Stationary (WSS) if the autocorrelation depends only on the time difference, not the actual time (very important) and the mean is constant over time. Note that the Fourier transform of the autocorrelation function of a WSS process is the Power Spectral Density (PSD)- see Appendix B.

- The autocovariance of a random signal is defined as

$$C_{xx}(n, m) = R_{xx}(n, m) - \mu_x(n)\mu_x^*(m) \quad (1.3)$$

where $C_{xx}(n, m)$ is an autocovariance value.

- Note that the autocorrelation and the autocovariance can be extended to cross-correlation and cross-covariance between two separate signals.

The above concepts are applied in the next section to mathematically model thermal noise.

A.3 Thermal Noise

In 1827, the British Botanist Robert Brown observed that small pollen grains exhibit random motion in water. In 1905, Albert Einstein (who was unaware of Brown's work) showed that small particles (around 10^{-4} cm) move randomly due to the constant bombardment from the molecules of the medium [30]. This random movement is now called Brownian motion. In 1923, Norbert Wiener, using stochastic theory, derived a mathematical random process model for Brownian Motion called the Wiener Process [30].

The Wiener Process is used extensively to model the random motion of electrons in electronic devices such as resistors, capacitors, inductors, and semiconductor devices (which make up the RF amplifier of the EW receiver). These random fluctuations in electron density interfere with the information bearing signals that flow through these components. This interference is referred to as thermal noise. As the number of devices increases, the collection of Wiener Processes become a zero-mean, stationary Gaussian Process due to the Central Limit Theorem [30]. The Gaussian process model for thermal noise exhibits a PSD that is flat over a wide range of frequencies, and is referred to as Additive White Gaussian Noise (AWGN) [30].

The white noise PSD is [30]

$$S_{WW}(f) = \frac{N_o}{2} \text{ Joules/Hz} \quad (1.4)$$

where N_o is equal to kT (where k is boltzmann's constant, and T is the temperature in Kelvin of the noise source), and $S_{WW}(f)$ is the PSD of the white noise. This implies that the autocorrelation function which is the IFT of the PSD is a delta function,

$$R_{WW}(t) = \sigma^2 \delta(t), \quad (1.5)$$

where σ^2 is the noise variance. From (1.5), each realization of thermal noise in time is independent from the next realization. For the general case of colored or white noise, the distribution of real noise for any stationary process for the general N-variate, zero mean Gaussian case is given as [30]

$$f_W(\mathbf{w}) = (2\pi)^{-\frac{N}{2}} |\mathbf{R}|^{-\frac{1}{2}} \exp \left\{ -\frac{1}{2} \mathbf{w}^T \mathbf{R}^{-1} \mathbf{w} \right\}, \quad (1.6)$$

where the matrix \mathbf{R} is the covariance matrix of the noise (for white noise $\mathbf{R} = \sigma^2 \mathbf{I}$, where \mathbf{I} is the identity matrix) and \mathbf{w} is the AWGN vector. Thermal noise is assumed throughout the thesis.

Appendix B. Power Spectral Density and the Periodogram

B.1 Introduction

Although the DFS is used for the frequency estimation algorithm in Section 3.3, the Periodogram - an estimate of a WSS process's PSD ¹ - is still an important tool for frequency estimation, and, because the Periodogram is a power statistic, has a natural relation to the direct Maximum Likelihood estimate of multiple frequencies. Thus, in Section B.2, the deterministic PSD is developed. In Section B.3, the PSD of a WSS random signal is introduced and then estimated with the Periodogram.

B.2 Deterministic Power Spectral Density

If an arbitrary signal voltage is referenced to a one ohm resistor, then the energy of the signal is defined as [19]

$$E \triangleq \lim_{T \rightarrow \infty} \int_{-T}^T |x(t)|^2 dt, \quad (2.1)$$

and the power of the signal is defined as

$$P \triangleq \lim_{T \rightarrow \infty} \frac{1}{T} \int_{-\frac{T}{2}}^{\frac{T}{2}} |x(t)|^2 dt. \quad (2.2)$$

It is a well-known relationship [16, 19] that energy in the frequency domain equals the energy in the time domain

$$E = \int_{-\infty}^{\infty} |x(t)|^2 dt = \int_{-\infty}^{\infty} |X(f)|^2 df. \quad (2.3)$$

Equation (2.3) is known as Parseval's theorem. A similar property applies to the power relationship between the time and frequency representation of a signal [19]

$$P = \lim_{T \rightarrow \infty} \frac{1}{T} \int_{-\frac{T}{2}}^{\frac{T}{2}} |x(t)|^2 dt = \lim_{T \rightarrow \infty} \frac{1}{T} \int_{-\infty}^{\infty} |X(f)|^2 df. \quad (2.4)$$

¹Since the signal's contained in the measurement signal are deterministic, the measurement is actually a mixed process, this fact is normally ignored in frequency/spectral estimation.

For periodic signals the limiting operation can be ignored in the power equations of above, and T_o can be substituted for T , where T_o is the period of the signals. A similar relationship that was made in (2.3) can be applied in the discrete time and frequency domains

$$P = \sum_{n=0}^{N-1} |x(n)|^2 = \frac{1}{N} \sum_{k=0}^{N-1} |X(k)|^2. \quad (2.5)$$

Equation (2.4) can be rewritten as

$$P = \lim_{T \rightarrow \infty} \frac{1}{T} \int_{-\frac{T}{2}}^{\frac{T}{2}} |x(t)|^2 dt = \int_{-\infty}^{\infty} S_x(f) df. \quad (2.6)$$

where $S_x(f)$ is the PSD of a signal defined as

$$S_x(f) = \lim_{T \rightarrow \infty} \frac{|X(f)|^2}{T}. \quad (2.7)$$

The discrete PSD is defined as

$$S_x[k] = \lim_{M \rightarrow \infty} \frac{1}{N} |X(k)|^2. \quad (2.8)$$

where N is the number of discrete frequency sample points. The PSD represents the power per unit Hertz of a signal. An interesting result is the equivalent operation in the time domain to the PSD

$$\begin{aligned} F^{-1} \{S_x\} &= \lim_{T \rightarrow \infty} \frac{1}{T} \int_{-\infty}^{\infty} |X(f)|^2 e^{j2\pi f\alpha} df \\ &= \lim_{T \rightarrow \infty} \frac{1}{T} \int_{-\infty}^{\infty} X(f) X(f)^* e^{j2\pi f\alpha} df \\ &= \lim_{T \rightarrow \infty} \frac{1}{T} \int_{-\infty}^{\infty} X(f) \left(\int_{-\frac{T}{2}}^{\frac{T}{2}} x(t) e^{-j2\pi ft} dt \right)^* e^{j2\pi f\alpha} df \\ &= \lim_{T \rightarrow \infty} \frac{1}{T} \int_{-\frac{T}{2}}^{\frac{T}{2}} x^*(t) \int_{-\infty}^{\infty} X(f) e^{j2\pi f(t+\alpha)} df dt \\ &= \lim_{T \rightarrow \infty} \frac{1}{T} \int_{-\frac{T}{2}}^{\frac{T}{2}} x^*(t) x(t+\alpha) dt \\ &= R_f(\alpha), \end{aligned} \quad (2.9)$$

where $R_f(\alpha)$ is the autocorrelation function and has a central role in random process theory.

The PSD can be employed in digital EW systems for the detection/estimation of sinusoids. Since the period of the sinusoids is unknown, the measurement time (window time length) is substituted for the period. Thus, the PSD of the signal in (3.3) is

$$S_x(f) = \frac{|X(f)|^2}{\tau}. \quad (2.10)$$

To make the task easier, rewrite $X(f)$ as

$$X(f) = AB + CD \quad (2.11)$$

where A,B,C, and D are defined as follows,

$$A = \frac{\tau A_1}{2} e^{-j(\pi f_1 \tau + \frac{\pi}{2})} \quad (2.12)$$

$$B = \text{sinc}(\tau(f + f_1))e^{-j\phi_1} - \text{sinc}(\tau(f - f_1))e^{j\phi_1} \quad (2.13)$$

$$C = \frac{\tau A_2}{2} e^{-j(\pi f_2 \tau + \frac{\pi}{2})} \quad (2.14)$$

$$D = \text{sinc}(\tau(f + f_2))e^{-j\phi_2} - \text{sinc}(\tau(f - f_2))e^{j\phi_2}. \quad (2.15)$$

Then the PSD of $x(t)$ is

$$S_x(f) = \frac{1}{\tau}(|AB|^2 + A^*B^*CD + ABC^*D^* + |CD|^2). \quad (2.16)$$

Although the above formula is for the continuous frequency case, it will match closely to the discrete PSD at the frequency sample points with slight differences due to the aliasing of the sinc function side-lobes. The cross terms of Equation (2.16) increase the frequency estimates bias for closely spaced sinusoids. The deterministic PSD plot results mirror the previous DFT magnitude plots in Chapter III for most results (since those results were reported in dB), except for the $\frac{1}{M}$ scaling term.

B.3 Periodogram

For WSS random signals, the PSD is defined as [13]

$$S_{XX}(f) = \lim_{T \rightarrow \infty} \mathcal{E} \left\{ \frac{|X_R(f)|^2}{T} \right\}. \quad (2.17)$$

Ignoring the expected value operator and using the available data yields the PSD estimate

$$\hat{S}_{XX}(f) = \frac{|X_R(f)|^2}{\tau}, \quad (2.18)$$

where $\hat{S}_{XX}(f)$ is called the Periodogram. The Periodogram is an inconsistent spectral estimator, i.e. the variance does not decrease as the number of measurements increases. The Periodogram is often employed for frequency detection/estimation. However, because the interpolation algorithms in Section 3.3 rely on phase information, the Periodogram is not used in this thesis.

Bibliography

1. J. B. Tsui, *Digital Techniques for Wideband Receivers*. Massachusetts: Artech House Publishers, second ed., 2001.
2. "Australia develops Blue Owl system," *Jane's International Defense Review*, vol. 37, p. 11, Jan. 2004.
3. D. D. Vaccaro, *Electronic Warfare Receiving Systems*. Massachusetts: Artech House Publishers, 1993.
4. D. C. Schleher, *Electronic Warfare in the Information Age*. Massachusetts: Artech House Publishers, 1999.
5. J. B. Tsui, M. H. Thompson, and W. McCormick, "Theoretical limit on instantaneous dynamic range of EW receivers," *Microwave Journal*, pp. 147–152, Jan. 1987.
6. D. C. Rife and R. R. Boorstyn, "Multiple tone parameter estimation from discrete-time observations," *The Bell System Technical Journal*, vol. 55, no. 9, pp. 1389–1410, 1976.
7. D. R. Zahirniak, *Parameter Estimation for Real, Filtered Sinusoids*. PhD thesis, Air Force Institute of Technology, Wright-Patterson AFB, Ohio, Sept. 1997. DTIC Report ADA331303.
8. E. A. Ingham, *Parameter Estimation for Superimposed Weighted Exponentials*. PhD thesis, Air Force Institute of Technology, Wright-Patterson AFB, Ohio, July 1996. DTIC Report ADA310879.
9. J. B. Y. Tsui. private communication, 2003.
10. S. M. Kay, *Fundamentals of Statistical Signal Processing: Estimation Theory*. Englewood Cliffs, NJ: Prentice Hall, 1993.
11. L. L. Scharf, *Statistical Signal Processing*. Reading, MA: Addison-Wesley, 1990.
12. H. L. Van Trees, *Detection, Estimation, and Modulation Theory: Part 1*. New York: John Wiley & Sons, 1968.
13. S. M. Kay, *Modern Spectral Estimation: Theory and Application*. Englewood Cliffs, NJ: Prentice Hall, 1988.
14. Y. Bresler and A. Macovski, "Exact maximum likelihood parameter estimation of superimposed exponential signals in noise," *IEEE Transactions on Acoustics, Speech, and Signal Processing*, vol. ASSP-34, pp. 1081–1089, Oct. 1986.
15. S. Kay and S. Saha, "Mean likelihood frequency estimation," *IEEE Transactions on Signal Processing*, pp. 1937–1946, July 2000.
16. F. G. Stremler, *Introduction to Communications Systems*. New York: McGraw Hill, third ed., 2001.
17. F. J. Harris, "On the use of windows for harmonic analysis with the Discrete Fourier Transform," *Proceedings of the IEEE*, vol. 66, pp. 51–83, Jan. 1978.

18. B. Smith and T. Hale, "An analysis of the effects of windowing on selected STAP algorithms," in *Proc. IEEE Radar Conference 2004 (Accepted)*, (Philadelphia, Pennsylvania), Apr. 2004.
19. R. E. Ziemer, W. H. Tranter, and D. R. Fannin, *Signals & Systems: Continuous and Discrete*. New Jersey: Prentice Hall, 1998.
20. M. D. Macleod, "Fast nearly ML estimation of the parameters of real or complex single tones or resolved multiple tones," *IEEE Transactions of Signal Processing*, vol. 46, pp. 141–148, Jan. 1998.
21. S. L. Marple, *Digital Spectral Analysis with Applications*. Englewood Cliffs, NJ: Prentice-Hall, 1987.
22. Y. T. Chan, J. M. M. Lavoie, and J. Plant, "A parameter estimation approach to estimation of frequencies of sinusoids," *IEEE Transactions on Acoustics, Speech, and Signal Processing*, vol. ASSP-29, pp. 214–219, Apr. 1981.
23. M. Pachter and O. R. Reynolds, "Identification of a discrete-time dynamical system," *IEEE Transactions on Aerospace and Electronic Systems*, vol. 36, no. 1, pp. 212–225, 2000.
24. O. R. Reynolds and M. Pachter, "Phasor approach to continuous-time system identification," *IEEE Transactions on Aerospace and Electronic Systems*, vol. 35, no. 2, pp. 683–699, 1999.
25. T. H. Li and B. Kedem, "Strong consistency of the contraction mapping method for frequency estimation," *IEEE Transactions on Information Theory*, vol. 39, pp. 989–997, May 1993.
26. J. M. Brown, *Optimal Inputs for System Identification*. PhD thesis, Air Force Institute of Technology, Wright-Patterson AFB, Ohio, Sept. 1995. DTIC Report ADA297483.
27. J. H. McClellan and D. Lee, "Exact equivalence of the Steiglitz-McBride iteration and IQML," *IEEE Transactions on Signal Processing*, vol. 39, pp. 509–512, Feb. 1991.
28. E. A. Ingham, J. Schofield, and M. Pachter, "Improved linear prediction for deep level transient spectroscopy analysis," *Journal of Applied Physics*, vol. 80, pp. 2805–2814, Sept. 1996.
29. M. Pachter and B. Smith, "An efficient frequency estimation algorithm using linear prediction," in *43rd IEEE Conference on Decision and Control (Submitted)*.
30. K. S. Shanmugan and A. M. Breipohl, *Random Signals: Detection, Estimation, and Data Analysis*. New York: John Wiley & Sons, 1988.

REPORT DOCUMENTATION PAGE				Form Approved OMB No. 074-0188	
<p>The public reporting burden for this collection of information is estimated to average 1 hour per response, including the time for reviewing instructions, searching existing data sources, gathering and maintaining the data needed, and completing and reviewing the collection of information. Send comments regarding this burden estimate or any other aspect of the collection of information, including suggestions for reducing this burden to Department of Defense, Washington Headquarters Services, Directorate for Information Operations and Reports (0704-0188), 1215 Jefferson Davis Highway, Suite 1204, Arlington, VA 22202-4302. Respondents should be aware that notwithstanding any other provision of law, no person shall be subject to a penalty for failing to comply with a collection of information if it does not display a currently valid OMB control number.</p> <p>PLEASE DO NOT RETURN YOUR FORM TO THE ABOVE ADDRESS.</p>					
1. REPORT DATE (DD-MM-YYYY) 23-03-2004		2. REPORT TYPE Master's Thesis		3. DATES COVERED (From – To) Jun 2003 – Mar 2004	
4. TITLE AND SUBTITLE ENHANCING THE INSTANTANEOUS DYNAMIC RANGE OF ELECTRONIC WARFARE RECEIVERS USING STATISTICAL SIGNAL PROCESSING				5a. CONTRACT NUMBER	
				5b. GRANT NUMBER	
				5c. PROGRAM ELEMENT NUMBER	
6. AUTHOR(S) Smith, Bryan, E., 1st Lt, USAF				5d. PROJECT NUMBER 04ENG145	
				5e. TASK NUMBER	
				5f. WORK UNIT NUMBER	
7. PERFORMING ORGANIZATION NAMES(S) AND ADDRESS(S) Air Force Institute of Technology Graduate School of Engineering and Management (AFIT/EN) 2950 Hobson Way Street, Building 640 WPAFB OH 45433-7765				8. PERFORMING ORGANIZATION REPORT NUMBER AFIT/GE/ENG/04-22	
9. SPONSORING/MONITORING AGENCY NAME(S) AND ADDRESS(ES) AFRL/SNRP Attn: Dr. James B. Tsui 2241 Avionics Building 620 N2-R1 WPAFB OH 45433 DSN: 785-6127 x4320 e-mail: James.Tsui@wpafb.af.mil				10. SPONSOR/MONITOR'S ACRONYM(S)	
				11. SPONSOR/MONITOR'S REPORT NUMBER(S)	
12. DISTRIBUTION/AVAILABILITY STATEMENT APPROVED FOR PUBLIC RELEASE; DISTRIBUTION UNLIMITED.					
13. SUPPLEMENTARY NOTES					
<p>14. ABSTRACT</p> <p>Accurately processing multiple, time-coincident signals presents a challenge to Electronic Warfare (EW) receivers, especially if the signals are close in frequency and/or mismatched in amplitude. The metric that quantifies an EW receiver's ability to measure time-coincident signals is the Instantaneous Dynamic Range (IDR), defined for a given frequency estimation accuracy, a given frequency separation and a given SNR as the maximum signal amplitude ratio that can be accommodated. Using a two sinusoid time-series model, this thesis analyzes IDR for ideal intercept and parametric digital EW receivers.</p> <p>In general, the number of signals contained in the EW receiver measurement interval is unknown. Thus, the non-parametric Discrete Fourier Transform (DFT) is employed in an EW intercept receiver with the associated amplitude dependent spectral leakage which limits IDR. A novel method to improve the DFT-based intercept receiver IDR by compensating for the high amplitude signal's spectral leakage using computationally efficient 3 bin interpolation algorithms is proposed and analyzed. For a desired frequency estimation accuracy of 1.5 bins, the method achieves an IDR of 57 dB with little frequency separation dependence when the signals are separated by more than 2 bins with a low amplitude signal SNR of 10 dB.</p> <p>For situations where the number of signals contained in the measurement interval is known, the IDR of an Iterative Generalized Least Squares (IGLS) algorithm-based parametric receiver is analyzed. A real and complex signal IDR Cramer-Rao Bound (IDR-CRB) is derived for parametric receivers by extending results contained in Rife. For tight frequency estimate requirements (these requirements depend on the number of measurement samples), the IDR-CRB yields achievable bounds. For less stringent frequency estimate requirements, the IDR-CRB is unrealistic due to the noise threshold inherent to frequency estimation. Thus, to achieve good results when less stringent frequency estimates are required, the author defines the IGLS algorithm-based parametric receiver IDR at the amplitude ratio where the frequency estimates first achieve efficiency, i.e., the amplitude ratio where the overmodelling condition first ceases.</p>					
<p>15. SUBJECT TERMS</p> <p>Parameter Estimation, Maximum Likelihood, Linear Prediction, Electronic Warfare</p>					
16. SECURITY CLASSIFICATION OF:			17. LIMITATION OF ABSTRACT	18. NUMBER OF PAGES	19a. NAME OF RESPONSIBLE PERSON
a. REPORT	b. ABSTRACT	c. THIS PAGE			Meir Pachter, Professor, (ENG)
U	U	U	UU	122	19b. TELEPHONE NUMBER (Include area code) (937) 255-6565, ext 4280; e-mail: Meir.Pachter@afit.edu